UNIVERSITAT POLITÈCNICA DE CATALUNYA

DOCTORAL THESIS

Study of Graphene Hybrid Heterostructures for Linear and Nonlinear Optics

Author:
David ALCARAZ IRANZO

Supervisor:
Prof. Dr. Frank H. L. KOPPENS

A thesis submitted in fulfillment of the requirements for the degree of Ph.D. in Photonics

in the

Quantum Nano-Optoelectronics Group
ICFO

"The only true wisdom is in knowing you know nothing."

Socrates

To my family.

Acknowledgements

First of all, I would like to thank the attention and time that the reader will devote to this thesis.

To begin with, I want to greatly thank the great opportunity that Frank Koppens gave me by giving me his confidence to carry out this investigation. I also thank you for your scientific supervision and the constant support throughout all these years, as well as the understanding of the personal situation, not only of me, but of all the members of the NOE / QNOE (please decide!) research group.

I would like to extend this gratitude both in the scientific and personal spheres to all the members of the group with whom I have coincided in space-time coordinates, as well as to members of other groups and to the staff of the great space for scientific advancement that is ICFO. I especially wish to express my most sincere gratitude to Sébastien Nanot, who spent much of his time teaching me everything I needed to know and even more during the first years of my PhD. His teachings have marked me all the way. I would also like to remind so many colleagues that to a greater or lesser extent have left a dent in my path that it is impossible to name them all. But surely, they will be taken for granted.

I thank my family for all their support and understanding during the long and hard period that has led to the conclusion of this work. I thank my parents for their love, education and the obvious financial support prior to emancipation for too many years. Finally, I thank my wife for her invaluable help on a day-to-day basis, for sharing small and large things and especially the fruit of our love that is our family with the recent incorporation of little Olga.

Abstract

Graphene is the first of the 2D-material family. It is formed by carbon atoms arranged in a honeycomb lattice, which confers it intriguing physical properties that are still being discovered nowadays. A fundamental advantage found in graphene is the ability to gate tune its optical response from reflective (metallic) to absorptive (lossy dielectric). It is in the reflective conditions when it becomes more interesting since it supports surface plasmon polaritons in the mid-infrared, similar to metals in the near-infrared and visible spectral regions. Surface plasmons in metals are known to be more confined than free space propagating light. But graphene naturally excels in this aspect by offering a confinement factor around 100, which causes light to couple in inefficiently.

Several studies on metal plasmonics have shown the possibilities of confining light into tiny spatial dimensions with applications in molecular sensing as an example. Often, metal plasmons are used in the visible and IR regions with moderate confinement. However, Landau damping limits the optical field confinement due to penetration in the material and the consequent losses. In this thesis, it is shown that graphene-insulator-metal hybrid heterostructures can overcome that limitation by efficiently exciting plasmons in unpatterned graphene with vertical confinement down to the ultimate one-atom insulator thickness. It is accomplished by encapsulating graphene with a single layer of h$-$BN (or thicker oxide layers for the systematic study) and fabricating nano/micro-ribbons on top. The transmission extinction of the samples was measured and compared with theoretical models accounting for material nonlocal permittivity. The ultimate confinement and the validity of the excitation method are confirmed enabling a path towards ultrastrong light-matter interaction.

An example application of the aforementioned method to graphene nonlinear optics is also presented. The large intrinsic graphene third-order nonlinear optical response has been of great interest and it has been studied both theoretically and experimentally. However, there were not experiments covering all the expected features from the theory in the mid-infrared. This thesis expands the measurement range to cover the mentioned gap in planar graphene. Additionally, field enhancement and confinement provided by the hybrid heterostructure was exploited to increase the nonlinear third-harmonic generation signal in more than three orders

of magnitude. Intriguingly, it was found that some structures presented further modulation of the nonlinear signal which is attributed to the oscillatory nature of graphene plasmons. This opened an extra channel for extreme nonlinear gate tunability for the optimized parameters.

To summarize, this thesis presented means to achieve the regime of ultrastrong light-matter interaction, it fully characterizes it down to the one-atom spacer limit, and provides an example while demonstrating its applicability in graphene nonlinear optics.

Resumen

El grafeno es el primero de la familia de materiales 2D. Está formado por átomos de carbono dispuestos en una red de panal, lo que le confiere propiedades físicas intrigantes que todavía se están descubriendo hoy en día. Una ventaja fundamental que se encuentra en el grafeno es la capacidad de modificar "in-situ" su respuesta óptica de reflectante (metálico) a absorbente (dieléctrico con pérdida). Es en las condiciones reflectantes cuando se vuelve más interesante, ya que admite plasmones superficiales en el infrarrojo medio, de forma similar a como los metales lo hacen en las regiones espectrales del infrarrojo cercano y el visible. Se sabe que los plasmones superficiales en metales están más confinados que la luz que se propaga libremente. El grafeno sobresale en este aspecto al ofrecer un factor de confinamiento alrededor de 100 de forma natural, pero esto hace que la luz se acople directamente de manera muy ineficiente.

Varios estudios sobre plasmones metálicos han demostrado que las posibilidades de confinar la luz en pequeñas dimensiones espaciales pueden ser aplicadas, por ejemplo, en la detección de biomoléculas. A menudo, los plasmones metálicos se usan en las regiones visibles e IR con un confinamiento moderado. Sin embargo, el amortiguamiento de Landau limita dicho confinamiento del campo electromagnético debido a la penetración de éste en el material y las consiguientes pérdidas. En esta tesis, se muestra que las heteroestructuras híbridas de grafeno-dieléctrico-metal pueden superar esa limitación excitando eficientemente los plasmones en grafeno extendido con confinamiento vertical máximo, hasta el espesor de un solo átomo del material aislante. Tal efecto se logra encapsulando el grafeno con una sola capa de h$-$BN (o capas de óxido más gruesas para el estudio sistemático) y fabricando nano/microtiras metálicas sobre el dieléctrico. La extinción en transmisión de las muestras se midió y comparó con modelos teóricos que incluyen la permitividad no local de los materiales. El confinamiento final y la validez del método de excitación se confirman, permitiendo así allanar el camino hacia la interacción ultra-fuerte de luz y materia.

También se presenta un ejemplo de aplicación del método antes mencionado al campo de la óptica no lineal con grafeno. La gran respuesta óptica no lineal intrínseca de tercer orden del grafeno ha sido de gran interés y se ha estudiado tanto

teórica como experimentalmente en la comunidad. A pesar de ello, no hubo experimentos que cubrieran todas las características esperadas de la teoría en el infrarrojo medio por falta de rango en el dopaje del material. Esta tesis amplía dicho rango de medición para cubrir la brecha mencionada en grafeno extendido. Además, la mejora en el confinamiento y el aumento de la densidad de campo electromagnético proporcionados por la heteroestructura híbrida se explotaron para aumentar la señal de generación no lineal del tercer armónico en más de tres órdenes de magnitud. Curiosamente, se encontró que algunas estructuras presentaban una modulación adicional de la señal no lineal que se atribuye a la naturaleza oscilatoria (en el espacio) de los plasmones de grafeno. Esto permite la futura exploración de un canal basado en la alta modulación de la señal no lineal mediante el voltaje de puerta para parámetros optimizados.

En resumen, esta tesis presenta un medio para alcanzar el régimen de interacción ultrafuerte entre luz y materia, lo caracteriza completamente hasta el límite inferior de usar un espaciador de un solo átomo de espesor. Asimismo, proporciona un ejemplo mientras demuestra su aplicabilidad en la óptica no lineal de grafeno.

Contents

Introduction & objectives

Graphene is a one-atom-thick material consisting of carbon atoms arranged in a honeycomb lattice. It was first isolated in 2004 [1] being worthy of the Nobel Prize in Physics in 2010 *"for groundbreaking experiments regarding the two-dimensional material graphene"*. Since then, it has been characterized many times using transport [1, 2, 3, 4, 5], Raman scattering [6, 7], optical transmission/reflection, etc. However, thin carbon materials down to a few layers were already found on substrates after epitaxial growth [8, 9, 10, 11], and other deliberate attempts were also performed [12].

Nowadays graphene can be obtained from different methods: mechanical exfoliation from a graphite crystal [1, 2](which is commonly known as *"the scotch tape technique"*), ultrasonication in a chemical solution (*"wet exfoliation"*)[13, 14], chemical vapor deposition (CVD) [15, 16, 17, 18], and epitaxy [19, 20, 21, 22]. Depending on the method used, a range of sizes, number of layers, electron mobility, homogeneity and transfer-ability of the layer are found (among other possible properties of interest).

Graphene is the first of a daily growing list of 2D-materials comprising insulators (such as hexagonal boron nitride, h−BN), semiconductors (e.g. the big group of transition metal chalcogenides, TMDs), and graphene itself, a semi-metal. The number of possible 2D-materials is so large that databases using computational methods had to be created in order to retrieve a reduced list of the viable ones [23, 24, 25, 26]. All these materials can be combined in hetero-structures [27, 28, 29, 30] by stacking them, which can provide new properties that match a specific need in a few atoms thickness [31, 32, 33, 34, 35, 36, 37, 38, 39]. These materials can be stacked using wet transfer [40, 41] or dry transfer [1] depending on the material origin or the targeted application. With the latter, it was observed that while using h−BN as substrate [42] and especially full h−BN encapsulation [43, 18] (also called *"the pick-up technique"*), graphene (and other 2-D materials) quality was improved thanks to the h−BN flatness and screening capability. Nowadays it is the preferred method used in the fabrication of the state of the art research devices.

Lately, there has been a growing interest in systems of multiple 2D layers stacked at

will, especially since the discovery of bilayer graphene unconventional superconductivity for twist angle between layers of $\sim 1.1^{\circ}$ (the magic angle) [44, 45]. After this discovery, everything is moving around "giving it a twist" in the graphene and 2D-material community, although there were some studies beforehand [33, 46, 47, 48, 49, 50, 51, 52]. It paved the way of "twisttronics" [52], where the manipulation of the twist angle between two adjacent layers unleashes new properties caused by the formation of a superlattice [30, 45, 53, 54, 55]. A superlattice effect was already observed when stacking graphene and h$-$BN close to perfect alignment: the appearance of satellite Dirac peaks (increased resistivity due to the low number of free carriers away from the charge neutrality) [46, 48, 49].

Despite the importance of the above-mentioned topics, this thesis is focused in the fundamental topic of light-graphene interaction; with special emphasis on electromagnetic field confinement, using surface plasmon polaritons (coupled oscillations of the fields and the metal charge carrier density along the metal-dielectric interface [56]) and the nonlinear optical response. The linear optical properties can be extracted from the band structure (Dirac cones) [57, 58, 59, 60, 61] and assuming that graphene can be considered essentially a 2DEG (2-Dimensional electron gas) [62]: constant absorption$= \pi\alpha \approx 2.3\%$, Pauli blocking and, Drude response, which are all in turn gate tunable [63, 64]. Originally, 2-DEGs are formed by semiconductor layered heterostructures, exhibiting negative values of the real part of the dielectric permittivity in the THz spectral region and hence, supporting surface plasmon polaritons [65, 66, 67]. However, in the case of graphene, such property can be extended up to the MIR or even NIR for extremely tunable devices (capable of Fermi energy ~ 1 eV [68, 69, 70, 71, 72, 73]).

Plasmons are not the only polaritons that can be observed in 2D materials [74, 75], yet they are the most versatile in terms of electrical tunability and excitation wavelength span (from THz to MIR [76, 77]). Their wavelength is shrunk down naturally by 2 orders of magnitude compared to the free space wavelength (which is much larger confinement than for metal surface plasmons); besides, the out-of-plane field is evanescent, providing in total, up to 6 to 8 orders of magnitude volume confinement. Due to the deep sub-wavelength scale of graphene plasmons, it is not straight-forward to couple light in and to observe them, although there might be interesting applications [78, 79, 80, 81].

The aforementioned fact led initially to two different approaches to couple propagating photons into plasmons. First, by using an illuminated metallic coated AFM tip to probe the material response while providing the necessary momentum to overcome the mismatch (s-SNOM, scattering-type scanning near-field optical microscopy). This technique allows to image plasmons directly using the scattered light [82, 83, 84, 34, 85] or indirectly using the generated photocurrent [86]. The

latter enabled the detection of acoustic plasmons with smaller wavelengths and reduced scattering due to the screening of the Coulomb long-range electron interaction caused by the vicinity of a nearby metal in the THz [87, 88, 89, 90]. These more confined plasmons represent the first key ingredient for the development of the thesis.

The second method consists of structuring graphene thus creating resonant plasmonic cavities while providing discrete momentum values much larger than the inverse of the free-space excitation wavelength. It is considered a far-field methodology because the plasmons are excited and detected by free-space light. There are examples using graphene nanostructures onto different substrates and shapes [91, 92, 93, 94, 95, 96, 97], including a Salisbury screen[32] and plasmons thermal emission [98]. Additionally, hybrid structures comprising graphene and metal structures arose [99], combined also with a Salisbury screen [100] which evolved towards the achievement of almost perfect absorption [101]. The combination of metallic structures in proximity with graphene is the second ingredient required for this thesis.

Finally, in the context of the nonlinear optical response of graphene, there have been experiments and theoretical works exploring the second, third and even higher-order nonlinear processes either with or without the intervention of plasmons. The first nonlinear optics experience in graphene was obtained from FWM (four-wave mixing) [102]. Later on, the same effect was also studied in different configurations [103, 104] alongside THG (third-harmonic generation) [105, 106] and, nonlinear refractive index [107]; all in the NIR/visible/UV range. HHG (high harmonic generation) experiments were carried in planar graphene for MIR [108, 109], and THz [110]. Also, FWM involving structured graphene with plasmonic contribution using MIR and NIR excitation [111] has been studied. However, some experiments showed nonlinear responses driven by thermal effects [112, 113] instead of its intrinsic response, or at least it is not easy to dissociate them. The experiments that explore the gate tunability of the $\chi^{(3)}$ response of graphene in MIR [114, 115] do not cover all the expected features clearly with their tuning range.

Since the discovery of graphene, there have been many theoretical works on the nonlinear optical response involving plasmons [116, 117, 118, 119, 120, 121, 122, 123, 124] or just considering its intrinsic odd-order nonlinear response [125, 126, 127, 128]. There is an interesting effect caused by plasmons in graphene consisting of enabling a $\chi^{(2)}$ response [129, 130].

The large intrinsic graphene third-order nonlinear optical response is the final ingredient to explore enhanced light-graphene interactions in this thesis. In some cases, we combine the different ingredients to realize that state's objectives. In

short, the objectives are as follows:

Goal 1 (Chapter 2)

The first goal of the thesis is to achieve plasmon excitation in unpatterned graphene from far-field light efficiently, allowing the use of patterned metallic structures. The objective is to maximally preserve the graphene quality (carrier mobility and homogeneity) to obtain stronger and narrower resonances. To finalize this goal, the method must be characterized.

Goal 2 (Chapter 3)

This second Goal aims for the exploration of the out-of-plane energy density and field confinement/enhancement down to the atom's scale. The use of metallic periodic structures in combination with the one-atom-thick insulating material h−BN is mandatory to reach the ultimate limit of one atom spacer.

Goal 3 (Chapter 4, first part)

This goal is focused on the observation of the gate tunable nonlinear optical response of graphene for excitation in the Mid-IR. There were initial studies showing several of the nonlinear response features but lacking experimental evidence on the doping range around the interband transition energy corresponding to the energy of three photons [114, 115]. It is intended to cover that experimental gap.

Goal 4 (Chapter 4, second part)

The last goal of this thesis is to explore the effects of graphene plasmonics in order to leverage the field enhancement provided by them and use it to enhance (or tune) the already outstanding graphene nonlinear optical response.

Chapter 1

Overview of graphene properties

1.1 Electrical properties

Knowing the electrical properties of a material is useful in many regards. It allows us to compare it with other materials, characterize specific devices for quality checks and, know how they will relate when used in combination with other electrical materials, to name a few.

Given that graphene is a 2D material, some of its electrical properties can be explained using 2-DEGs analogies[62], some using tight-binding models [131, 132], and others can be explained by simple solid state physics formulas. The most important magnitudes to describe graphene electrically are its band structure [133, 132] (with all the parameters that can be extracted from it) and the carrier mobility/lifetime/relaxation time, which all together determine graphene's DC characteristics almost completely.

1.1.1 Band structure

The electronic band structure for graphene is important to know the relation of momentum and energy, density of states, etc... It is crucial to know how the bands of graphene will align with another material in an electrical contact, for example.

It is calculated using the tight-binding model including hoping to nearest and second-nearest neighbors [133, 132]. The energy bands are described as:

$$\begin{aligned} E_{\pm}(\mathbf{k}) &= \pm t\sqrt{3+f(\mathbf{k})} - t'f(\mathbf{k}); \\ f(\mathbf{k}) &= 2\cos\left(\sqrt{3}k_y a\right) + 4\cos\left(\frac{\sqrt{3}}{2}k_y a\right)\cos\left(\frac{3}{2}k_x a\right), \end{aligned} \tag{1.1}$$

where plus and minus signs correspond to the upper π^* and the lower π bands. We can observe 6 Dirac cones in Fig. 1.1 using eq.1.1 at **K** and **K**′ points of the Brillouin zone. When considering $\|\mathbf{q}\| \ll \|\mathbf{K}\|$ the linear dispersion relation (see inset in Fig. 1.1) becomes evident:

$$E_{\pm}(\mathbf{q}) \approx \pm v_F \|\mathbf{q}\| + O[(q/K)^2], \tag{1.2}$$

with **q** being the electron momentum relative to the Dirac point (DP) (**K** or **K**′ points in the first Brillouin zone), also known as charge neutrality point (CNP). The proportionality constant between energy and momentum is the Fermi velocity ($v_F \simeq 10^6 \mathrm{m/s} \approx c/300$).

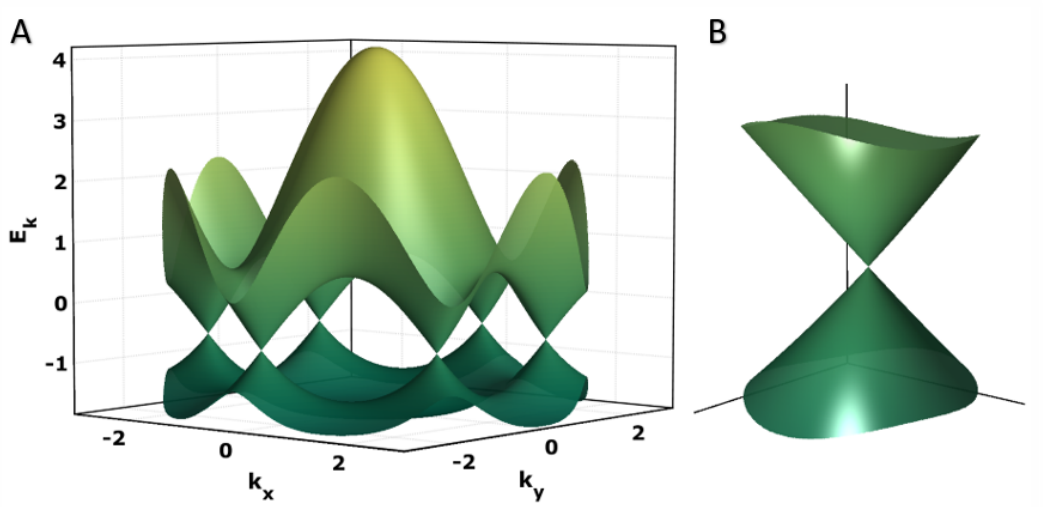

FIGURE 1.1: **A** - Graphene band structure from tight binding model of eq.1.1. Hoping values of $t = 2.7$ and $t' = -0.2t$, for nearest and second-nearest neighbors. **B** - K point zoom.

The Dirac-like dispersion relation implies a constant electron velocity and massless quasiparticles, opposite to parabolic bands in semiconductors with massive quasiparticles and energy-dependent velocity. A consequence of the graphene quasiparticles following the massless Dirac equation is a square root dependence of the cyclotron mass (m^*) with the electronic density [62, 134]. Accordingly one obtains:

$$m^* = \frac{E_F}{v_F^2} = \frac{k_F}{v_F} = \frac{\sqrt{\pi}}{v_F}\sqrt{n}. \tag{1.3}$$

A useful relation of E_F with n can be derived straight forward. However, in the context of eq.1.1 to eq.1.3, the authors [133, 132] used the convention $\hbar = 1$. A direct expression including $\hbar \neq 1$ is:

$$E_F = \text{sign}\,(n)\hbar v_F \sqrt{\pi n}, \tag{1.4}$$

which is positive for electron doping ($n > 0$) and negative for hole doping ($n < 0$). As a consequence, $E_F = 0$ is the reference energy with ideally no charge carriers.

1.1.2 Carrier density control & DC conductivity

Control of n or E_F in graphene is relatively easy thanks to its 2D nature and low carrier density by simply applying an electrostatic potential. This section will introduce the concept of capacitance and show its relation to surface carrier density and mobility for graphene, which are the main terms governing DC conductivity in semiconductors. Furthermore, the Hall measurement scheme will be also analyzed.

1.1.2.1 Capacitor model

It is well known in electrostatics that a parallel plate capacitor accumulates equal charge of opposite sign on each one of its plates. The number of charges accumulated is proportional to the voltage applied between them; the proportionality constant is called capacitance (C). This magnitude can be measured electrically, but this measurement is normally used to know the isolating material dielectric constant.
The capacitance of a single dielectric infinite parallel plate capacitor expression given by:

$$C = \varepsilon_0 \varepsilon_R \frac{A}{d}. \tag{1.5}$$

However, since we are interested in obtaining surface carrier density, we will rather use the surface capacitance per unit of fundamental charge (C_S), or from now on simply surface capacitance. It represents the number of carriers with the fundamental charge (e) per unit area. It is calculated as:

$$C_S = \frac{\varepsilon_0 \varepsilon_r}{de}, \tag{1.6}$$

with units of $\text{V}^{-1}\text{cm}^{-2}$, thus, graphene surface carrier density is obtained by:

$$n = C_S \Delta V, \tag{1.7}$$

where $\Delta V = V_{BG} - V_{CNP}$ is the voltage difference between the applied back-gate voltage and the CNP voltage position, respectively.

If the system consists of several layers of different dielectrics, the total capacitance is obtained as the sum of capacitors in series using the inverse sum rule:

$$C_{Total}^{-1} = \sum_i C_i^{-1}. \tag{1.8}$$

As seen in this section, the thickness and dielectric constant of the materials surrounding graphene are crucial for using its gate tunable properties (n dependent) such as device resistance (FET) or optical properties, which will be discussed later on (section 1.2). However, the graphene band structure also contributes to the capacitance due to its semimetallic behavior and limited density of states.

1.1.2.2 Quantum capacitance

Quantum capacitance (QC) explains the deviation from $Q = CV$ when at least one of the plates does not behave as a perfect conductor (∞ number of charge carriers density of states). Due to the limited density of states, the charge carriers can only occupy discrete energy levels. This effect occurs normally in semiconductors, but it is also important for graphene close to the CNP. The difference in those energy levels is translated into an energy "cost" to insert a charge in the system, thus reducing the effect of the applied potential when compared to a material with an infinite number of available states. Hence, when the density of states of the material of one or both of the plates in the capacitor is comparable to the electrostatically induced charges using Gauss law for a given applied voltage, this effect cannot be neglected. The quantum capacitance must be introduced in series with the surface capacitance:

$$C_{Total}^{-1} = C_S^{-1} + C_Q^{-1}. \tag{1.9}$$

In the case of graphene, one can obtain the density of states from the two-dimensional electron gas (2-DEG) model. It describes properly the experimental trend and reads [135]:

$$C_Q = \frac{2e^2 k_B T}{\pi(\hbar v_F)^2} \ln\left[2\left(1 + \cosh\frac{E_F}{k_B T}\right)\right]. \tag{1.10}$$

In case $E_F \gg k_B T$ the previous expression approximates to:

$$C_Q \approx e^2 \frac{2E_F}{\pi(\hbar v_F)^2} = \frac{2e^2}{\hbar v_F \sqrt{\pi}} \sqrt{n}, \tag{1.11}$$

where $n = |n_G| + |n^*|$ is the addition of the gate induced and the impurity charge density, correspondingly.

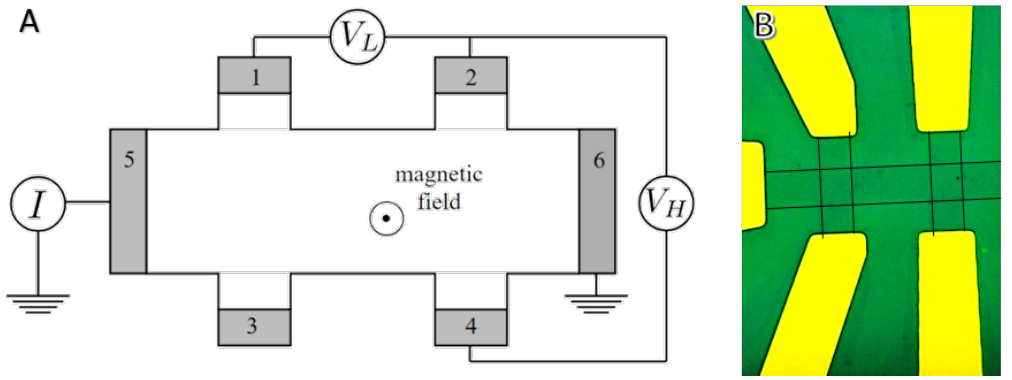

FIGURE 1.2: **A** - Schematic of a standard Hall bar [138]. **B** - A graphene Hall bar with bottom Au contacts. The channel width is 7 μm and its length is 40 μm.

Graphene quantum capacitance monotonically increases with the number of carriers. Consequently, its effects won't be noticeable for doping levels whose $C_Q \gg C_S$.

1.1.2.3 Charge carrier extraction and mobility

A Hall measurement scheme consists of conductive material with electrical connections disposed in a Hall bar shape (see Fig 1.2), with constant source-drain current and longitudinal (L or sometimes xx) and perpendicular (H from Hall or sometimes xy) voltage drops measured as a function of the external magnetic field. The longitudinal voltage drop provides the material resistance as normally calculated from Ohm's law. On the other hand, it is possible to calculate the Hall resistance from the perpendicular voltage drop, which is related to the magnetic field, the sign and the number of charge carriers through [136, 137]:

$$R_H = \frac{E_\perp}{j_\parallel B} = \frac{V_H t}{IB} = -\frac{1}{Bne}, \tag{1.12}$$

where t is the thickness of the conductor.

The conductance of graphene (and any semicontuctor) is typically defined as [136, 137]:

$$\sigma = \mu n e, \tag{1.13}$$

where n is the carrier density, e the electron charge and μ the carrier mobility. Therefore, in the situation that we know the carrier density and the conductance from Hall measurements, the mobility is calculated using:

$$\mu = \frac{\sigma}{ne}. \tag{1.14}$$

Nonetheless, samples are not always suitable for Hall measurements and the carrier density values are not accessible in a direct way. In such a case, we might prefer to use differential values for carrier density and conductance from back-gate dependent two or four-probe measurements (the first being less accurate due to the contact resistance contribution). The differential mobility reads:

$$\mu = \frac{\delta\sigma}{\delta nq} = \frac{\delta\sigma}{C_S \delta V q} = \frac{1}{C_S q}\frac{\delta\sigma}{\delta V}. \tag{1.15}$$

The term $\frac{\delta\sigma}{\delta V}$ is obtained from the trans-conductance measurement and it corresponds to the change in conductance per unit of back-gate voltage change. Example measurements of differential and Hall mobility measurements of the sample in Fig. 1.2 are shown in Fig. 1.3 and Fig. 1.4, respectively. CVD (chemical vapor deposition) grown graphene was used.

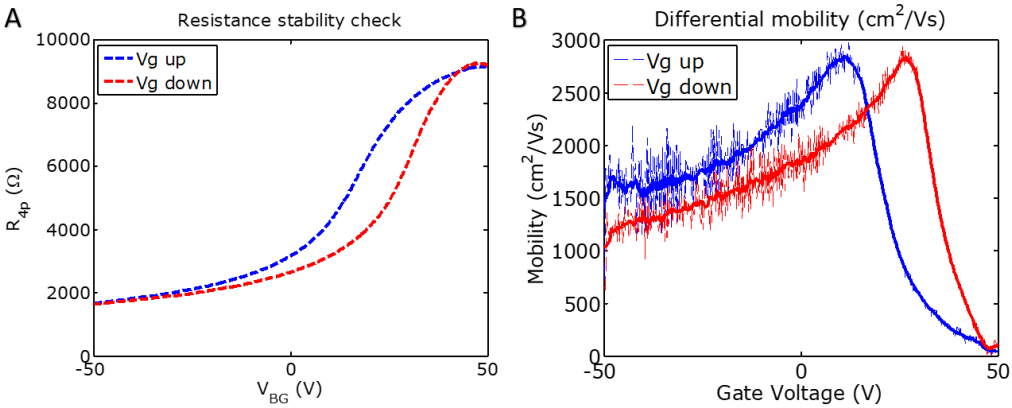

FIGURE 1.3: **A** - Measured 4 probe (4p) resistance of the channel in the sweep up (blue) and down (red). **B** - Differential mobility calculated from R_{4p} using eq.1.15 for both sweep directions.

When measuring differential mobility, one measures the transconductance i.e. the changes in the drain current due to changing the gate voltage (V_{BG}). It is typically done in a four-probe (4p) configuration which eliminates the contact resistance contribution and the measured value is the voltage drop caused by the channel resistance, hence trans-resistance. The trans-resistance is obtained by dividing the source voltage by the transconductance current in a 2-port configuration. However, this value is only used for qualitative purposes such as observation of hysteretical behavior and CNP localization.

To calculate mobility through eq.1.15 one must obtain the conductivity/resistivity first. It is possible to convert the drain current/voltage drop (for 2-probe or 4p configurations) into conductivity (σ)/resistivity (ρ) by using the conductance (G) /resistance (R) scaling with the geometrical values:

$$R = \rho \frac{L}{tW} = \frac{1}{G} = \frac{1}{\sigma} \frac{L}{tW}. \tag{1.16}$$

The capacitance of the gate is given by the dielectric thickness and permittivity from the manufacturer and tabulated values, respectively. Nonetheless, in the manufacturing process, there are some tolerances which lead to inaccurate capacitance values. In Fig. 1.3 measurements, hysteresis, and mobility dropping to 0 at CNP are observed. The former is usually related to the gate oxide charge traps while the latter comes from the broadness of the resistance peak due to charge puddles (inhomogeneity). These effects combined cause the carrier density to be inaccurate both in origin and slope.

Hall type measurements solve this issue thanks to the capability of extracting accurately the number and the sign of the charge carriers (see Fig. 1.4). It requires to shape the sample or place contact pads in a Hall bar configuration which sometimes is not convenient when conductivity measurements are, normally, only a characterization step and not the final purpose.

Fig. 1.3 and Fig. 1.4 measurements lead to similar mobility values far from CNP. It is concluded then that both methods are valid if the CNP is visible and there are accurate values for gate oxide thickness and permittivity. It is worth commenting that using a 2-probe configuration leads to a larger uncertainty due to the gate dependent contribution of the contact resistance.

1.2 Optical properties

The different conductivity models that can be obtained/used for graphene in the linear regime are explored in this section. The models described in the linear response are the Drude model, and the local and nonlocal RPA. Additionally, the means to calculate conductivity at nonzero temperatures will be also defined and exemplified.

Every electromagnetic field must follow Maxwell's equations and here they are explicitly written [139]:

$$\nabla \cdot \mathbf{D} = \rho, \tag{1.17}$$

$$\nabla \cdot \mathbf{B} = 0, \tag{1.18}$$

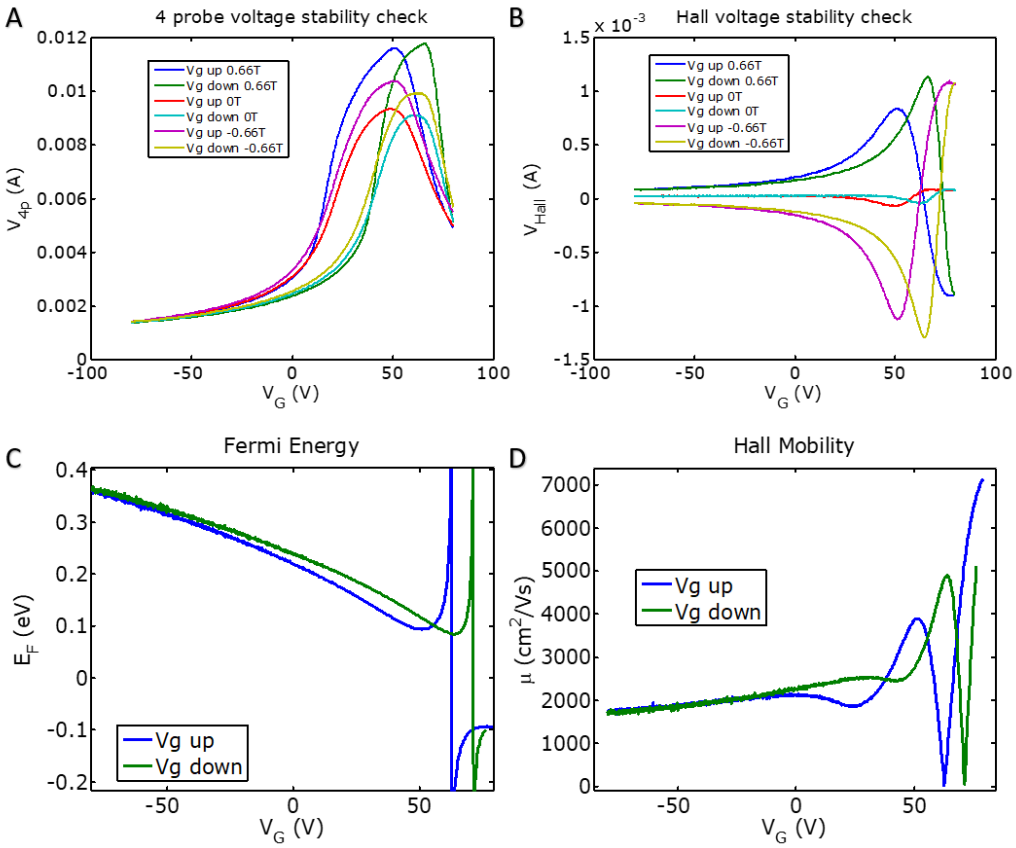

FIGURE 1.4: **A** - Longitudinal voltage drop in the sweep up and down directions for $B = 0.66,\ 0$ and -0.66 T. **B** - Same for the perpendicular voltage drop (Hall voltage). **C** - Extracted carrier density (in eV) in the up/down direction sweeps. **D** - Corresponding extracted carrier mobility.

$$\nabla \times \mathbf{H} = \frac{\partial \mathbf{D}}{\partial t} + \mathbf{J}, \tag{1.19}$$

$$\nabla \times \mathbf{E} = -\frac{\partial \mathbf{B}}{\partial t}, \tag{1.20}$$

where ρ and $\mathbf{J}$ are charge and current densities, and the electric and magnetic fields $\mathbf{E}$ and $\mathbf{H}$ are related to the electric displacement $\mathbf{D}$ and magnetic induction $\mathbf{B}$ fields in isotropic and non-magnetic media via:

$$\mathbf{D} = \varepsilon_0 \varepsilon \mathbf{E}, \tag{1.21}$$

$$\mathbf{H} = \frac{1}{\mu_0}\mathbf{B}; \tag{1.22}$$

with ε_0 and μ_0 referring to the vacuum permittivity and permeability, correspondingly, and ε is the relative permittivity of the media. In this thesis, the relative permeability μ is assumed to be 1.

1.2.1 Optical modeling of graphene

Since graphene is a 2D material, it is possible to model it as a surface conductivity or as a bulky material with a given thickness and bulk permittivity. Each type of modeling might be chosen depending on the method to use and/or the simulation purpose/limitations.

1.2.1.1 Graphene as a finite thickness layer

Introducing graphene as a 3D material is quite straightforward using the analogy of the Drude-like metal permittivity and substituting its conductivity by graphene's one. Since graphene is a 2D, its conductivity is also in 2D units, so one must correct for it dividing by its thickness (d_g) and use the following relative permittivity expression:

$$\varepsilon_D = 1 + \frac{i\sigma}{d_g \omega \varepsilon_0}. \tag{1.23}$$

This approach was widely used in the community and applied to commercial software. However, it required a lot of computing power due to subdivisions of the graphene layer thickness. Nowadays, its use is decaying in favor of graphene as an interlayer conductivity as a consequence of faster and/or less demanding computations.

1.2.1.2 Graphene as a surface conductivity

According to this approach, graphene is input as a surface conductivity. In order to properly use this methodology, one must consider carefully the continuity equations [139]:

$$\hat{\mathbf{n}} \cdot (\mathbf{D}_1 - \mathbf{D}_2) = \rho_S, \tag{1.24}$$

$$\hat{\mathbf{n}} \cdot (\mathbf{B}_1 - \mathbf{B}_2) = 0, \tag{1.25}$$

$$\hat{\mathbf{n}} \times (\mathbf{B}_1 - \mathbf{B}_2) = \mu_0 \mathbf{J}_S, \tag{1.26}$$

$$\hat{\mathbf{n}} \times (\mathbf{E}_1 - \mathbf{E}_2) = 0, \tag{1.27}$$

where ρ_S and $\mathbf{J}_S$ the surface carrier density and current density. $\mathbf{J}_S$ relates with σ (graphene surface conductivity) via Ohm's law $\mathbf{J}_S = \sigma \mathbf{E}_S$. These expressions will be used to obtain the graphene transfer matrix in 1.2.3.1. The proper expressions for the different graphene conductivity models to use will be introduced next.

1.2.2 Linear optical conductivity

Graphene optical conductivity is the key tool to understand its electrically tunable optical properties. Through eq.1.23, graphene's optical conductivity is related to the permittivity. It provides information about the light-carriers type of interaction, resistive, capacitive or inductive.

Generally, one can state that the real part of the conductivity is related to the optical absorption (resistance as an electrical analogy) since it appears in the imaginary part with a positive sign (the $\varepsilon = \varepsilon_1 + i\varepsilon_2$ convention is used here). On the other hand, negative or positive imaginary part of the conductivity will determine if graphene behaves as a dielectric ($\varepsilon_1 > 0$, capacitive conductance) or as a metal ($\varepsilon_1 < 0$, inductive conductance), respectively; with the offset in the conductivity given by the 1 in the real part of eq.1.23.

1.2.2.1 Drude conductivity

The Drude model describes the metallic behavior of a material using the electrons in the Fermi sea and its effects. Mainly, the conductivity increases (in absolute value) with the number of carriers and decreases with frequency, electron mass and electron scattering time/lifetime/relaxation time (depending on the context it will be named differently). The characteristic expression of Drude conductivity for a 3D metal reads [79]:

$$\sigma_v(\omega) = \frac{n_v \mathrm{e}^2}{m^*} \frac{i}{\omega + \mathrm{i}\tau^{-1}}, \tag{1.28}$$

where n_v is the volumetric charge carrier density, e is the electron charge, m^* is the carriers effective mass and τ is their scattering time. If we reduce dimensionality and exclude the scattering time (to introduce it again, one should change ω by $\omega + \mathrm{i}\tau^{-1}$, graphene Drude conductivity [140]:

$$\sigma_D^{(1)}(\omega) = \frac{i\mathrm{e}^2 |E_F|}{\pi \hbar^2 \omega} = \frac{i 4 \alpha \varepsilon_0 c |E_F|}{\hbar \omega}, \tag{1.29}$$

where $\alpha \equiv \mathrm{e}^2 / 4\pi\varepsilon_0 \hbar c \ \ (\sim 1/137)$ is the fine structure constant and provides a different vision of the Drude model.

This model only provides us the metallic behavior of graphene, hence losing the interband transition contribution (which is crucial in some regimes) and the light momentum dependence which will be useful further on.

1.2.2.2 Local RPA

In order to solve the first issue, it is introduced the graphene interband conductivity ($T = 0$K):

$$\sigma_I^{(1)}(\omega) = \frac{e^2}{4\hbar}\left(\theta(\hbar\omega - 2E_F) - \frac{i}{\pi}\ln\left|\frac{2E_F + \hbar\omega}{2E_F - \hbar\omega}\right|\right) \tag{1.30}$$

which combined with the Drude conductivity gives rise to the graphene local RPA conductivity ($T = 0$K):

$$\sigma_L^{(1)}(\omega) = \sigma_D^{(1)}(\omega) + \sigma_I^{(1)}(\omega). \tag{1.31}$$

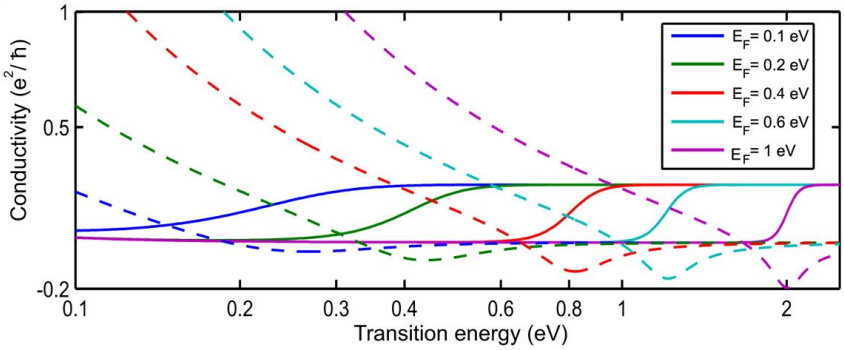

FIGURE 1.5: Real (solid) and imaginary(dashed) parts of local RPA conductivity as a function of excitation energy for several E_F values [140].

We can obtain the local RPA ($q \to 0$) analytical expression including T dependence as a derivation from the nonlocal (momentum dependent) RPA, which is developed in the next subsection, as [140]:

$$\sigma(\omega) = \frac{2e^2T}{\pi\hbar}\frac{i}{\omega + i\tau^{-1}}\log\left[2\cosh\left(E_F/2k_BT\right)\right] + \frac{e^2}{4\hbar}\left[H(\omega/2) + \frac{4i\omega}{\pi}\int_0^\infty d\varepsilon\frac{H(\varepsilon) - H(\omega/2)}{\omega^2 - 4\varepsilon^2}\right], \tag{1.32}$$

where

$$H(\varepsilon) = \frac{\sinh(\hbar\varepsilon/k_B T)}{\cosh(E_F/kBT) + \cosh(\hbar\varepsilon/k_B T)}.$$

1.2.2.3 Nonlocal RPA at 0 K

This model is used to solve the second issue (momentum dependence of graphene's optical conductivity) but it cannot provide the temperature dependence.

First, it is needed to establish some useful relations for the derivation. The longitudinal conductivity is related to the susceptibility through:

$$\sigma(\omega, q) = -i\omega\chi_\tau(\omega, q) \tag{1.33}$$

where the relaxation time is introduced using carrier number preserving Mermin prescription [141]:

$$\chi_\tau(\omega, q) = \frac{(1 + i/\omega\tau)\chi(\omega + i/\tau, q)}{1 + (i/\omega\tau)\chi(\omega + i/\tau, q)/\chi(0, q)} \tag{1.34}$$

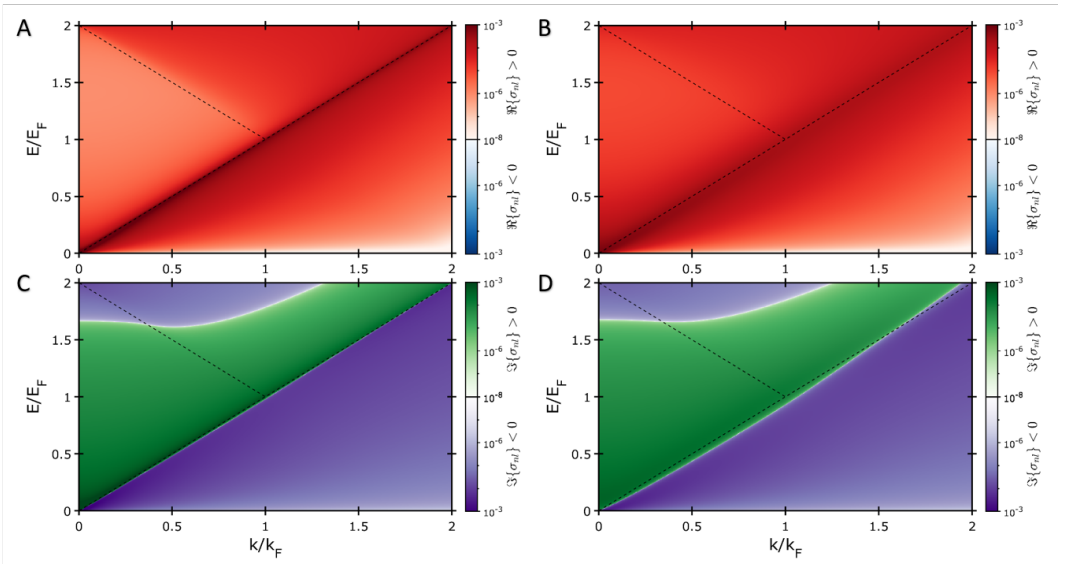

FIGURE 1.6: Non-Local RPA colorplots or real (**A**, **B**) and imaginary (**C**, **D**) parts in double logarithmic color-scale of the nonlocal RPA graphene conductivity for $E_F = 200$ meV and $\tau = 300$ and 30 fs for left (**A**, **C**) and right (**B**, **D**), respectively. Dashed black lines indicate interband transitions.

with the linear RPA response function being:

$$\chi(\omega,q)=\frac{e^2}{2\pi^2\hbar q^2}\int d^2\mathbf{q}'\sum_{s,s'=\pm}\left[1+ss'\frac{\mathbf{q}'\cdot(\mathbf{q}+\mathbf{q}')}{q'\,|\mathbf{q}+\mathbf{q}'|}\right]\frac{\theta_F(s'v_F\,|\mathbf{q}+\mathbf{q}'|-\theta_F(sv_Fq'}{\omega+v_F(sq'-s'\,|\mathbf{q}+\mathbf{q}'|)+i0^+} \tag{1.35}$$

and $\theta_F(E)$ is the Fermi-Dirac distribution. This expression, however, admits an analytical form for zero temperature:

$$\chi(\omega,q)=\frac{e^2}{4\pi\hbar}\left[\frac{8k_F}{v_Fq^2}+\frac{G(-\Delta_-)\theta[-\Re\Delta_--1]+[G(\Delta_-)+i\pi]\theta[\Re\Delta_-+1]+G(\Delta_+)}{\sqrt{\omega^2-v_F^2q^2}}\right] \tag{1.36}$$

being $G(z)=z(z-1)(z+1)-\log(z+(z+1)(z-1))$, and $\Delta_\pm=(\omega/v_F\pm 2k_F)/q)$. The imaginary part of the logarithm is taken in the $(-\pi,\pi]$ range. Additionally, the response at zero frequency stands:

$$\chi(0,q)=\frac{e^2}{2\pi\hbar v_Fq}\left\{\frac{4k_F}{q}-\theta(1-x)\left[x\sqrt{1-x^2}-\cos^{-1}x\right]\right\},$$

where $x=2k_F/q$. At this point, we can obtain the analytical expression eq.1.32, which corresponds to the local limit and includes temperature dependence.

Examples of nonlocal RPA conductivity are shown in Fig. 1.6 for $\tau=300$ and 30 fs, which correspond to the typical range of exfoliated and CVD grown graphene. It is obvious that different τ values provide different optical properties to graphene, thus graphene quality and hence, the obtention method is crucial for many applications (e.g. size requirements). Firstly, if one pretends to exploit Pauli blocking (blockade of transitions due to the level of full occupation) in order to tune the material transparency, exfoliated graphene provides less absorption/larger contrast. And secondly, exfoliated graphene presents a better metallic behavior due to larger positive imaginary part according to eq.1.29, 1.32-1.36 and Fig. 1.6.

1.2.2.4 Temperature dependence

As there is no analytical solution for the temperature dependence of some graphene properties including the optical conductivity, one can simply use Maldague's identity [142] to calculate them numerically:

$$\sigma(\omega,k,\tau,E_F,T)=\frac{1}{4k_BT}\int_{-\infty}^{\infty}dE\frac{\sigma(\omega,k,\tau,E,0)}{\cosh^2\left(\frac{E-E_F}{2k_BT}\right)}. \tag{1.37}$$

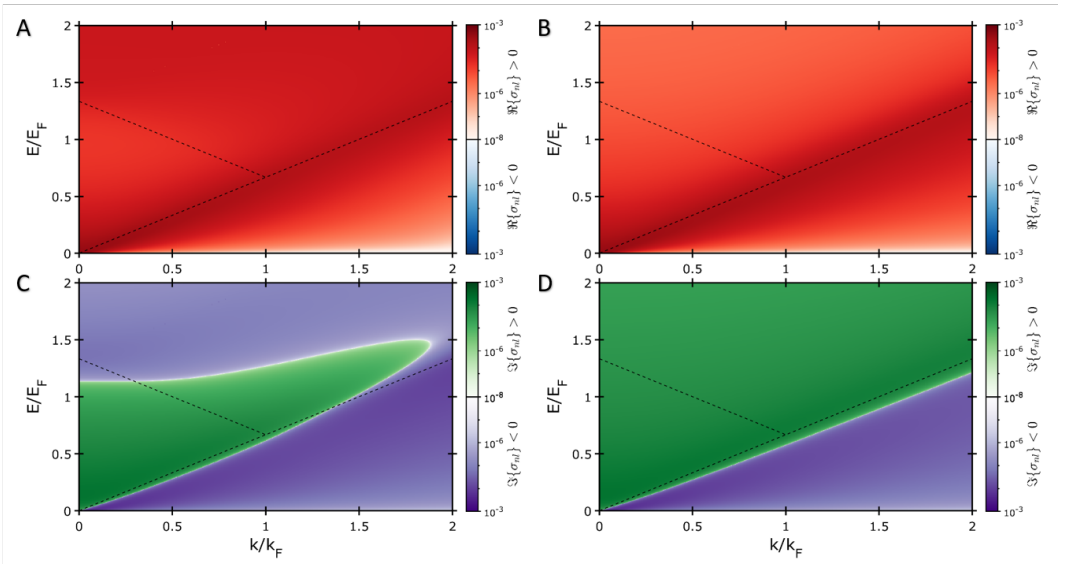

FIGURE 1.7: 0 K (**A**, **C**) and 300 K (**B**, **D**) nonlocal RPA conductivity real (**A**, **B**) and imaginary (**C**, **D**) parts in double logarithmic color-scale in a.u. for $E_F = 10$ meV and $\tau = 300$ fs.

It assigns a weight to the evaluated conductivity in a range of chemical potentials, accordingly to the chemical potential shift and the designated temperature. The desired temperature dependence is obtained by integrating the aforementioned quantity over the complete energy space.

An example use of the above-mentioned prescription is to obtain the nonlocal RPA conductivity at $T \neq 0$ (see Fig. 1.8). It shows that for excitation energy above $2E_F$, it is possible to observe metallic behavior ($\Im\{\sigma\} > 0$, i.e. inductive) as shown in [88] where plasmons at CNP were observed at room temperature in the THz range. Another effect is the absorption diminution (lighter red color, $\Re\{\sigma\} \downarrow$) for interband transitions (crossing the negative slope dashed line) which indicates an effective increase of the doping (in absolute terms). And finally, but more intriguingly, there are regions preserving metallic behavior (intense green) crossing the Dirac cone towards the Landau damping region (positive slope dashed line). This effect is more prominent for higher temperatures, with apparent reduction of losses.

1.2.3 Numerical methods

This section covers several methods to obtain the optical response of graphene, their pros, their cons and, their applicability.

1.2.3.1 Transfer matrix method (TMM)

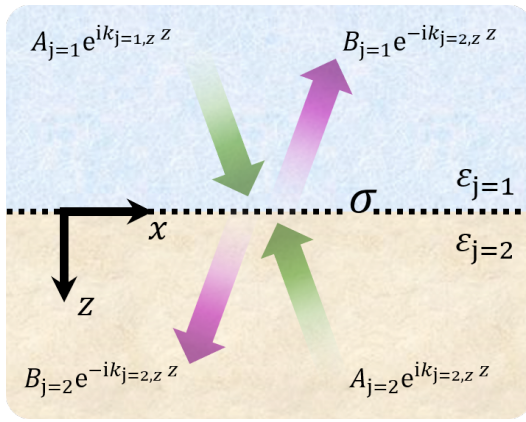

FIGURE 1.8: Schematic of fields used for TMM. Graphene is represented by the black dotted line between materials 1 and 2.

The transfer matrix method (TMM) is an analytical approach to calculate the optical response of parallel-plane multilayered systems and the fields at each position given the layer properties and the input field amplitudes. It consists of a series of matrices which transfer the electric and magnetic fields to the next layer (transfer matrix T) or through the layer (propagator matrix P). They are multiplied consecutively for every layer in the system. In the end, the matrix obtained relates the input fields with the output fields. Additionally, as already mentioned, the fields at all layers can be retrieved: simply by storing the obtained values at the intermediate steps.

In our approach we consider the following induced magnetic field for p polarization:

$$\mathbf{B}_y^{(\mathrm{j})}(\mathbf{r},t) = \left(A_\mathrm{j} e^{ik_{\mathrm{j},z}z} + B_\mathrm{j} e^{-ik_{\mathrm{j},z}z}\right) e^{i(qx-\omega t)}\hat{\mathbf{y}}, \tag{1.38}$$

where q is the in-plane wavevector common to all layers and $k_{\mathrm{j},z}$ is the out-of-plane wavevector of layer j. Using Ampère's circuital law (eq. 1.19) for isotropic media in the absence of currents $\nabla \times \mathbf{B} = \frac{\varepsilon}{c^2}\frac{\partial \mathbf{E}}{\partial t}$ and $\frac{\partial \mathbf{E}}{\partial t} = -i\omega\mathbf{E}$, the electric field reads:

$$\mathbf{E}_x^{(\mathrm{j})}(\mathbf{r},t) = \frac{k_{\mathrm{j},z}c^2}{\omega\varepsilon_\mathrm{j}}\left(A_\mathrm{j} e^{ik_{\mathrm{j},z}z} - B_\mathrm{j} e^{-ik_{\mathrm{j},z}z}\right) e^{i(qx-\omega t)}\hat{\mathbf{x}}, \tag{1.39}$$

$$\mathbf{E}_z^{(\mathrm{j})}(\mathbf{r},t) = -\frac{qc^2}{\omega\varepsilon_\mathrm{j}}\left(A_\mathrm{j} e^{ik_{\mathrm{j},z}z} + B_\mathrm{j} e^{-ik_{\mathrm{j},z}z}\right) e^{i(qx-\omega t)}\hat{\mathbf{z}}. \tag{1.40}$$

For s polarization the electric field is defined as:

$$\mathbf{E}_y^{(\mathrm{j})}(\mathbf{r},t) = \left(A_\mathrm{j}\mathrm{e}^{\mathrm{i}k_{\mathrm{j},z}z} + B_\mathrm{j}\mathrm{e}^{-\mathrm{i}k_{\mathrm{j},z}z}\right)\mathrm{e}^{\mathrm{i}(qx-\omega t)}\hat{\mathbf{y}}, \tag{1.41}$$

and using Maxwell-Faraday equation (eq. 1.20) in our case $\nabla \times \mathbf{E} = -\frac{\partial \mathbf{B}}{\partial t} = \mathrm{i}\omega\mathbf{B}$, the induced magnetic field is:

$$\mathbf{B}_x^{(\mathrm{j})}(\mathbf{r},t) = \frac{k_{\mathrm{j},z}}{\omega}\left(A_\mathrm{j}\mathrm{e}^{\mathrm{i}k_{\mathrm{j},z}z} - B_\mathrm{j}\mathrm{e}^{-\mathrm{i}k_{\mathrm{j},z}z}\right)\mathrm{e}^{\mathrm{i}(qx-\omega t)}\hat{\mathbf{x}}, \tag{1.42}$$

$$\mathbf{B}_z^{(\mathrm{j})}(\mathbf{r},t) = \frac{q}{\omega}\left(A_\mathrm{j}\mathrm{e}^{\mathrm{i}k_{\mathrm{j},z}z} + B_\mathrm{j}\mathrm{e}^{-\mathrm{i}k_{\mathrm{j},z}z}\right)\mathrm{e}^{\mathrm{i}(qx-\omega t)}\hat{\mathbf{z}}. \tag{1.43}$$

Assuming those fields exist at the beginning of each dielectric layer j, it is obvious that the fields after propagating through the layer thickness d_j will acquire the following phase:

$$e^{\mathrm{i}k_{\mathrm{j},z}d_\mathrm{j}}\ (\text{forward}) \quad \text{and} \quad e^{-\mathrm{i}k_{\mathrm{j},z}d_\mathrm{j}}\ (\text{backward}) \tag{1.44}$$

yielding the propagator matrix:

$$P_\mathrm{j}(d_\mathrm{j}) = \begin{pmatrix} e^{-\mathrm{i}k_{\mathrm{j},z}d_\mathrm{j}} & 0 \\ 0 & e^{\mathrm{i}k_{\mathrm{j},z}d_\mathrm{j}} \end{pmatrix}, \tag{1.45}$$

which relates the forward and backward propagating fields at the beginning of the layer j ($z = z_0$) with the corresponding ones at the end ($z = z_0 + d_\mathrm{j}$):

$$\begin{pmatrix} A_\mathrm{j}(z=z_0) \\ B_\mathrm{j}(z=z_0) \end{pmatrix} = P_\mathrm{j}(d_\mathrm{j}) \begin{pmatrix} A_\mathrm{j}(z=z_0+d_\mathrm{j}) \\ B_\mathrm{j}(z=z_0+d_\mathrm{j}) \end{pmatrix}. \tag{1.46}$$

Once those fields are obtained, they must be transferred to the next layer using boundary conditions defined in eq.1.24-1.27. If there are no surface carriers at the interface, we can define the following parameters:

$$\eta_s = \frac{k_{2,z}}{k_{1,z}}, \quad \eta_p = \frac{\varepsilon_1 k_{2,z}}{\varepsilon_2 k_{1,z}}. \tag{1.47}$$

for s and p polarization, respectively. Hence, the transfer matrix relating fields in layer 1 to 2 using these parameters is:

$$T_{m,1\to 2} = \frac{1}{2}\begin{pmatrix} 1+\eta_m & 1-\eta_m \\ 1-\eta_m & 1+\eta_m \end{pmatrix}, \tag{1.48}$$

where m selects s or p polarization. Graphene contribution can also be introduced using an extra parameter per polarization:

$$\xi_s = \frac{\sigma\mu_0\omega}{k_{1,z}}, \quad \xi_p = \frac{\sigma k_{2,z}}{\varepsilon_0\varepsilon_2\omega}. \tag{1.49}$$

The resulting transfer matrix between two dielectrics with graphene at the interface reads:

$$T^G_{m,1\to2} = \frac{1}{2}\begin{pmatrix} 1+\eta_m+\xi_m & 1-\eta_m-\varsigma_m\xi_m \\ 1-\eta_m+\varsigma_m\xi_m & 1+\eta_m-\xi_m \end{pmatrix}, \tag{1.50}$$

where $\varsigma_s = -1$ and $\varsigma_p = 1$.

Applying input fields, the results must fulfill eq. 1.24-1.27 with graphene surface carrier density. Fulfillment of eq. 1.24-1.27 for a graphene layer in vacuum ($\varepsilon_1 = \varepsilon_2 = 1$) and p polarization is going to be explicitly demonstrated. In this case $\eta_p = 1$, $\xi_p = \frac{\sigma k_z}{\varepsilon_0\omega}$, $k_{1,z} = k_{2,z} = k_z$ and the transferred induced magnetic field coefficients in layer 1 (A_1 and B_1) as a function of the field in layer 2 read:

$$\begin{pmatrix} A_1 \\ B_1 \end{pmatrix} = \frac{1}{2}\begin{pmatrix} 2+\frac{\sigma k_z}{\varepsilon_0\omega} & -\frac{\sigma k_z}{\varepsilon_0\omega} \\ \frac{\sigma k_z}{\varepsilon_0\omega} & 2-\frac{\sigma k_z}{\varepsilon_0\omega} \end{pmatrix}\begin{pmatrix} A_2 \\ B_2 \end{pmatrix}, \tag{1.51}$$

which results in:

$$A_1 = A_2 + \left(\frac{A_2}{2} - \frac{B_2}{2}\right)\frac{\sigma k_z}{\varepsilon_0\omega} \quad \text{and} \quad B_1 = B_2 + \left(\frac{A_2}{2} - \frac{B_2}{2}\right)\frac{\sigma k_z}{\varepsilon_0\omega}. \tag{1.52}$$

Next, we substitute this result equation by equation.

From eq. 1.24 we obtain:

$$\begin{aligned} \hat{\mathbf{n}}\cdot(\mathbf{D}_1 - \mathbf{D}_2) &= \varepsilon_0\left(\mathbf{E}_z^{(1)} - \mathbf{E}_z^{(2)}\right) \\ &= -\varepsilon_0\frac{qc^2}{\omega}\left[(A_1 - A_2)\mathrm{e}^{\mathrm{i}k_z z} + (B_1 - B_2)\mathrm{e}^{-\mathrm{i}k_z z}\right]_{z=0}\mathrm{e}^{\mathrm{i}(qx-\omega t)} \\ &= -\varepsilon_0\frac{qc^2}{\omega}\left[A_2 + \left(\frac{A_2}{2} - \frac{B_2}{2}\right)\frac{\sigma k_z}{\varepsilon_0\omega} - A_2 \right. \\ &\qquad \left. + B_2 + \left(\frac{A_2}{2} - \frac{B_2}{2}\right)\frac{\sigma k_z}{\varepsilon_0\omega} - B2\right]\mathrm{e}^{\mathrm{i}(qx-\omega t)} \\ &= -\frac{q\sigma}{\omega}\frac{k_z c^2}{\omega}\left(A_2 - B_2\right)\mathrm{e}^{\mathrm{i}(qx-\omega t)} \\ &= -\frac{q\sigma}{\omega}\mathbf{E}_x \end{aligned} \tag{1.53}$$

which apparently is not the surface carrier density, but including the expression obtained from calculating the divergence of eq. 1.19, we recover the expected result. In eq. 1.25 the magnetic induced field along $\hat{\mathbf{z}}$ is 0 by definition:

$$\hat{\mathbf{n}} \cdot (\mathbf{B}_1 - \mathbf{B}_2) = \mathbf{B}_z^{(1)} - \mathbf{B}_z^{(2)} = 0 - 0 = 0. \tag{1.54}$$

From eq. 1.26 we obtained:

$$\begin{aligned}
\hat{\mathbf{n}} \times (\mathbf{B}_1 - \mathbf{B}_2) &= \mathbf{B}_y^{(1)} - \mathbf{B}_y^{(2)} \\
&= \left[(A_1 - A_2)\mathrm{e}^{\mathrm{i}k_z z} + (B_1 - B_2)\mathrm{e}^{-\mathrm{i}k_z z}\right]_{z=0} \mathrm{e}^{\mathrm{i}(qx-\omega t)} \\
&= \left[A_2 + \left(\frac{A_2}{2} - \frac{B_2}{2}\right)\frac{\sigma k_z}{\varepsilon_0 \omega} - A_2 \right. \\
&\qquad \left. + B_2 + \left(\frac{A_2}{2} - \frac{B_2}{2}\right)\frac{\sigma k_z}{\varepsilon_0 \omega} - B_2\right] \mathrm{e}^{\mathrm{i}(qx-\omega t)} \\
&= \frac{\sigma k_z}{\varepsilon_0 \omega}\left(A_2 - B_2\right)\mathrm{e}^{\mathrm{i}(qx-\omega t)} \\
&= \mu_0 \sigma \frac{k_z c^2}{\omega}\left(A_2 - B_2\right)\mathrm{e}^{\mathrm{i}(qx-\omega t)} \\
&= \mu_0 \sigma \mathbf{E}_x^{(2)} = \mu_0 \mathbf{J}_x,
\end{aligned} \tag{1.55}$$

which is the expected result.

And last, from eq. 1.27 we obtain:

$$\begin{aligned}
\hat{\mathbf{n}} \times (\mathbf{E}_1 - \mathbf{E}_2) &= \mathbf{E}_x^{(1)} - \mathbf{E}_x^{(2)} \\
&= \frac{k_z c^2}{\omega}\left[(A_1 - A_2)\mathrm{e}^{\mathrm{i}k_z z} - (B_1 - B_2)\mathrm{e}^{-\mathrm{i}k_z z}\right]_{z=0} \mathrm{e}^{\mathrm{i}(qx-\omega t)} \\
&= \frac{k_z c^2}{\omega}\left[A_2 + \left(\frac{A_2}{2} - \frac{B_2}{2}\right)\frac{\sigma k_z}{\varepsilon_0 \omega} - A_2 \right. \\
&\qquad \left. - B_2 - \left(\frac{A_2}{2} - \frac{B_2}{2}\right)\frac{\sigma k_z}{\varepsilon_0 \omega} + B_2\right] \mathrm{e}^{\mathrm{i}(qx-\omega t)} \\
&= 0.
\end{aligned} \tag{1.56}$$

that fulfills the condition.

Finally, one may want some physical quantities out of the calculations. To do so, the complete layered system matrix M is needed. It has embedded the total system

response relating the fields from the first (1) and last ($N+1$) layer:

$$\begin{pmatrix} A_1 \\ B_1 \end{pmatrix} = M \begin{pmatrix} A_{N+1} \\ B_{N+1} \end{pmatrix}. \tag{1.57}$$

To compute it, as many propagator and transfer matrices as needed are multiplied in the correct order. M is defined then:

$$M = \begin{pmatrix} M_{11} & M_{12} \\ M_{21} & M_{22} \end{pmatrix} = T_{m,1\to 2} P(d_2) \cdots P(d_N) T_{m,N\to N+1} \tag{1.58}$$

where the transfer matrices may or may not contain graphene.

Under this notation, the Fresnel reflection and transmission coefficients in terms of the elements of M are:

$$r = \frac{M_{21}}{M_{11}}, \tag{1.59}$$

$$t = \frac{1}{M_{11}}, \tag{1.60}$$

and the corresponding reflectance and transmittance read:

$$R_m = |r_m|^2, \tag{1.61}$$

$$T_m = \eta_m |t_m|^2, \tag{1.62}$$

where η_m, in this case, links the first and last layers. Finally, the absorbance is defined as usual:

$$A = 1 - T - R. \tag{1.63}$$

1.2.3.2 FDTD simulations: Lumerical

Lumerical is a commercial software based on FDTD (Finite Differences in Time Domain) which divides the space into rectangular cells in order to calculate the propagation of the fields. Initially, graphene had to be introduced as a material with some volume, thus having to use the permittivity model and input some thickness. Recently, a software update allowed graphene to be introduced as an interface using the model given by [143]. Such a model differs in a factor of 4π on the scattering rate used in 1.2 due to different definitions of the scattering rate. Factor 2 comes from defining τ of the conductivity by the FWHM in one model and by the HWHM

in the other. The additional 2π arises from differences in $\omega\tau$ and $\nu\tau$ convention. Extra details in [143] which follow [144, 145].

This software allows for complete 3D simulations with the only limitation of system processing and memory capabilities to obtain convergence in a reasonable amount of time. Obtaining the transient and the possibility to simulate nonlinear material properties are some extra benefits.

1.2.3.3 RCWA simulations

The RCWA (Rigorous Coupled Wave Analysis) is a simulation method based on scattering matrices to obtain field profiles, reflectance, and transmittance from a multilayer system that is periodically structured in the perpendicular direction [146, 147, 148]. The Matlab script used in this thesis was obtained from Simone Zanotto [149], who used it in [150] and adapted it for us including graphene as an interface with the possibility of graphene nonlocal response (momentum dependence). It is limited to simulate structures with the same periodicity through all their layers.

1.2.3.4 Semi-analytical model

This method was developed and applied by Eduardo Dias and Nuno Peres for the *"Science"* publication [151] and it is similar to RCWA. It considers a layered system like the one depicted in Figure 1.9, whose dielectric layers are numbered from I to V, as shown. The material I and II are air, III is the spacer material (either h-BN or Al_2O_3), IV is SiO_2 and V is Si. The metal was considered to be a perfect electric conductor, and hence it admits no fields inside.

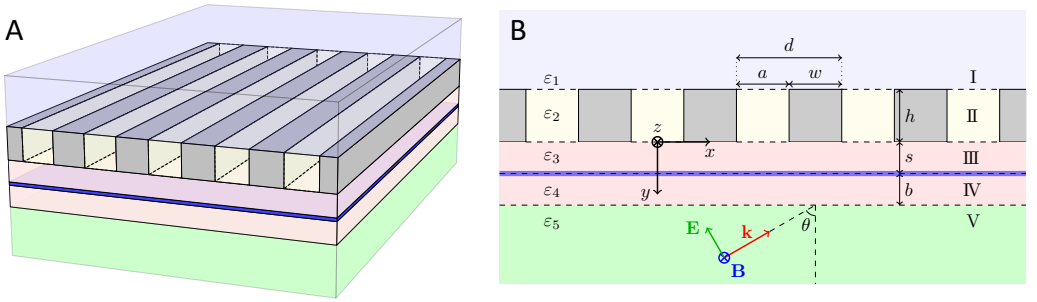

FIGURE 1.9: **A** - Scheme of the considered grating system in perspective view. **B** - Cross-sectional schematics with region and parameter details.

In order to theoretically describe the optical properties of the system,the magnetic field in each dielectric region is decomposed $\mathbf{B}_\nu(\mathbf{r},t) = B_\nu(x,y)\mathrm{e}^{-\mathrm{i}\omega t}\hat{\mathbf{z}}$ as

$$B_\nu(x,y) = \sum_{n=-\infty}^{\infty} \left\{ C_n^+ \mathrm{e}^{\mathrm{i}k_n^{(\nu)} y} + C_n^- \mathrm{e}^{-\mathrm{i}k_n^{(\nu)} y} \right\} \mathrm{e}^{\mathrm{i}\beta_n x}. \tag{1.64}$$

The corresponding electric field follows from Maxwell's equations as $\mathbf{E}_\nu(\mathbf{r},t) = (\mathrm{i}c^2/\omega\varepsilon_\nu)\nabla \times \mathbf{B}_\nu(\mathbf{r},t)$, whereas Bloch's theorem sets $\beta_n = q + 2n\pi/d$ and the EM wave equation yields $k_n^{(\nu)} = [\epsilon_\nu \omega^2/c^2 - \beta_n^2]^{1/2}$. In region V, an additional mode $B_0\mathrm{e}^{-\mathrm{i}k_0^{(1)}y}\mathrm{e}^{\mathrm{i}\beta_0 x}$ is considered, in order to account for the impinging wave. The coefficients C_n^- in region I and C_n^+ in region V are redefined as $B_0 r_n$ and $B_0\tau_n$, respectively, so that the coefficients r_n and τ_n are the usual reflectance and transmittance amplitudes. The coefficients C_n^+ in the region I and C_n^- in the region V are equal to zero, to comply with the boundary conditions (BCs) at $y \to \pm\infty$.

The coefficients in each region are then determined by the inter-layer BCs, which are typically the continuity of the tangential electric field and the (dis)continuity of the magnetic field in the (presence)absence of graphene in the interface. In the interfaces III/IV and IV/V (where there is translational x-invariance), each mode n is diffracted individually, so we obtain a single relation between the nth coefficients in each region. In interfaces I/II and II/III, however, each mode in the region is diffracted into all the allowed modes in the neighboring region, meaning that we obtain each coefficient n as a combination of all the neighboring m coefficients. This yields a matrix equation $\mathbb{M}\cdot\mathbb{C} = \mathbb{S}$, where the elements of matrix $\mathbb{M}$ come from the BCs, $\mathbb{C}$ is a column with the coefficients and $\mathbb{S}$ is the source-term column, related to the impinging wave. This equation is easily solvable (although care should be taken with the convergence of the result), and allows for the determination of all the coefficients which describe the system.

From this point, the reflectance $\mathcal{R}$ and transmittance $\mathcal{T}$ are determined from the coefficients r_n and τ_n as

$$\mathcal{R}(\omega) = \sum_{n\in\mathrm{PM}} \Re\left\{\frac{k_n^{(5)}}{\varepsilon_5}\right\} \Re\left\{\frac{\varepsilon_5}{k_0^{(5)}}\right\} |r_n|^2, \qquad \mathcal{T}(\omega) = \sum_{n\in\mathrm{PM}} \Re\left\{\frac{k_n^{(1)}}{\varepsilon_1}\right\} \Re\left\{\frac{\varepsilon_5}{k_0^{(5)}}\right\} |\tau_n|^2, \tag{1.65}$$

where $\Re\{x\}$ stands for the real part of x, and both summations are performed over the propagating modes (PM). The absorbance, in its turn, is defined as $\mathcal{A} = 1 - \mathcal{R} - \mathcal{T}$.

1.2.4 Plasmons

After having discussed some methods to calculate the optical response of a system containing graphene layers, it is time to explore such response. In particular, plasmon polaritons are the relevant subject to study in the scope of this thesis.

Plasmon polaritons emerge as a solution of Maxwell's equations at the interface of a dielectric ($\Re\{\varepsilon\} > 0$) and a conductor ($\Re\{\varepsilon\} < 0$) consisting of the electromagnetic field and charge carrier density (Fermi sea) coupled oscillations [56].

1.2.4.1 Graphene plasmons

Graphene is susceptible to sustain plasmons because its dielectric permittivity can be negative depending on the frequency and/or E_F as deduced from its positive real part of the conductivity in Fig. 1.5.
Solving for the graphene plasmons dispersion relation reduces to finding the poles of the Fresnel reflection coefficient. Considering a general case of graphene between 2 dielectrics and p polarization, eq.1.59 reads:

$$r = \frac{1 - \eta_{1\to2} + \xi_\sigma}{1 + \eta_{1\to2} + \xi_\sigma} = \frac{1 - \frac{\varepsilon_1 k_{2,z}}{\varepsilon_2 k_{1,z}} + \frac{\sigma_g k_{2,z}}{\omega\varepsilon_0\varepsilon_2}}{1 + \frac{\varepsilon_1 k_{2,z}}{\varepsilon_2 k_{1,z}} + \frac{\sigma_g k_{2,z}}{\omega\varepsilon_0\varepsilon_2}}. \tag{1.66}$$

which in the electrostatic approximation ($k_{j,z} = iq$) reduces to:

$$r \approx \frac{\varepsilon_2 - \varepsilon_1 + i\frac{\sigma_g q}{\omega\varepsilon_0}}{\varepsilon_2 + \varepsilon_1 + i\frac{\sigma_g q}{\omega\varepsilon_0}}. \tag{1.67}$$

We find the dispersion relation (poles of the Fresnel reflection coefficient) by equating the denominator to zero:

$$q \approx i\frac{(\varepsilon_1 + \varepsilon_2)\omega\varepsilon_0}{\sigma}. \tag{1.68}$$

If Drude conductivity of graphene is used and terms are rearranged, the well-known approximated dispersion relation for graphene plasmons is recovered [140]:

$$\frac{\lambda_p}{\lambda_0} \approx \frac{4\alpha}{\varepsilon_1 + \varepsilon_2}\frac{E_F}{\hbar\omega}. \tag{1.69}$$

To observe the graphene plasmons dispersion relation in a color-plot we might look at the system losses, i.e. the imaginary part of the reflection coefficient. Plasmons will appear as high loss features (see Fig. 1.10).

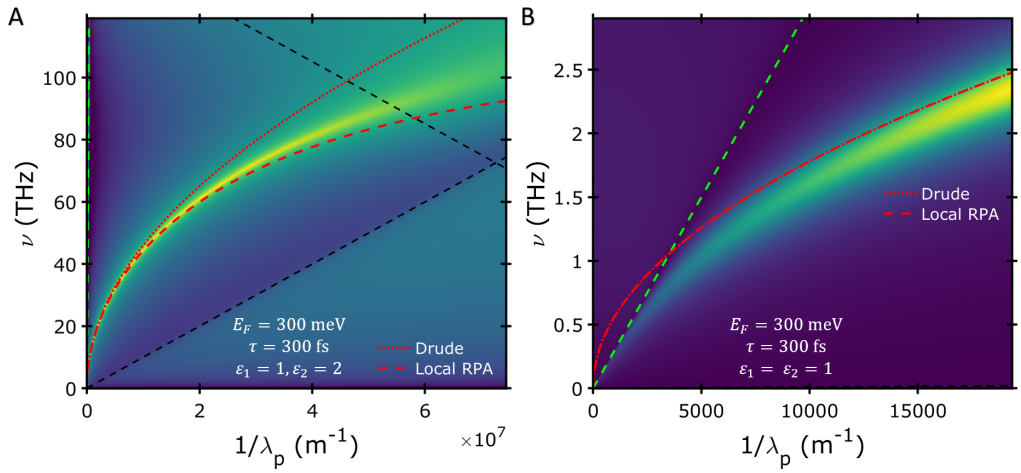

FIGURE 1.10: Graphene plasmons dispersion relation

Example of dispersion relation using the $\Im\{r\}$ from eq.1.66 with nonlocal RPA conductivity. Cyan and red dashed-lines correspond to Fermi velocity and the speed of light. The spectral spread of the feature provides information about the plasmons' lifetime. Solutions to eq.1.68 using Drude and local RPA conductivity are represented as green dotted and dashed lines, respectively. Electrons relaxation time $\tau = 30$ fs in **A** and $\tau = 300$ fs in **B**. We can observe noticeable discrepancies between Drude, local and nonlocal conductivity for large momentum. On the small momentum regime, the electrostatic aproximation clearly fails.

Chapter 2

Screened graphene plasmons

It is known that at the interface of a dielectric and metal, there is a solution to Maxwell's equations for p-polarization which consists of a surface propagating wave that is a coupled mode of electromagnetic fields (EM-fields) and Fermi sea electron's oscillations. Such waves are called surface plasmons and have greater momentum than light i.e. they are evanescent waves and do not propagate through the bulk. Thanks to its greater momentum, the EM-fields are more confined thus increasing the energy density. However, field confinement factor using metals is on the order of 4 to 10 even if the metal layer is thinned down to a few nm [56].

Graphene plasmons emerged as a novel platform for enhanced light-matter interaction studies [82, 83, 84, 85, 91, 92, 95, 32, 97, 96, 93, 94] impulsed by field confinement factor on the order of 100 for Mid-IR (see eq.1.69) [76, 77, 152, 153, 154, 155, 156, 157, 158] and the possibility of high energy density [78, 79, 80, 81, 140]. This fact, drove the field into investigating Bio-sensing using graphene plasmonics [159, 160, 161] and nonlinear optics [114, 115, 121, 129, 130], and still more applications to come.

Conversely, most of the confinement effects are given at small E_F values, which causes the energy density to be moderate and the graphene plasmon modes extremely weak and inefficient in this regime. It is desirable to observe such confinement levels at high E_F values in order to obtain even higher energy density and stronger plasmonic signatures to study the light-matter interaction.

With the previously mentioned goals in mind, the combination of extended graphene with metallic periodic nanostructures at a certain vertical distance determined by a spacer material is used to reach the requirements. It results in a hybrid structure presenting hybrid graphene plasmon resonances as it will be further detailed later on in the text. The main advantage of the structure is the larger in-coupling to highly confined plasmons, leading to stronger signals than with the single-pass of light designs such as graphene nanoribbons. Additionally, it is non-invasive because graphene doesn't need to be etched and as a consequence, it preserves its

quality. It enables us to observe plasmons from high-quality graphene even with far-field (FF) techniques such as transmission in an FTIR microscope.

On the other hand, to complete the study presented in this thesis, one needs a plethora of different devices that reliably provide a decent signal. CVD grown graphene was chosen for ease of fabrication and for its large area coverage, which allowed us to have many different devices in the same chip. However, long and delicate nano-lithography processes needed to be done to obtain the different metal nanostructures on top.

This chapter will deal with graphene plasmons and their relation in the hybrid structure as well as the characterization of the main structure parameter effects.

2.1 Optical vs. acoustic plasmons

Remember the well-known approximated dispersion relation for single layer graphene plasmons (SLGP) reads [140]:

$$\frac{\lambda_p}{\lambda_0} \approx \frac{4\alpha}{\varepsilon_1 + \varepsilon_2} \frac{E_F}{\hbar\omega}; \tag{1.69}$$

where λ_p, λ_0 are the plasmon and free space wavelengths, correspondingly. $\alpha \approx 1/137$ is the fine structure constant, ε_i is the dielectric permittivity of the materials above (i =1) and below (i =2) graphene. Finally, Fermi energy (E_F) or chemical potential (μ) and the excitation energy ($\hbar\omega$) complete the variables used. It is now easy to observe the linear dependence $\lambda_p \propto E_F$ and the square root dispersion relation $\hbar\omega \propto \sqrt{1/\lambda_p}$. Being $1/\lambda_p$ the plasmon in-plane momentum (k_p) divided by 2π. Remember that eq.1.69 considers local conductivity (no momentum dependence, valid for $q \ll k_0 c/v_F$) in the electrostatic approximation ($q \gg k_0$).

Double-layer graphene, in contrast to single-layer graphene, presents two plasmonic modes that arise from the interaction of both single graphene layers. The modes' solution of two equally conducting SLG separated by a distance $2L$ reads [162]:

$$\text{a)}\ \frac{i\sigma}{\omega\varepsilon_0} + \frac{\varepsilon_1}{\kappa_1} + \frac{\varepsilon_2}{\kappa_2}\tanh(\kappa_2 L) = 0; \quad \text{b)}\ \frac{i\sigma}{\omega\varepsilon_0} + \frac{\varepsilon_1}{\kappa_1} + \frac{\varepsilon_2}{\kappa_2}\coth(\kappa_2 L) = 0; \tag{2.1}$$

with $\kappa_i = \sqrt{k_p^2 - \varepsilon_i \omega^2/c^2}$ and sub-index i =1 (2) indicates substrate (spacer) material.
The symmetric plasmon modes observed -solution of Eq.2.1,a- are called optical plasmons (OP) and they are shifted towards higher energy with respect to SLGP.

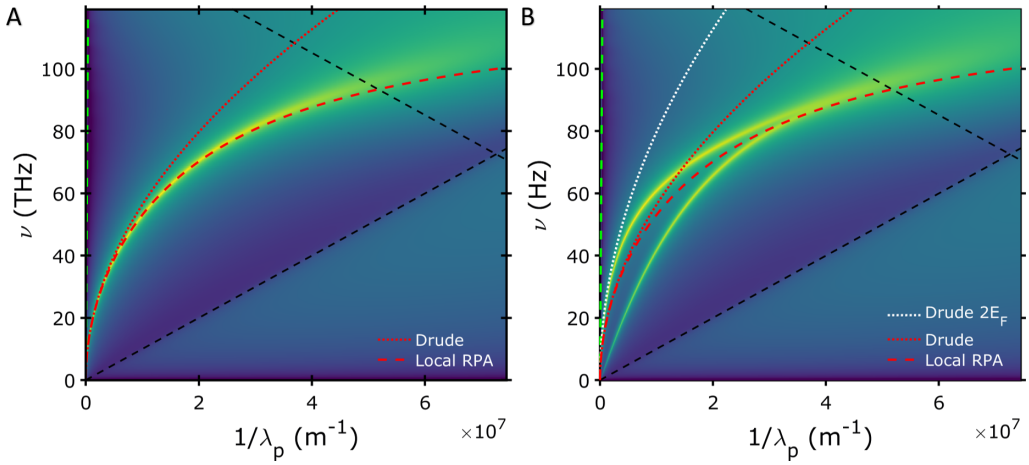

FIGURE 2.1: Optical response of single **A** and double layer **B** graphene in vacuum. $E_F = 0.3$ eV, $\tau = 300$ fs and distance between layers $d \cdot k_F = 1$.

On the other hand, the plasmon modes found at lower energy -solution of eq.2.1,b- are called acoustic plasmons (AP) and they are anti-symmetric (see Fig. 2.1).

At low energy, mode splitting is noticeable and disappears at higher energy/momentum. For this higher energy/momentum, both modes merge together resembling the SLG plasmon dispersion (see Fig. 2.1,B). Mentioned merge point and mode splitting depend heavily on the separation between SLG ($2L$). The larger the distance between SLG, the closer the system behaves to two isolated SLG, while merge point and mode splitting are reduced. On the contrary, for close proximity, mode splitting is greater and the merge point might not even occur. The mode at higher energy approximates to a SLG with double E_F (see white dotted line in Fig. 2.1,B).

All the effects mentioned can be easily interpreted using approximations in Eq.2.1. In the limit of $\kappa_2 L \ll 1$ mode splitting is large while in the $\kappa_2 L \gg 1$ limit, both equations become equal and hence, both layers present the same SLG modes.

In the OP mode, the charge distribution is symmetric with respect to the plane of separation of both layers. In other words, equal charge distributions are aligned vertically in both SLG, thus causing the field to be higher above and below the DLG. Conversely, AP modes are anti-symmetric, equal charges of opposite sign are aligned vertically, hence creating larger fields between layers (see Fig. 2.2A).

From the field profile, one can foresee an alternative approach to obtain AP. By placing a metal layer at half the spacing than in the DLG system; and thanks to the metal screening of the field, the same anti-symmetric field profile is recovered (but

in half of the space). An example is depicted in Fig. 2.2,b.

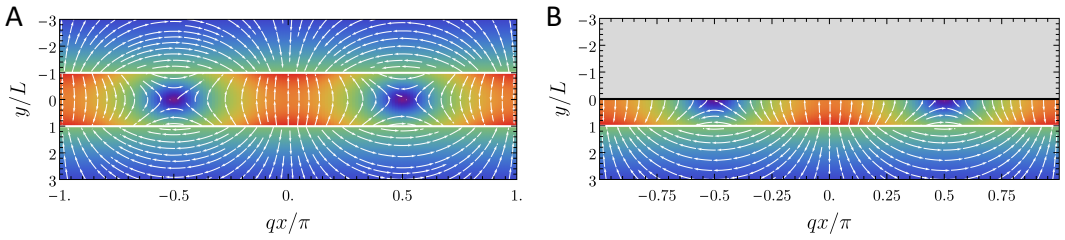

FIGURE 2.2: Field comparison double-layer graphene **A** and graphene-metal **B**.

Using only SLG plasmons, one can obtain larger confinement (larger k_p) at a given excitation energy by lowering E_F (in magnitude), but with a corresponding reduction of the plasmon field strength (see Fig. 2.3,a). Notwithstanding the above, high confinement and high field strength can be achieved with the use of AP. Even at high E_F, if a metallic layer is placed at a nanometric distance from a SLG, the lateral confinement (k_p, q) is increased due to the metal screening (see Fig. 2.3,b). This effect was known in the 2DEG community but there were limitations on the separation between the 2DEG and the metal gates [65, 66, 67].

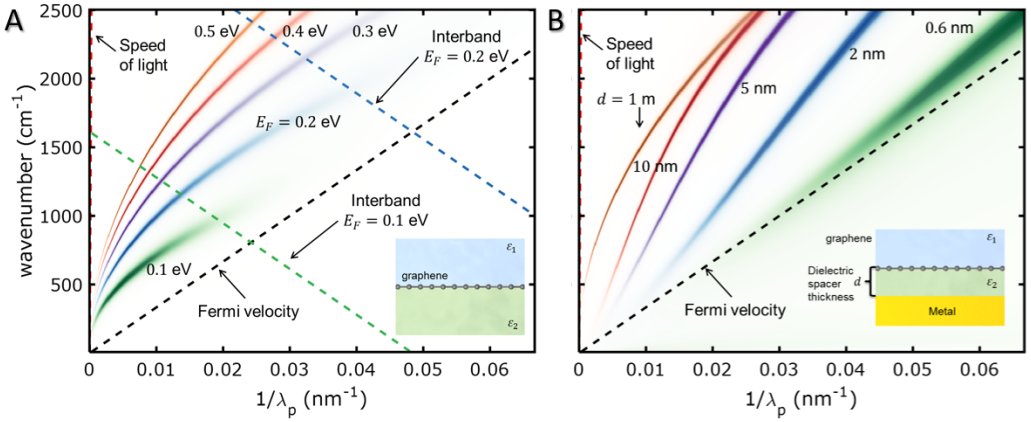

FIGURE 2.3: **A** - Optical graphene plasmons dispersion relation for decreasing E_F (orange to green). **B** - Acoustic graphene plasmons dispersion relation at $E_F = 0.5$ eV for decreasing spacer thickness (orange to green).

A clearer picture of the confinement (lateral and vertical) as a function of the metal-graphene distance is represented in Fig. 2.4 for given excitation energy. It should be noted that different spacer material with different dielectric permittivity yields different plasmon wavelength even with no metal around as shown by eq.1.69.

This fact reduces the effect of the metal screening because the field is already more confined (see Fig. 2.4 mode index difference between Al_xO_y and h−BN).

The fundamental limitation of q related to electron velocity in graphene is indicated as a horizontal dashed line for mode index $\frac{\lambda_0}{\lambda_p} = \frac{c}{v_F}$ =300. It indicates the maximum momentum a plasmon (coupled-wave between light and electron oscillations) may support before being over-damped by Landau interband transitions. In parallel, there also exists another fundamental limitation for confinement in the vertical direction: one atom thick spacer layer. In other words, one atom is the minimum distance we can separate metal and graphene apart. If there was a thinner than an atom vacuum spacer, it could be considered that both materials are in contact, thus not "spaced". Even if they were not in strict contact, electrical interaction between them will affect the local band structure; leading to what could be understood as a hetero-junction. Nonetheless, said interaction is out of the scope of this thesis.

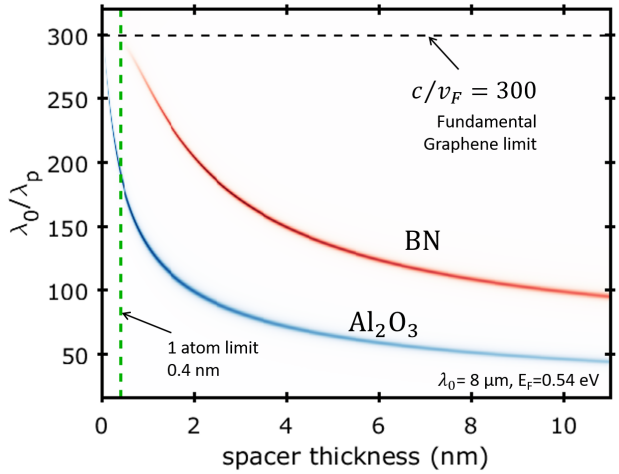

FIGURE 2.4: Spacer material and thickness dependence of Acoustic Plasmons. The spacer thickness represents the vertical confinement (when the out-of-plane decay length of the field is larger than the spacer thickness) with the bottom limit of 1 atom. Mode index (λ_0/λ_p) represents the lateral confinement and it is limited in graphene to 300, where light would have the same group velocity as electrons in graphene and it will absorbed.

2.2 Far field excitation

In the previous section, it was discussed how the dispersion relation of plasmonic modes in graphene can be affected by the proximity of a metal layer. Despite the advantageous properties of AP, these modes in planar structures are difficult to

access in the MidIR even for nano-probing techniques [34, 82, 83, 84, 85] because of the extremely small λ_p. Nonetheless, they have been studied at THz frequencies where λ_p is indeed larger and hence, accessible to s-SNOM. The study unveiled outstanding knowledge about quantum electron dynamics in graphene [88] such as Fermi velocity re-normalization or e-e interactions.

In this section, the method used to study AP resonances is presented. It overcomes the light-AP momentum mismatch and provides a platform to sustain AP resonances observable from far-field (FF). Similarly to standard SLGP resonances where graphene itself was nanostructured, some sort of structure is needed to provide both momentum and a resonant cavity [32, 85, 91, 92, 93, 94, 95, 96, 97]. In this thesis case, it was decided to structure the metal layer instead, as it was done for the so-called gate plasmons in 2DEGs [65, 66, 67].

Before putting the above-mentioned approach in practice, some FDTD simulations were performed in order to estimate the validity of the method. The results comparing graphene etched ribbons and screened graphene plasmon (SGP) structures with equal periodicity and duty cycle are shown in Fig. 2.5. One can immediately distinguish differences in the field intensity distribution of the fundamental resonance and in the extinction values, even for high order resonances as well. Graphene etched ribbons focus the light into "hot spots" at its edges of evanescent nature, i.e. the field decays exponentially away from the edge. On the other hand, for SGP, most of the field is confined in the spacing region between continuous graphene and the metal ribbon.

It is assumed further on, that metal ribbon width defines, in a major proportion, the plasmon resonance cavity. A smaller contribution is observed from the field which couples adjacent ribbons (SLGP). Extra freedom of selecting the amount of confinement and the resonance frequency is obtained by carefully choosing the spacing material and its thickness.

In order to obtain some more system insights, simulated electric field lines are depicted in Fig. 2.6. One may see a horizontal dipole-like field distribution emerging from in between the metal ribbons. They are created by oscillating charge carrier densities of opposite sign at the lateral faces of adjacent ribbons (like a tiny capacitor). Such an effective dipole with high momentum near-field components might be responsible to excite SGP and SLGP in the system as well. Another possibility comes from the idea that momentum is provided by sharp edges of the nanostructures. In any case, the metallic ribbon array contributes by launching and modifying SGP properties at the same time that creates a plasmonic cavity. A recent study [161], later than the publication leading to this thesis chapter [151], suggests scattering from far-field into both types of plasmons and additional conversion between

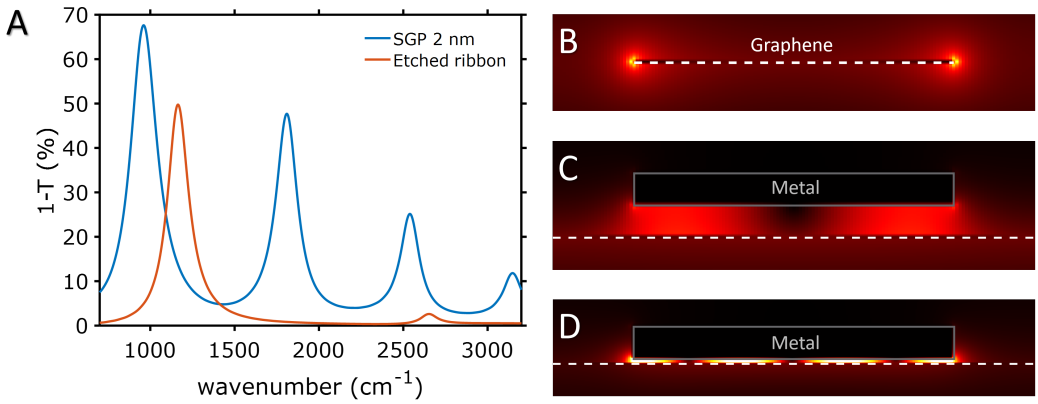

FIGURE 2.5: **A** - Simulated extinction of the plasmonic resonances for graphene ribbon array of w = 100 nm (orange) and for an array of 100 nm wide gold rod (blue) situated 2 nm away from continuous graphene in vacuum (the period is 120 nm in both cases). **B,C,D** - Simulated field magnitude profiles at resonance for a graphene nanoribbon (**B**) and w = 100 nm metal rods at 10 (**C**) and 1.5 nm (**D**) distance from graphene with a 150 nm period (same linear colorscale for all).

them afterward.

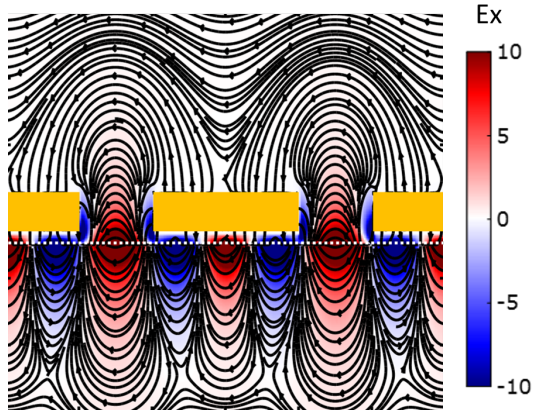

FIGURE 2.6: Field lines at plasmonic resonance showing the dipolar character of the excitation. In-plane electric field in color-scale. Graphene position is marked with a white dotted-line.

2.3 Sample fabrication/ characterization

With a better understanding of the working mechanisms, a schematic device is shown in Fig. 2.7. It consists of CVD graphene field-effect transistors (FET) on a low doped Si-SiO_2 wafer, encapsulated with a thin dielectric film/layer and terminated with a periodic array of metallic ribbons. The devices are designed to be measured in transmission using an FTIR (Fourier transform infrared spectrometer) microscope in the Mid-IR spectral region. Gate-dependent extinction referenced to CNP will be measured for several device parameters such as metal ribbon width (w), gap width (g), spacer thickness (s) or material.

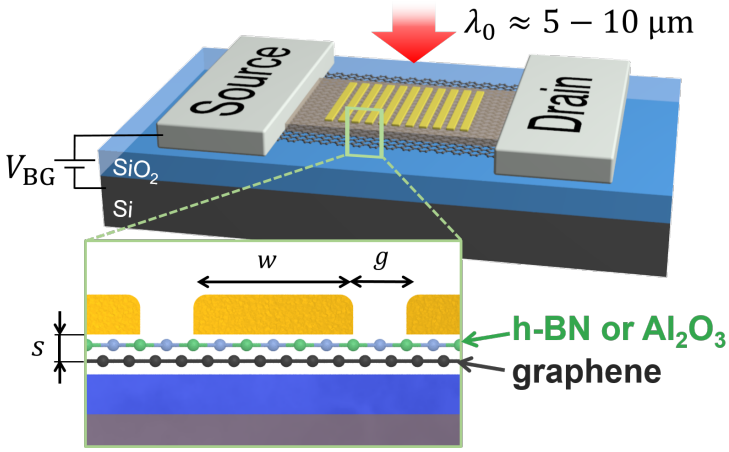

FIGURE 2.7: Graphene FET with metallic ribbons general and detail (inset) schematics.

The samples consist of 800 μm long and 120 μm wide CVD graphene stripes (dark gray rectangles with blue perimeter in Fig. 2.8). CVD graphene (obtained from ©Graphenea) was obtained from a Cu foil where it was grown on both sides and one of them spin-coated with polymethyl methacrylate (PMMA). Dry-etching of the back graphene and wet-etching of the Cu layer were performed. A layer of graphene with PMMA floating on ammonium persulfate results. After being transferred 3 times onto de-ionized water (where it also floats), graphene was wet-transferred onto the Si-SiO_2 wafer piece with already deposited source and drain contacts. The final shape of the stripes was done with oxygen plasma using a polymer mask created by optical means. Encapsulation of several nanometers Al_2O_3 or HfO_2 is done using atomic layer deposition (ALD) over the whole piece. Finally, a PMMA mask with the ribbon arrays form is shaped using electron beam lithography (EBL) and consequent metal deposition and lift-off were conducted. Such arrays occupy an area of 100 by 100 μm^2. They were placed deliberately on and

off graphene for reference purposes. The arrays consist of 9 μm long horizontal ribbons arranged in 10 columns separated by 1 μm. Ribbons' nominal width and periodicity vary from graphene stripe to graphene and are reproduced in the adjacent reference column. Inside each stripe/column, the EBL dose (exposure time) increases vertically. This last parameter finally defines the final width of the ribbons (some variation from the nominal width).

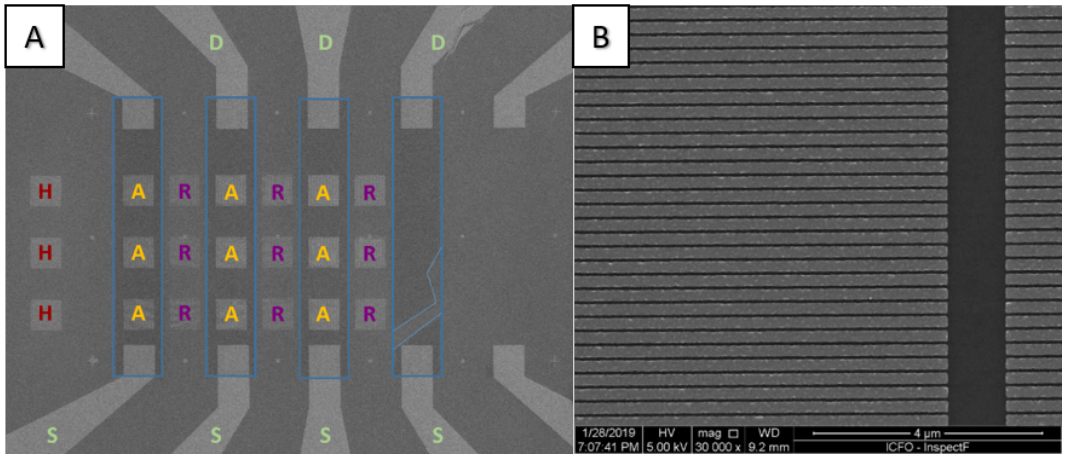

FIGURE 2.8: Sample scanning electron microscopy (SEM) micrographs. **A** - Complete sample including source-drain (S-D) contacts, active (A) and reference (R) areas with metal ribbon arrays on and off graphene, respectively, and homogeneous (H) metal layer off graphene. **B** - Detail image of a 250 nm period array of metal ribbons active area.

Before the study of the whole system (including graphene and its gate tunable optical response), it is mandatory to understand the effects of the metallic ribbon arrays (or grating) alone, i.e. with no graphene contribution. Their effect on transmission is shown in Fig. 2.9 for light polarized perpendicular (a) and parallel (b) to the ribbon longest dimension. Starting with perpendicular polarization, one can appreciate 2 main features: first, a sharp dip between 1000 and 1500 cm^{-1} corresponding to grating enhanced absorption of SiO_2. And second, a metal width tunable transition from high to low transmission. A naif explanation of the effect is explained by the inability of the electrons to screen the incident field. When the metal plasmon wavelength is larger than a factor times the ribbon width, the electrons accumulate at the ribbon sides, which creates an intense near-field between ribbons that allows propagation through the grating. Unlike for perpendicular polarization, if the incident field is polarized parallel to the ribbon length, the incident wavelength is shorter than the ribbon length thus the electrons "have space" to screen the field completely. Some deviation is observed in the experiment when compared to the

homogeneous metal case due to the finite length of the ribbons and the 90% area coverage. It is worth mentioning that the incident polarization is controlled with a wire grid holographic polarized, which is, in essence, the same type of system than the grating on our substrate.

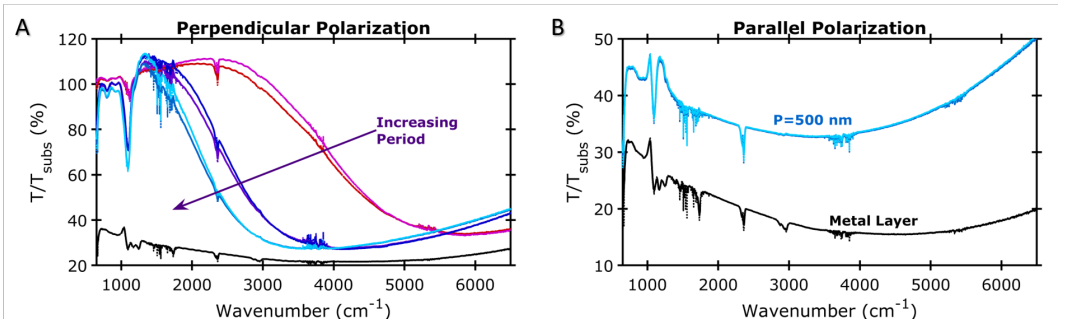

FIGURE 2.9: Grating effects on transmission using substrate's transmission as reference for polarization across (**A**) or along (**B**) the ribbons. Device nominal widths are 200, 300 and, 400 nm with 100 nm nominal gap.

2.4 Characterization of the optical response

In this section, the experimental dependence of the device parameters is studied. The basic electrostatic gate tuning knob will provide the basis to analyze the results for the material and geometric parameters. Thus, it will be the first one to be explored. Next it is continued with the geometrical parameters: array period (p), metal width (w), gap width between metal ribbons (g), and spacer thickness (s).

2.4.1 Fermi Energy

The first and most important parameter to study is the charge carrier density (also known as chemical potential or Fermi energy E_F), which brings one of the main characteristics of graphene: its in situ electrical tunability. Since graphene is a monolayer of carbon atoms, it is easy to electrostatically tune the number of charge carriers. The Fermi energy dependence is the basic measurement through this thesis because it allows us to extract the gate voltage-dependent extinction (referenced to CNP), and compare it through all the parameters at the same carrier density.

In metals, the plasma frequency is proportional to the square root of the charge carrier density (n_e). The plasma frequency, in turn, determines the plasmonic response of the material, at which energy it starts absorbing light, and consequently the metal color. In general, if no other material parameter is changed, for larger n_e

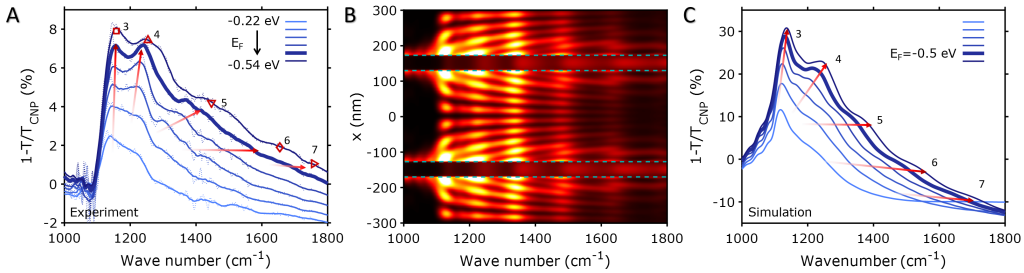

FIGURE 2.10: E_F dependent extinction of 2 nm thick Al_2O_3 spacer, 240 nm metal width and 60 nm gap width device. **A** - experiment, **B** - simulated field at graphene at the bold line doping ($E_F = 0.5$ eV), and **C** - simulated gate tunable extinction.

(plasma frequency), the plasmon wavelength at a given frequency is longer; which is true not only for metals but also for graphene. The case of SGP is equivalent to the prior mentioned with the advantage of dealing with much smaller n_e and the possibility of in situ tunability. Experimentally, a given SGP structure will be resonant for a fixed $\lambda_p \equiv \lambda_{p0}$ and its multiples (see Fig. 2.10). From the dispersion relation at a given $|E_F|$, we will find the corresponding resonant excitation wavelengths λ_0 by matching with λ_{p1} and its multiples. If $|E_F|$ is increased, then, the corresponding λ_{p2} for the previous λ_0 excitation is increased $\lambda_{p2} > \lambda_{p1}$ due to larger n_e and it is no longer resonant with the structure λ_{p0}. In this situation, the new resonant condition is moved towards higher excitation energy $\lambda_1 < \lambda_0$ (blue-shifted). In the case of multi-mode resonant structures (structures that support more than a single resonant mode); such as the one studied in Fig. 2.10, the higher-order modes shift more rapidly than lower-order ones. This effect causes the multiple resonances to be mainly distinguished (separated) at high $|E_F|$, especially for highly dispersive dielectric substrates as SiO_2 with modes clustered between the TO (transverse optic at 1080 cm^{-1}) and LO (longitudinal optic at 1250 cm^{-1}) phonon energies at low doping values.

2.4.2 Geometrical parameters

Disentangling the effects of some lateral geometric parameters is rather hard experimentally. Meanwhile, the vertical direction presents higher fabrication accuracy and the spacer thickness does not affect the other parameters. Since it is needed to establish the effect and relation of the lateral parameters first, the spacer dependence is going to be studied last. The fabricated structures present deviations from the nominal values (in the in-plane dimensions) due to the e-beam lithography process. Usually, the structure period is repeatable from device to device within a few

nm tolerance, which only depends on the writing field resolution. The most affected parameters are the ribbon width and the gap width: a small difference in the dose (exposure time) will affect the gap/width ratio and duty cycle (width/period), making them quite hard to separate. For that reason, it is tried to bring light to it first.

2.4.2.1 Width/period dependence for constant gap

Two prominent features in the transmission extinction curves are noticed when studying the lateral dimensions parameters: the metal and the gap widths, and the period. First, a broadband increase of the system transmission (negative extinction); and second, a narrow-band increase of the absorption (positive extinction). The prior effect is a broadband modulation of the system impedance caused by an increment of graphene's $|E_F|$ (Fig. 2.11A). On the other hand, increased doping in graphene also leads to increased narrow-band ($\sim 100\ \mathrm{cm}^{-1}$) absorption(Fig. 2.11,b). The later is associated with SGP resonances which are the interest of this work.

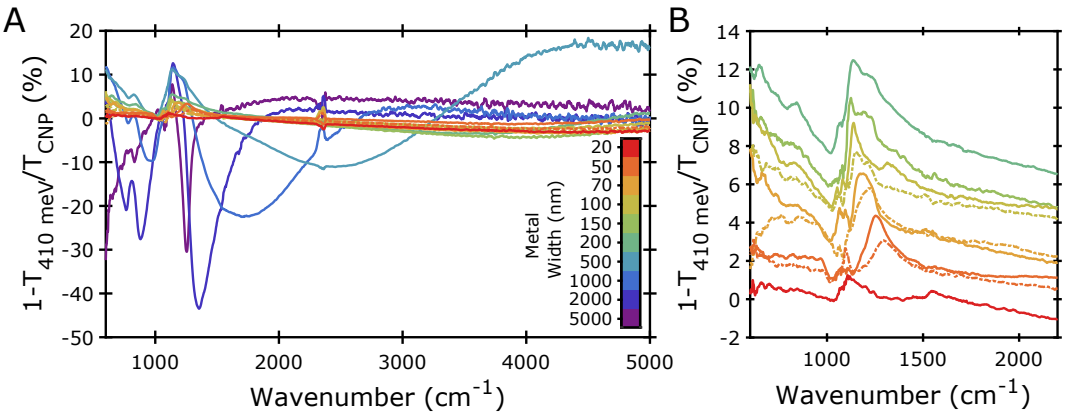

FIGURE 2.11: Metal width dependence of 3 nm Al_2O_3 device extinction with a nominal gap width of 50 nm. **A** - Full spectral range all devices with no offset. **B** - Narrower spectral range of selected smaller devices, with extinction offset for clarity. The color-coded metal width values represent the nominal design values. The real values differ on higher (solid lines for wider ribbons of the same period) or smaller (dash-dotted lines for narrower metal ribbons of the same period) EBL dose.

The broadband increased transmission in Fig. 2.11,a red-shifts for larger metal widths in the same way that the transition region from high to low transmission of the gratings themselves (Fig. 2.9,a). Additionally, it is observed a stronger effect for larger structures with high duty cycles (> 90 %). It can be interpreted as graphene modulating the EOT (extraordinary optical transmission) of the metal ribbon array,

where the effective inter-ribbon dipoles heavily interact with graphene via near-field. At low doping values, vertical and non-vertical transitions are available due to the large momentum components of the dipole, providing stronger absorption than fundamentally expected 2.3 % ($\pi\alpha$) for vertical transitions (plane waves or light momentum approximated to 0) in a vacuum environment. Once $|E_F|$ is large enough, part of these transitions are blocked and transmission starts to grow in the grating transition region.

If we focus now only on the SGP resonances (Fig. 2.11,b), we observe how the narrower structures yield fundamental resonant frequency at higher energies. In other words, the resonant energy red-shifts with metal width/ structure period as expected: the larger the cavity, the larger the wavelength that fits in. Even if the fundamental mode of a structure is located at a lower frequency, thanks to the strong response of high order modes, it is possible to observe SGP resonances at shorter wavelengths than those of the smaller structures fundamental. As an example, the orange curves in Fig. 2.11,b have broad "peaks" around 2000 cm^{-1} while the narrowest structure peaks around 1600 cm^{-1}. The fabricated structures with lower EBL dose (dash-dotted lines) presenting narrower ribbons than the higher dose counterparts, still show the same trend but slightly blue-shifted and weaker. It is possible to reaffirm that the main parameter controlling the SGP resonance position is the metal width and the gap has a major influence in the resonance strength and relatively minor in the peak position.

Fig. 2.12 summarizes the effects up to this point by the use of RCWA simulations (see 1.2.3.3) for single excitation wavelength, constant gap and varying metal ribbon width/structure period. Firstly, one observes the system transition from transmissive to reflective for wider metal ribbons (equivalent to increase/decrease the excitation wavelength λ_0). Secondly, introducing graphene in the system modifies its response by inducing higher absorption due to interband transitions. And thirdly, SGP resonances appear at large doping thanks to the near-field created by the joined effects of metal ribbons and graphene.

2.4.2.2 Gap/period dependence for constant width

The next experimental parameter to be considered is the gap width. A sample with two sets of gap widths for several metal widths was fabricated to study its effect (Fig. 2.13). Regarding the broadband increased transmission, it is observed that a larger gap generally reduces the transmission and blue-shifts its maximum effect (see Fig. 2.13A). Conversely, small gap widths enhance SGP absorption, especially for larger momentum due to the stronger dipole created. It can also slightly modify the resonant condition because the period is modified or because the coupling between adjacent ribbons is changed. Additionally, there might be SLGP contribution

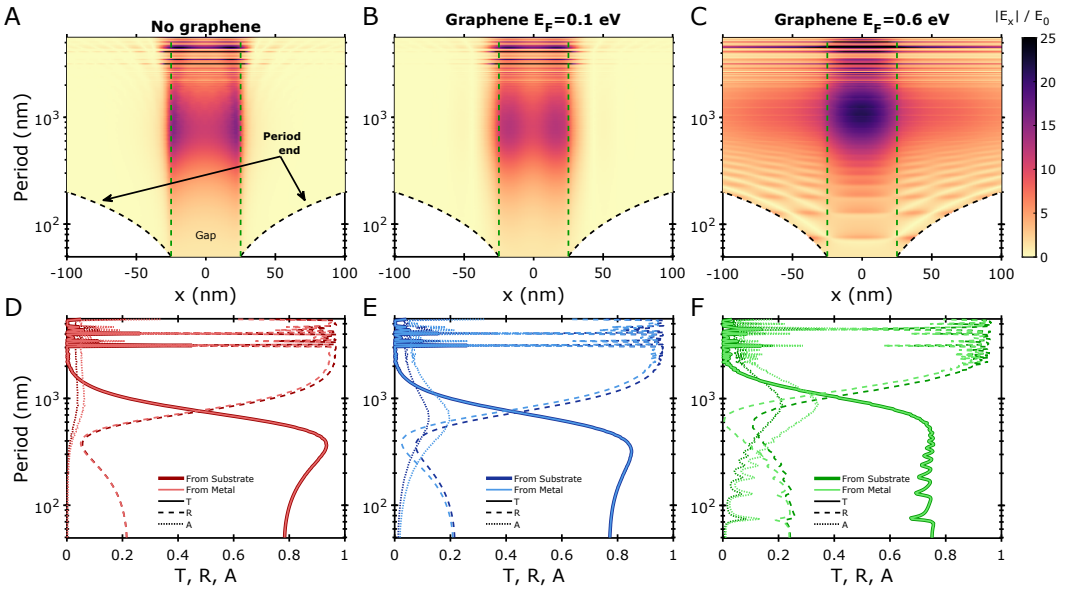

FIGURE 2.12: RCWA simulated in-plane field magnitude at graphene position with $\lambda_0 = 5.5$ μm excitation and increasing period for a constant gap size for the cases of no graphene (**A**), low doped graphene (**B**) and high doped graphene (**C**). **D** to **F**, optical response (Transmission, Reflection and Absorption) corresponding to **A**-**C** for top (light color, from the grating side) or bottom (dark color, from the substrate side) illumination.

in the gap under certain doping and geometry conditions (see the lack of field in the metal region around 1570 cm^{-1} in Fig. 2.14,c).

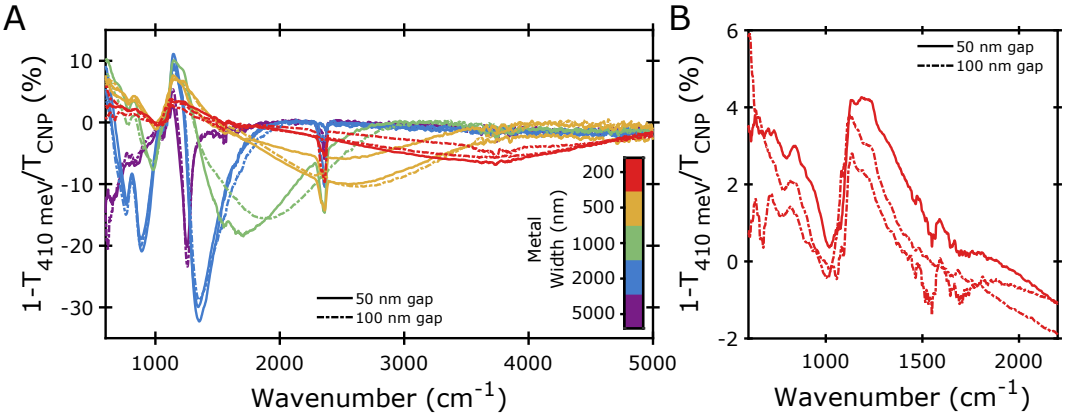

FIGURE 2.13: Gap width dependence of 4 nm thick HfO_2 device extinction. **A** - Full range no offset. **B** - Smaller range of 200 nm width devices. Color-coded metal width values represent nominal design values; real values may differ. Solid (dash-dotted) lines for 50 nm (100 nm) gap width. The 50 nm gap curve in B is offset 1 % vertically.

An easy approach to observe the gap width is using the help of simulations: either by increasing the gap width continuously (similarly to Fig. 2.12) and observing the field profiles either by comparing the extreme cases of a small period structure with a single ribbon structure. The latter hasn't been studied experimentally because the expected signal to noise (S/N) ratio is extremely low in the single structure case. It has been studied with the use of FDTD simulations Fig. 2.14 instead. The main characteristic to be observed is the similarity of the field distribution both in section (Fig. 2.14,a and b) and the spectral and spacial field distribution at graphene position (Fig. 2.14, c and d), despite a gap SLGP contribution around ~ 1570 cm^{-1} in the periodic case. It should be noted 2 orders of magnitude difference in the electric field modulus, being that the reason not to try it experimentally.

With the perspective given by time, it could have been studied an array of ribbons with a gap larger than several times the SLGP propagation length (at least 4 or 5 times larger). However, the signal could have been still too small and our interest at this point was not in the single structure yet. The experimental study of single/non-coupled structures is left open for future investigations.

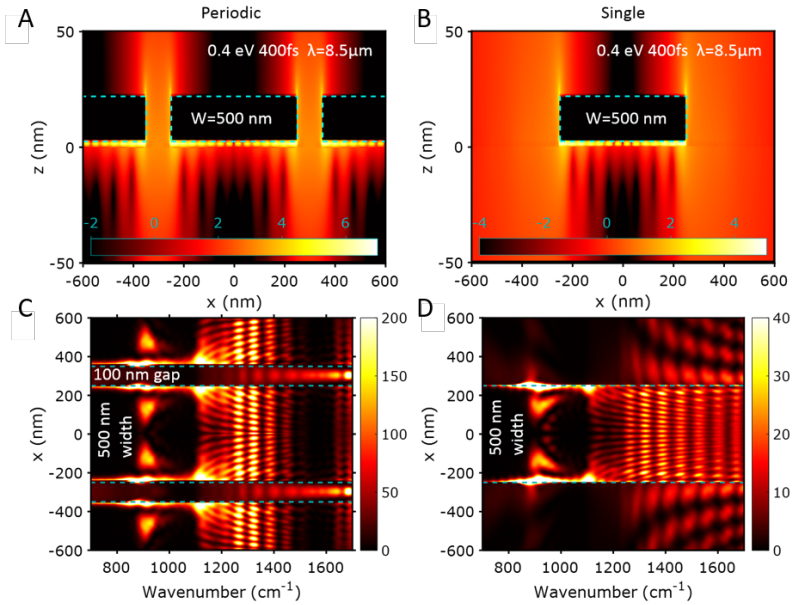

FIGURE 2.14: Comparison of FDTD simulated single and periodic structures. Cross-section with graphene at $z = 0$ and logarithmic color-scale for periodic (**A**) and single structure (**B**) devices. **C** and **D** are the spectral field distribution (field in linear color-scale) on graphene corresponding to **A** and **B** structures, respectively, for the length of two periods.

2.4.2.3 Spacer thickness dependence

The last parameter to be studied experimentally is the spacer thickness (see Fig. 2.15). It controls the screening of the metal layer and vertical confinement directly, and the lateral confinement is obtained as a consequence. Control of confinement in the out of plane direction is easy assuming a perfect metal: all the electric field must be confined between graphene and metal (if it did not vanish earlier as for large graphene metal separations). s is directly the upper limit of the confinement in the z-direction.

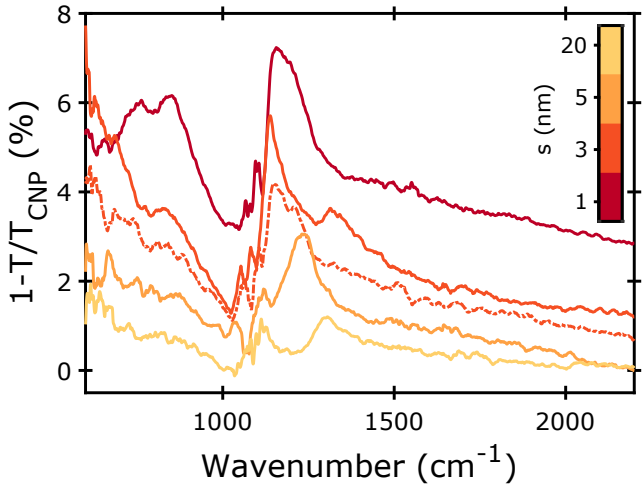

FIGURE 2.15: Al_2O_3 spacer thickness dependence of the device extinction for similar E_F doping, 100 nm period and 50 nm nominal metal width. The curves have been offset vertically in 1, 3, and 5 by 4 %, 1.5 %, and 1 %, respectively. The dash-dotted line corresponds to a device with lower EBL dose, hence, narrower metal ribbon.

In-plane confinement is not straight forward, yet approachable. From Fig. 2.3,b it is clear that a given grating structure with a resonant λ_p will exhibit a decreasingly lower fundamental resonant excitation energy for thinner spacers as shown experimentally (see red-shifting extinction peaks in Fig. 2.15). If conditions are appropriate, it is possible to transition from single mode to multi-mode resonant structures by tuning s: two extinction peaks at 1150 and 1350 cm^{-1} for $s = 3$ nm and also two peaks at 750 and 850 cm^{-1} for $s = 1$ nm. Additionally, s also control the SGP excitation efficiency. Recovering the dipole analogy, at larger distances from the dipole, the fields are weaker and have less high momentum components. Consequently, even for the more confined SGP in thinner spacers and thanks to enhanced coupling through the effective dipole, it is possible to preserve a good S/N ratio.

2.5 Acoustic plasmons in high-quality graphene

CVD graphene is good for a variety of plasmonic applications [159, 160, 161], but it is definitely not the best regarding plasmon lifetime. For such a purpose, high-quality graphene encapsulated in h−BN stacks must be used [34, 163]. With mentioned heterostructures, mobility higher than $30,000\ \mathrm{cm^2V^{-1}s^{-1}}$ have been reported at room temperature and achieved quite regularly. However, plasmons haven't been studied using far-field techniques in these structures yet because the typical flake sizes are not large enough to provide good enough S/N ratio once the stack is etched into nanostructures. Additionally, fabrication of the stacks is highly time-consuming and nanofabrication is detrimental for graphene quality.

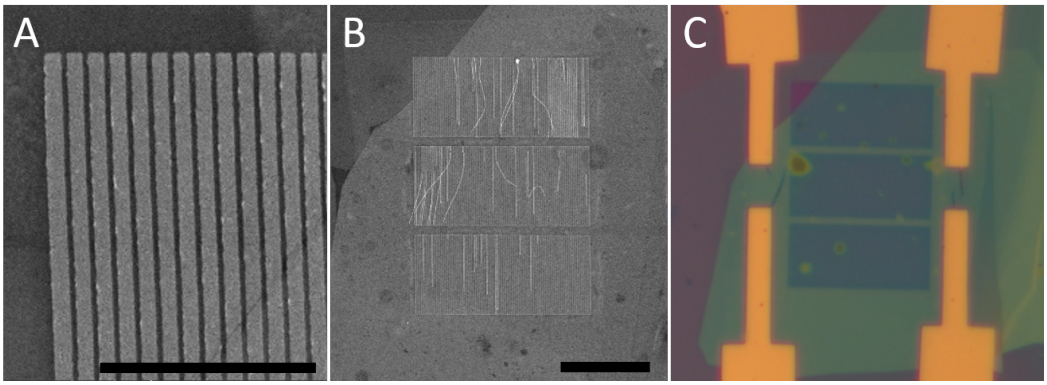

FIGURE 2.16: Micrographs of hybrid heterostructure device with 150 nm periodic structure of 100 nm nominal width metal ribbons. **A** - SEM detail of the nanostructures, scalebar is 1.5 μm. **B** - SEM image of the complete hybrid structure before contacts, scalebar is 10 μm. **C** - Optical image of the structure after contacts.

Application of the SGP methodology/fabrication was found appropriate for successful observation of high-quality plasmon resonances in FF, paving the way towards fine spectroscopy sensing applications.

As a proof of concept, a h−BN/graphene/h−BN stack with top and bottom h−BN thicknesses of 13 and 4.5 nm respectively was contacted and finished with a periodic array of 100 nm nominal width ribbons and 150 nm period arranged on 3 rows. The active device area covered 20 by 30 $\mu\mathrm{m}^2$. Micrographs of the device are shown in Fig. 2.16.

Transmission extinction measurements were performed using a 36x collecting objective in an FTIR microscope, instead of the usual 15x objective. Results are shown in Fig. 2.17 with simulated extinction divided by 2 of 120 nm metal width and 150 nm period superimposed to the experiment extinction. Despite the resulting

features are quite clear it is obvious that noise level reaches $1-2\%$ which is comparable or even higher than extinction signals observed from narrow ribbons in a larger area. This fact highlights the difficulty to observe the resonances before.

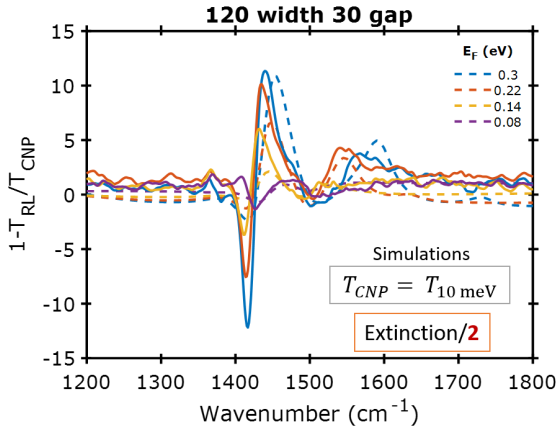

FIGURE 2.17: Different doping extinction curves of a high-quality graphene hybrid heterostructure device referenced to CNP for experiments (solid line) and simulations (dashed line).

Analyzing the results, we observe 2 resonant features in the second Resthralen band of h$-$BN blue-shifting with E_F. The first resonance (around 1450 cm^{-1}), tightly bound in the phonon band, exhibits a Q-factor of 53 which yields a lifetime of 393 fs. Meanwhile, the second resonance at 1590 cm^{-1} provides a Q-factor of 29 and 200 fs lifetime.

The above-mentioned results are promising for future studies and applications.

Chapter 3

Ultimate field confinement to one atom

3.1 Introduction

As it was mentioned in section 2.1, there is a fundamental limitation to one-atom for the out-of-plane direction confinement. If the spacer material is removed in the aforementioned scheme; then both, graphene and metal, are found to be in electrical contact. Unless by some means a vacuum spacer thinner than an atom holds them together but still remain separated (van der Waals force might do it) and somehow electrically disconnected too; which seems unfeasible. Under this perspective, someone may ambition/devise/wish on creating a thinner spacer made out of particles or sub-particles such as neutrons or quarks, but it happens to be unrealistic, unstable, and completely out of the scope of this thesis.

Comparable light-squeeze down to atom-sized dimensions in the out-of-plane direction have been reported before using metal plasmonics [164, 165] with a huge drawback: extremely high losses caused by the field penetration in the metal. The experimental realization of the ultimate vertical confinement by squeezing propagating plasmons through a one-atom spacer with reduced losses is reported and analyzed in this chapter. Such heterostructures should provide a powerful and versatile platform for nanophotonics, enabling new regimes of light-matter interaction.

3.2 Sample fabrication & methods

Fabrication-wise, we find ourselves within the work-space of the previous chapter but with a major difference: the spacing material only comprises a monolayer of insulating h−BN [166, 167]. This configuration requires a slightly different fabrication process and external collaboration (with the Massachusetts Institute of Technology, MIT) to obtain the proper materials.

The fabrication process started with CVD graphene being wet-transferred to the bare $SiO_2/Si/SiO_2$ substrate, and after drying, wet-transferring of CVD h−BN monolayer on top. Later on, lithographic processes shaped graphene and h−BN into six 800 μm by 120 μm (length, width) stripes and patterned the corresponding source (S) and drain (D) metal contacts (see Fig. 3.1). Finally, the rod arrays were made by e-beam lithography, evaporation and lift-off on top (active area) and aside (reference area) of graphene-h−BN stripes covering an area of 99 by 100 μm^2 each. The rod nominal width (by design) ranged from 20 to 500 nm with a constant nominal gap distance between adjacent rods of 50 nm. They were arranged in 10 columns of 9 μm long horizontal rods with 1 μm separation between columns for easier fabrication purposes. In some cases, depending on the dose (which is increased bottom-up, i.e. from S to D, and equal for active and the corresponding reference areas), the measured values differ up to $\pm$17 nm compared to the nominal width ones in successfully fabricated structures.

As in the previous chapter, the devices were measured with an FTIR microscope in transmission mode (illumination from the substrate side). The polarization was set perpendicular to the ribbons' long direction (TM or "p"), i.e. the wires of the holographic polarizer were parallel to the ribbons. The polarizer was indistinctly positioned before the focusing mirror lens or after the collecting mirror lens because they render equal results. The reference spectrum was taken at CNP and the following spectra for several E_F were taken relative to it and in the same position.

3.3 Experimental results

In order to exemplify and illustrate the success, the narrowest rods were studied first because these structures should present single plasmon resonances due to their reduced lateral dimensions (Fig. 3.2). However, due to the use of a polar substrate (SiO_2) and a monolayer spacer (h−BN) with mid-IR active phonons, hybrid SPPPs (surface plasmon phonon polariton) exhibit distinctive marks in the extinction spectra as extra peaks or dips.

The carrier density of graphene is controlled through the gate voltage, and with it, the plasmon resonant frequency (wavenumber) of the structure. It is a characteristic fingerprint of the graphene-plasmonic nature. Hence, within the available voltage range, several positions of the SPPP mode were scanned crossing the upper h−BN phonon reststrahlen band. It could have been possible to analyze the plasmon-phonon coupling strength from Fig. 3.2 and know if the strong coupling regime has been reached, but it is not relevant for this thesis. The relevant information to extract reduces to: a resonance appears as a broad peak (because of short plasmon lifetime) split by the anti-crossing at the phonon frequency (1350 cm^{-1}).

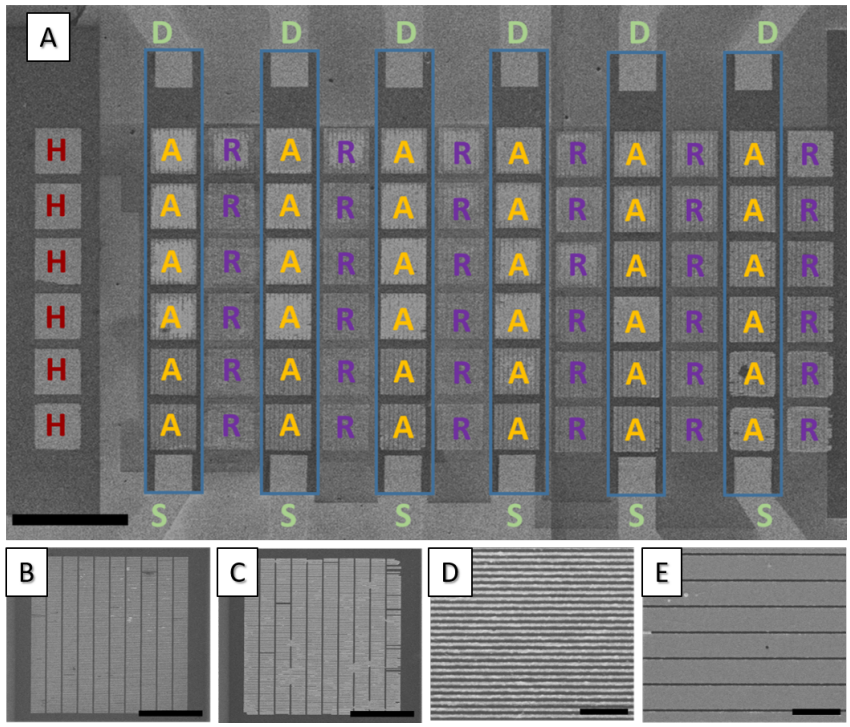

FIGURE 3.1: **A** - Graphene encapsulated in Monolayer h−BN sample composite of 2 SEM micrographs with all the devices showing source-drain S-D Au contacts, graphene dark gray stripes delimited by blue rectangles, reference R and sample A (on top of graphene stripes) metallic rod arrays and homogeneous metal regions (H). Scale bar is 250 μm. Active areas of 100 μm for metal rod periods of 70 nm (**B**) and 550 nm (**C**). Scale bars are 40 μm. (**D**) 70 nm period metallic rod array (scale bar is 500 nm). (**E**) Rod array with period of 550 nm. Scale bar is 1 μm.

After it is ensured the graphene-plasmonic origin of the resonance by the gate tunability (Fig. 3.2), one must examine if the plasmons propagate under the metal and through the one-atom spacer. In order to study it, extinction measurements in transmission at the highest $|E_F|$ for several metal widths are shown in Fig. 3.3A. Following the red-dashed line, one gets the intuition of the peak position evolution with metal width for a constant gap. Having a trend indicates there is a relation between metal width and the plasmonic resonance position. And red-shift of the resonant frequency for increased width confirms that the resonant condition is dominated by the metal width. This is a Fabry-Pérot cavity whose fundamental frequency red-shifts with cavity length. Its higher-order modes evolution can also be seen by following the other two dashed-lines. Other interesting features are the peaks close to the SiO_2 phonon for graphene only and 33 nm width curves, which are related to large wave-vector SPPP; or simply, Drude-like graphene response

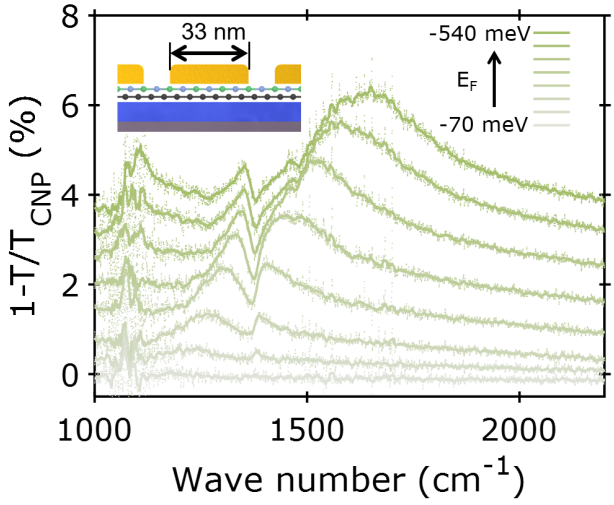

FIGURE 3.2: Monolayer h−BN spacer single resonance structure extinction evolution with E_F. The device dimensions are 33 nm rod width and 70 nm period the rest of the structure is found in the inset. Every curve is shifted 0.25 % from the previous one for visibility reasons.

coupled to the substrate surface phonons.

Willing for an in-depth understanding of the device's response, they were compared with simulations. Surprisingly, we had to use a thicker spacer in order to fit the peak position properly. In the next section 3.4 it is going to be explained why.

It is observed a qualitative match between experiments (Fig. 3.3A) and semi-analytical simulations (Fig. 3.3B) using the method described in subsubsection 1.2.3.4. The overall shape is preserved, yet the extinction values do not match. This discrepancy has two components (excluding the thicker h−BN which will be detailed in 3.4): experimental imperfections and model idealizations. The former includes ribbon edge roundness, a possible tilt of the sample and not normal incidence, to name a few. The later assumes graphene as an interlayer, i. e. zero thickness and the broadening caused by the metal inhomogeneous width along the ribbon is phenomenologically introduced in the model by a shorter electron lifetime of the conductivity. Additionally, the metal is assumed to be perfect, which implies no fields inside (perfect screening). On the other hand, all the surfaces present a certain roughness (including CVD graphene itself), which is generally neglected but affects the optical response and especially the part related to graphene electron mobility (quality).

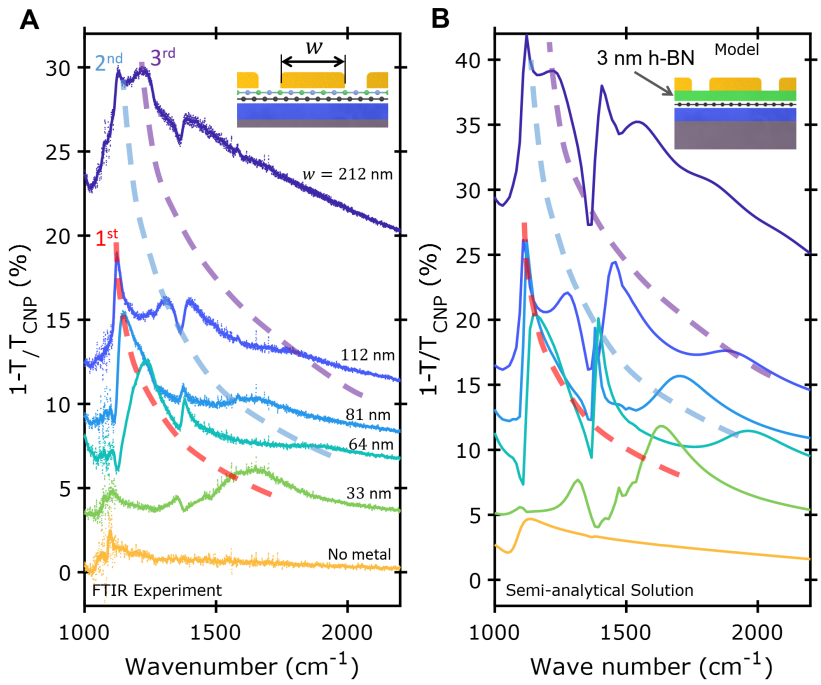

FIGURE 3.3: Monolayer h−BN spacer, metal width extinction dependence. **A** - Experimental extinction spectra for w ranging from 33 to 212 nm, and fixed $g = 38 \pm 5$ nm, and $E_F = 540$ meV. Dashed lines are guides to the eye showing the evolution of each resonance with w. **A** (Inset) - Monolayer device schematic for the experimental data. **B** - Simulated extinction spectra where the nonlocal metal effects are accounted for by modeling a perfectly conducting metal but an effective thicker 3-nm h−BN spacer. **B** (Inset) - Model schematic for the semi-analytical solution. Every curve in both plots is shifted proportionally to the metal width in nm: $shift = w_{\text{nm}} \times 0.1\%$

3.4 Metal nonlocal effects

Nonlocal effects is the terminology used for the momentum dependent optical response of the material. In other words, the metal permittivity becomes a function of excitation energy and momentum, and the local assumption (the material response at a given point only depends on the point properties) doesn't hold anymore and the contribution of neighbors should also be considered to obtain a meaningful response at the evaluated point.

Generally, nonlocal effects appear when the field component has wave-vector (momentum) comparable to a characteristic length/momentum of the material itself. In metals, this length is related to the electron-electron interaction in the electron gas.

Nonlocal effects on metal-insulator-metal (MIM) structures start to be important for insulator thickness of < 5 nm [168], for example. However, the limit where nonlocal effects become dominant depends on the in-plane momentum of the mode, which depends on wavelength, the properties of the metal itself and the surrounding materials, and the system geometry. If by any means, one can reach a similar mode index (wave-vector) than in a MIM of dielectric thickness < 5 nm, nonlocal effects will present a non-negligible contribution to the system response.

3.4.1 Nonlocal hydrodynamic model

In the structures used in this section, the close proximity between the metal and the graphene, and the subsequent very strong confinement of the field in the spacer, nonlocal effects in the metal become very important to accurately describe the physical behavior of the system, as it will be shown henceforth. Although our description of the periodic system (described in subsubsection 1.2.3.4) considers the metal to be perfect, these effects can be accounted for in the case where we consider a continuous system, as discussed below.

In order to take nonlocal effects into account, we consider the hydrodynamic model developed in [168, 169, 170]. Within this model, Faraday's law $\boldsymbol{\nabla} \times \mathbf{E} = \mathrm{i}\omega\mathbf{B}$ remains unchanged, whereas Ampère's law now reads:

$$\boldsymbol{\nabla} \times \mathbf{B} = -\mathrm{i}(\varepsilon_\mathrm{m}\omega/c^2)[\mathbf{E} - \alpha\boldsymbol{\nabla}(\boldsymbol{\nabla}\cdot\mathbf{E})], \tag{3.1}$$

where ε_m is the metal local dielectric permittivity, and α is defined as:

$$\alpha = \frac{\beta^2}{\omega_\mathrm{p}^2/(1+\chi_\mathrm{b}) - \omega^2 - \mathrm{i}\gamma_\mathrm{m}\omega}, \tag{3.2}$$

with ω_p is its plasma frequency, γ_m is its damping frequency, and χ_b being the magnetic susceptibility of the metal and β being a phenomenological nonlocal parameter characteristic of the metal. We will take the most useful definition $\beta = \sqrt{2/3}v_\mathrm{F}$, where v_F is the Fermi velocity of the electrons in the metal. It is clear that the local case is recovered when $\beta = 0$.

Under these conditions, the Maxwell's equations admit, on the one hand, the well-known divergence-free modes (dubbed 'transversal'), obeying the condition $\nabla^2\mathbf{E}^\mathrm{T} = -\varepsilon_\mathrm{m}\omega^2/c^2\mathbf{E}^\mathrm{T}$, with the corresponding magnetic field being determined by Faraday's equation. These are equally recovered when $\beta = 0$, being hence equivalent to the modes considered in the local framework. However, on the other hand, now the Maxwell's equations also admit additional curl-free modes (dubbed 'longitudinal') obeying the condition $\nabla^2\mathbf{E}^\mathrm{L} = (1/\alpha)\mathbf{E}^\mathrm{L}$. It is clear that the magnetic field

corresponding to these modes is null. The total electric field inside the metal is therefore $\mathbf{E} = \mathbf{E}^{\mathrm{T}} + \mathbf{E}^{\mathrm{L}}$, whereas the magnetic field is simply $\mathbf{B} = \mathbf{B}^{\mathrm{T}}$.

3.4.2 Treatment of the continuous structure

In order to get further insight into the influence of the metal on the plasmonic properties of the system, it is useful to consider the case where the metal is continuous, as depicted in Fig. 3.4.

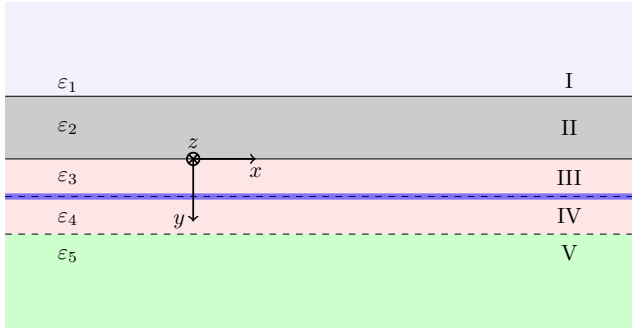

FIGURE 3.4: Scheme of the considered system for the continuous case.

Unlike the previous case, now we will consider a real metal described by Drude's model, taking into account nonlocal effects. Furthermore, we will be looking into the plasmonic properties of the system, the reason why no impinging field will be considered.

Since there is no scattering in the system (it is continuous), the magnetic field $\mathbf{B}_\nu(\mathbf{r},t) = B_\nu(x,y)\mathrm{e}^{-\mathrm{i}\omega t}\hat{\mathbf{z}}$ in each dielectric region (where ν is the layer index from I to V) can be written as:

$$B_\nu(x,y) = \left[C_\nu^+ \mathrm{e}^{\kappa_{\mathrm{T}}^{(\nu)} y} + C_\nu^- \mathrm{e}^{\kappa_{\mathrm{T}}^{(\nu)} y}\right]\mathrm{e}^{\mathrm{i}qx}, \tag{3.3}$$

with $\kappa_{\mathrm{T}}^{(\nu)} = \sqrt{q^2 - \varepsilon_\nu \omega^2/c^2}$. Like before, C_{I}^- and C_{V}^+ must be set to zero in order to guarantee the convergence of the fields in the infinity. The corresponding electric fields are obtained using the expression $\mathbf{E}_\nu(\mathbf{r},t) = (\mathrm{i}c^2/\omega\varepsilon_\nu)\boldsymbol{\nabla} \times \mathbf{B}_\nu(\mathbf{r},t)$.

The absence of periodicity on the system strongly simplifies the approach to the problem, being possible to consider a real metal whose permittivity is described by Drude's model:

$$\varepsilon_{\mathrm{m}}(\omega) = \varepsilon_\infty - \frac{\omega_{\mathrm{p}}^2}{\omega(\omega + \mathrm{i}\gamma_{\mathrm{m}})}, \tag{3.4}$$

and it will also be considered to be nonlocal, and thus its magnetic field $\mathbf{B}_{\mathrm{II}}^{\mathrm{T}}(\mathbf{r},t) = B_{\mathrm{II}}^{\mathrm{T}}\mathrm{e}^{-\mathrm{i}\omega t}\hat{\mathbf{z}}$ is given by:

$$B_{\mathrm{II}}^{\mathrm{T}}(x,y) = \left[C_{\mathrm{II}}^{+}\mathrm{e}^{\kappa_{\mathrm{T}}^{(2)}y} + C_{\mathrm{II}}^{-}\mathrm{e}^{-\kappa_{\mathrm{T}}^{(2)}y}\right]\mathrm{e}^{\mathrm{i}qx}, \tag{3.5}$$

whereas its electric field is composed by longitudinal and transversal modes whose x and y components are given by:

$$\begin{aligned} E_{\mathrm{II}}^{\mathrm{T},x}(x,y) &= \frac{\mathrm{i}\kappa_{\mathrm{T}}^{(2)}}{\omega\varepsilon_0\varepsilon_{\mathrm{m}}}\left[C_{\mathrm{II}}^{+}\mathrm{e}^{\kappa_{\mathrm{T}}^{(2)}y} - C_{\mathrm{II}}^{-}\mathrm{e}^{-\kappa_{\mathrm{T}}^{(2)}y}\right]\mathrm{e}^{\mathrm{i}qx}, \\ E_{\mathrm{II}}^{\mathrm{T},y}(x,y) &= \frac{q}{\omega\varepsilon_0\varepsilon_{\mathrm{m}}}\left[C_{\mathrm{II}}^{+}\mathrm{e}^{\kappa_{\mathrm{T}}^{(2)}y} + C_{\mathrm{II}}^{-}\mathrm{e}^{-\kappa_{\mathrm{T}}^{(2)}y}\right]\mathrm{e}^{\mathrm{i}qx}, \end{aligned} \tag{3.6}$$

$$\begin{aligned} E_{\mathrm{II}}^{\mathrm{L},x}(x,y) &= \left[D_{\mathrm{II}}^{+}\mathrm{e}^{\kappa_{\mathrm{L}}^{(2)}y} + D_{\mathrm{II}}^{-}\mathrm{e}^{-\kappa_{\mathrm{L}}^{(2)}y}\right]\mathrm{e}^{\mathrm{i}qx}, \\ E_{\mathrm{II}}^{\mathrm{L},y}(x,y) &= \frac{\kappa_{\mathrm{L}}^{(2)}}{\mathrm{i}q}\left[D_{\mathrm{II}}^{+}\mathrm{e}^{\kappa_{\mathrm{L}}^{(2)}y} - D_{\mathrm{II}}^{-}\mathrm{e}^{-\kappa_{\mathrm{L}}^{(2)}y}\right]\mathrm{e}^{\mathrm{i}qx}, \end{aligned} \tag{3.7}$$

in accordance with the differential equations stated in the previous subsection 3.4.1 for each case. In the previous expressions, $\kappa_{\mathrm{T}}^{(2)}$ is defined as before and $\kappa_{\mathrm{L}}^{(2)} = \sqrt{q^2 + \frac{1}{\beta^2}\left(\frac{\omega_{\mathrm{P}}^2}{1+\chi_{\mathrm{b}}} - \omega^2 - \mathrm{i}\gamma_{\mathrm{m}}\omega\right)}$.

In order to determine the unknown 10 coefficients describing the fields in each region, we need to employ the interlayer boundary conditions in the problem, in a similar manner to the noncontinuous problem. However, the addition of the longitudinal modes to the description of the electric field inside the metal adds two new undetermined coefficients to the problem, $D_{\mathrm{II}}^{\pm}$, what imposes the consideration of another boundary condition to the problem. We will consider this additional boundary condition to be the vanishing of the normal component of the polarization $\mathbf{P} = (\mathrm{i}/\omega\mu_0)\boldsymbol{\nabla}\times\mathbf{B} - \varepsilon_0(1+\chi_{\mathrm{b}})\mathbf{E}$ in each of the metal/dielectric interfaces; this condition means that currents flowing from the metal to the dielectric are not allowed.

With these two new conditions, the number of boundary conditions matches the number of unknown coefficients, as they should. However, note that, since there is no impinging field, this system is undetermined; 9 out of the 10 conditions must be used to determine 9 out of the 10 coefficients; the other condition must be solved for the dispersion relation. The remaining undetermined coefficient needs to be regarded as a free parameter of the problem, acting as the scaling of the plasmonic fields.

Proceeding as described before, one can study a realistic system with a spacer filled

with hBN, and regions IV and V filled respectively with SiO_2 and Si. Considering that the experimental setup has 2 nm of metallic Titanium underneath the Gold ribbons, we assume in the simulations the bulk metal to be Titanium, described by the parameters: $\omega_P = 2.80$ eV, [171] $\gamma_m = 82.0$ meV [171], $\chi_b = 1.2$, [172] and $v_F/c = 0.00597$ [173]. We further consider the spacer width to be $s = 0.7$ nm. Using this method, we have calculated the dispersion relation for this system both in the local and nonlocal frameworks, as shown in Fig. 3.5A. Comparing both curves, one sees that the influence of the nonlocality in this problem is very large.

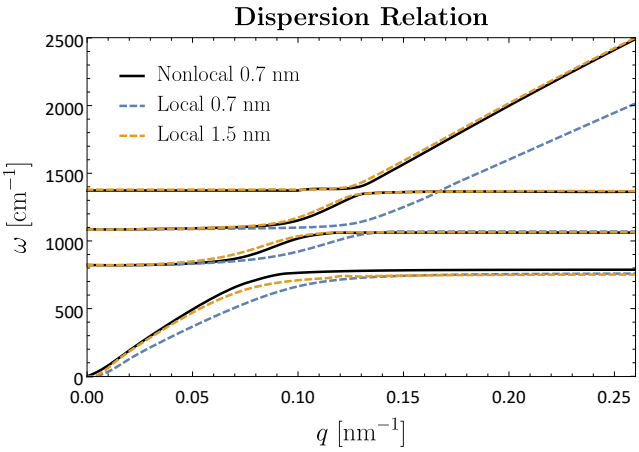

FIGURE 3.5: Dispersion relation for a plasmonic mode calculated nonlocally (solid black) for the real spacer 0.7 nm and locally (dashed) for 0.7 nm (blue) and the best fitting effective spacer 1.5 nm (orange).

On the other hand, it is also shown that these effects can be very well mimicked by considering an effective spacer thickness in the local regime; for this case, a local system with $s = 1.5$ nm effectively mimics very well the nonlocal system with $s = 0.7$ nm. However, one should note that the optimal effective spacer thickness which better compensates the nonlocal effects depends highly on the geometric properties of the system and the physical properties of the media that it is composed of, so its theoretical calculation is very difficult, and it must be regarded as a fitting parameter of the model. For this reason, this analysis does not intend to provide a theoretical effective spacer value that holds for the periodic case, but rather to show that this is a valid technique to account for nonlocality within a local approach as demonstrated for metal plasmons before [174].

To conclude, Fig. 3.6 shows the magnetic (a) and electric (b) field profile of a simplified system (not including Si-SiO_2 substrate) in the air (light-blue background), h−BN (green background), and metal (grey background) regions, calculated both

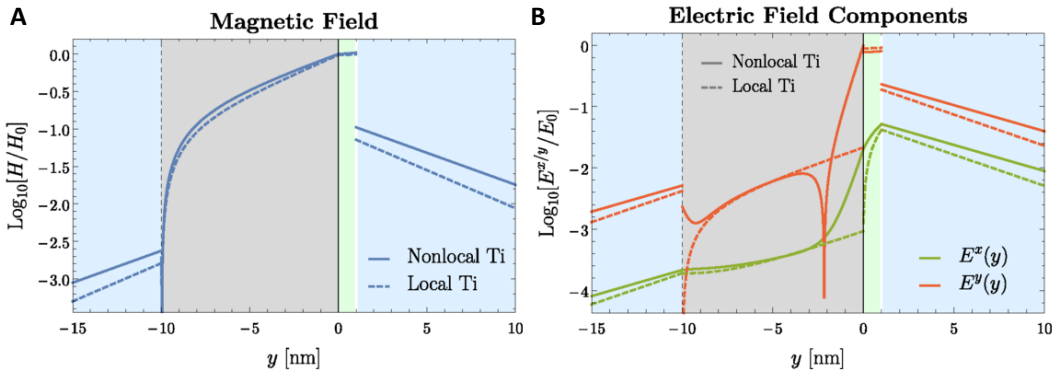

FIGURE 3.6: Nonlocal metal fields from [175] I'm second author.

locally and nonlocally, for modes with the same frequency. The fields were arbitrarily normalized to their value in the outer surface of the metal. There are very similar magnetic field trends for both local and nonlocal calculations since there is no transverse contribution (the only one affecting the magnetic field) introduced by the hydrodynamic model. In the electric field plot, one sees that, locally, the y-component of the electric field penetration is negligible (the field inside the metal is at least two orders of magnitude lower than its value outside), whereas nonlocally there is a much higher penetration which decays slowly inside the metal, with a penetration depth of around 2 nm (a value which is comparable to the height of the metal 10 nm). The field along x is continuous in both cases (as expected), but when nonlocality is included, its value is larger inside the metal because the longitudinal component along x is allowed. This behavior agrees with the previously discussed fact that nonlocality contributes to higher penetration of the field inside the metal, rather than its concentration on the surface as it happens for a perfect metal.

At around $y = -2.5$ nm there is a sudden dip of the electric field, which does not occur locally. This corresponds to the point where the y-component of the electric field has a node because its longitudinal and transverse components cancel each other ($E_{\mathrm{L}}^{\mathrm{y}} + E_{\mathrm{T}}^{\mathrm{y}} = 0$). To the right of this point, the longitudinal component is dominant, thus amounting to a greater nonlocal effect; to the left of this point, on the other hand, the transversal component is dominant, and the behavior of the field resembles very well the local one.

3.4.3 Loss function for a continuous heterostructure

The calculation of the loss function for the system presented in the previous section losses on the calculation of the optical properties of that system (namely its

reflectance) upon illumination. Let us assume that the impinging field propagates upwards from region V, has some magnetic field amplitude B_0, frequency ω and inclination angle θ with respect to the y-axis. Itt therefore carries momentum $\mathbf{k} = k_x\hat{\mathbf{x}} - k_y\hat{\mathbf{y}}$, with $k_x = k\sin(\theta)$, $k_y = k\cos(\theta)$ and $k = \sqrt{\varepsilon_5}\omega/c$. The method to calculate these properties follows basically the same steps as before except for the following differences:

- in the field description of region V, an additional term must be added corresponding to the impinging illumination. This term must have the form $B_0 e^{ik_x x} e^{-ik_y y}$ for the magnetic field, and an analogous one for the electric field;
- the in-plane momentum of the remaining fields must now be k_x instead of q;
- in the fields description, we must perform the change $\kappa_{T/L}^{(\nu)} \rightarrow ik_{T/L}^{(\nu)}$, with $k_T^{(\nu)} = \sqrt{\varepsilon_\nu\omega^2/c^2 - q^2}$ and $k_L^{(2)} = \sqrt{-\left[\omega_p^2/(1+\chi_b) - \omega^2 - i\gamma_m\omega\right]/\beta^2 - q^2}$, in order to explicitly consider propagating modes;
- its useful to identify coefficient $C_I^- \equiv B_0\tau$ and $C_V^+ \equiv B_0 r$ so that τ and r have the physical meaning of the transmittance and reflectance coefficients, respectively.

After performing these changes, one must once again use the interlayer boundary conditions to find all the coefficients. Unlike the previous case, the addition of the impinging field provides a source to the system, meaning that the system of equations composed by all the boundary conditions is determined, and can be straightforwardly solved to find all the coefficients. After they are determined, the loss function is defined as:

$$L = -\Im\{r\}. \tag{3.8}$$

An example of the use of the loss function is shown in Fig. 3.7 for the nonlocal system of Fig. 3.5. Observing this magnitude provides a visual understanding of the intrinsic broadening of the mode. Dispersion relations for different spacer thicknesses for local and perfect metal are also superimposed. It should be noted there is almost no difference for local or perfect metal models in the 3 nm spacer case. This fact supports the use of the perfect metal for the semi-analytical calculations within the analogous model of the metal nonlocality using a thicker dielectric spacer.

3.5 Mode losses

When calculating the dispersion relation of the plasmonic modes, in the presence of dissipation in the system, either q or ω need to be regarded as a complex number, in

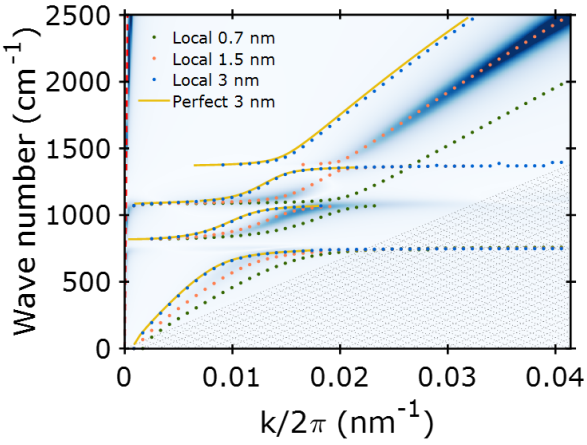

FIGURE 3.7: Plasmon dispersion relation for a (continuous) SiO_2/graphene/h$-$BN/metal/air heterostructure. Dotted curves correspond to local metal response [with nonzero loss; refAppendix] and are plotted for h$-$BN thickness of 0.7 nm (green), 1.5 nm (orange), and 3 nm (blue). The solid yellow curve corresponds to h-BN thickness of 3 nm (yellow) and modeling the metal as perfectly conducting. The blue color gradient represents the loss function of the heterostructure for 0.7 nm-thick h$-$BN with nonlocal metal (titanium) and nonlocal graphene response. This illustrates that accounting for nonlocality comes down to adding an extra spacer thickness of $\sim$ 2 nm to a model that considers only the local or perfect metal response.

order to successfully comply with the systems boundary conditions. In the present case, we have chosen to regard q as real and ω as complex, because this approach was advantageous when numerically solving the problem.

For this reason, although in the previous analysis only the real part of ω has been considered, in fact, we retrieved frequencies of the form $\omega = \omega' - i\omega''$, where ω' and ω'' are both real and positive numbers. For this reason, noting that the fields evolve with $e^{-i\omega t}$, this contribution can be written as $e^{-i\omega' t}e^{-\omega'' t}$, where the latter term clearly corresponds to a damping of the fields. For that reason, ω'' is intrinsically connected to the plasmonic losses of the system (the larger the ω'', the larger the losses), providing useful insight to characterize them.

In Fig. 3.8 is represented the imaginary part of the frequency for each of the dispersion curves represented in Fig. 3.7 plotted against the corresponding wavenumber. There is a strong frequency dependence of the losses due to the dispersive nature of the dielectric materials employed, namely the hBN and the SiO_2. Especially,

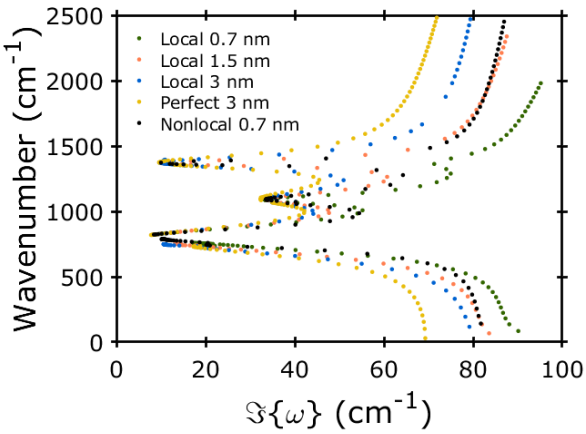

FIGURE 3.8: Imaginary part of ω of the dispersion plots in Fig. 3.7 (including the dispersion associated with the nonlocal metal represented by the loss function there), which is associated with losses.

phonons with a quite large τ can be noticed around 800, 1100 and 1400 cm^{-1} becoming dominant at those regions. On the other hand, it is interesting to note that, for the same spacer, the losses under the local regime are generally higher than those under the nonlocal one.

3.6 Confinement

The lateral confinement can be represented as the mode index (λ_0/λ_p) that indicates how many times the plasmon wavelength is smaller than the free space one. Its evolution with the spacer thickness is plotted in Fig. 3.9,a for two different dielectric materials (h$-$BN and Al_2O_3) at 1250 cm^{-1} excitation. This theoretical study was repeated under three different regimes: local graphene with local metal, nonlocal graphene with local metal, and nonlocal graphene with nonlocal metal. If both materials are considered to present a local response, it becomes clear that the lateral mode index diverges when diminishing the distance between graphene and metal. However, this image is not realistic and as soon as one of the materials is input with a more realistic model, the mode index presents an upper bound.
It is known that the graphene plasmons mode index cannot reach 300 (the c/v_F ratio) which is equivalent to excite interband transitions in the Landau damping region (momentum assisted). This effect is included in the nonlocal graphene conductivity and it can be observed as an asymptotic approach of the mode index towards 300 in the dashed-dotted line of Fig. 3.9A. Finally, metal nonlocality adds an extra constraint to the mode index and lowers its value again due to its reduced

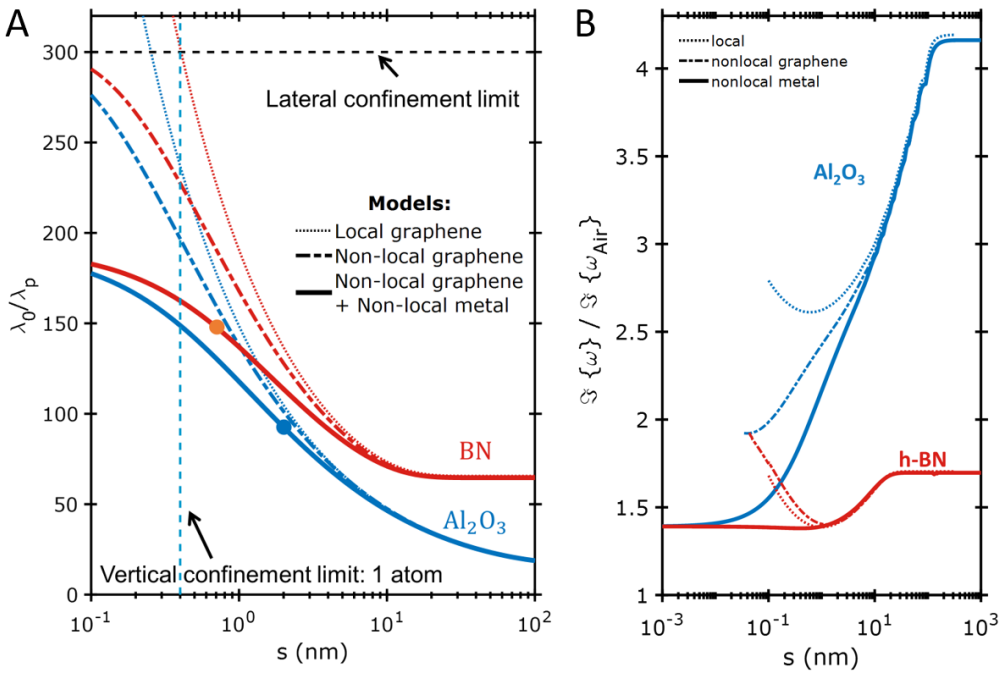

FIGURE 3.9: **A** - Calculated mode index (λ_0/λ_p) as a function of metal-graphene spacer s for the two materials used in the experiments ($\lambda_0 = 8$ μm and $E_F = 0.54$ eV). The vertical dashed line refers to the fundamental limit: one-atom-thick spacer. Colored circles correspond to the two sets of devices discussed in the main text of [151]. The dotted lines represent the model where the metal was considered as a perfect conductor in combination with the local graphene conductivity model. The dash-dotted lines represent the nonlocal graphene conductivity model (obtained from the random-phase approximation), but the metal was still considered a perfect conductor. The solid lines represent the model where the nonlocal optical response for both metal and graphene are considered. **B** - System losses normalized by losses of graphene in air. The same line and color coding as in A are used.

screening capability. The metal considered for the calculations was Ti, whose nonlocality is large compared to other metals, for instance, Au.

In Fig. 3.9B, it has been traced the evolution of the system losses normalized to the graphene in air losses (represented by the division of their imaginary parts of the frequency) as a function of the spacer thickness for the same conditions as in Fig. 3.9A. Generally speaking, for all regimes, the losses are substantially higher for

larger spacers, which can be attributed to the fact that, in this case, the field propagates in h−BN/Al_2O_3 for a larger distance, thus increasing the total absorption in the dielectric. On the opposite regime, when the spacer is very small (and the confinement increases), the losses tend to increase for local metal and to stabilize for nonlocal one. The reason for this divergence is that, locally, the field accumulates mostly outside the metal, meaning a larger field on the surface of the graphene, amounting for higher losses; nonlocally, on the other hand, when the confinement increases, a larger amount of energy penetrates into the metal, and the field on the surface of the graphene does not increase as much.

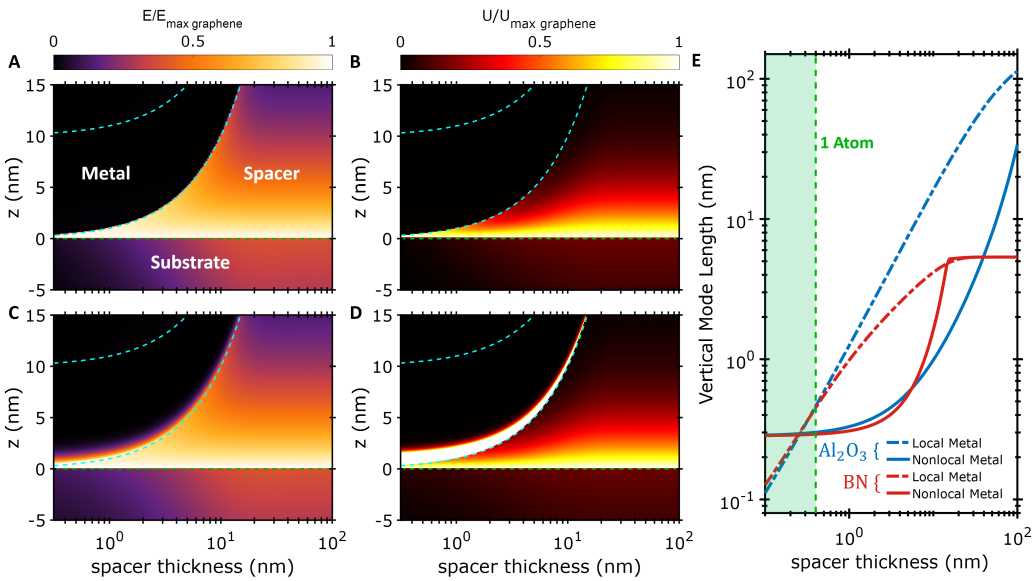

FIGURE 3.10: Electric field magnitude distribution of the plasmons associated to a continuous heterostructure of air/Ti/h−BN/graphene/SiO_2 as a function of h−BN thickness for local metal permittivity model (**A**) and nonlocal metal permittivity model (**C**). The top and bottom metal limits are depicted by blue dashed lines, and graphene is located at z = 0. Normalization by the maximum electric field strictly above graphene shows the confinement and screening effects. (**B** and **D**) Same as (A) and (C), respectively, but for energy density. **E** - Vertical field confinement for both types of dielectrics as a function of the spacer thickness for local (dash-dotted lines) and nonlocal (solid lines) metal permittivity.

Accounting for the confinement in the vertical direction is not as straight-forward as in the lateral confinement case. One must use the following definition:

$$L_z = \frac{\int u_E(z)dz}{\max u_E(z)}, \tag{3.9}$$

where $u_E(z)$ is the z-dependent energy density distribution that has to be integrated for the whole space and normalized by its maximum to obtain the vertical mode length L_z. Consequently, the vertical field distribution needs to be obtained. It can be calculated using the formalism of subsection 3.4.2 for the local and nonlocal approaches and their spacer thickness dependence are plotted in Fig. 3.10A and C, respectively. The differences are minor except for the small penetration of the electric field in the nonlocal metal permittivity case. The electric field confined between graphene and the metal is still shown. However, following eq.3.9 one must obtain the energy density that reads:

$$u_E = \frac{1}{2}\epsilon|E|^2, \tag{3.10}$$

for non-dispersive media and

$$u_E = \frac{1}{2}\epsilon_0|E|^2\left[\frac{\partial\omega\epsilon_r'(\omega)}{\partial\omega}\right], \tag{3.11}$$

for dispersive media [176]. The calculated energy density is obtained using the complete expression eq. 3.11 in Fig. 3.10,B and D, for local and nonlocal metal permittivity models, respectively. It is observed that its value heavily increases if there is some field penetration in the metal due to its large permittivity (assuming eq. 3.10 for an easier but not so accurate explanation).

Finally, the vertical mode length is plotted in Fig. 3.10,E, again for both approaches using eq. 3.9. One can clearly see how the mode length is determined exclusively by the spacer thickness in the local case below a certain thickness. On the other hand, if the nonlocality of the metal is turned on, the vertical mode length is dominated by the field penetrating the metal which decreases the mode length value compared to the local case due to its large energy density (using the simple formula eq.3.10 and considering that metal's permittivity is huge but negative). We can conclude that we have reached atomic-scale vertical field confinement in the spacer, although the energy confinement was in the metal.

Chapter 4

Nonlinear optics with graphene

The reader will find in this chapter a brief introduction to nonlinear optics. It is followed by a general description of nonlinear optics in the case of the one-atom-thick material graphene. Once the basis is settled, it is proceeded to study the third-harmonic generation (THG) from graphene in the MIR experimentally. Finally, the effects on the graphene's THG due to the close proximity of a metallic ribbon periodic array are presented. In particular, the experimental field enhancement provided by the metal structures and the graphene plasmons modulation of such signal.

4.1 Nonlinear optics

Every material has a nonlinear response to external excitation, whether we consider mechanics, electronics or optics. The existence of nonlinear response in most fields was known for a long time except in optics where there was a lag of appropriate light sources to reach this regime, until the invention of the laser [177, 178] and the realization of the first optical harmonic generation experiment [179]. Despite the knowledge of materials nonlinear response, for ease of use, their response is generally linearized in the regime of small amplitude excitation. Some examples are the small displacement in a pendulum, the elastic response/deformation of a spring/material below the plastic limit under elongation/stress, the small amplitude response of a biased diode and, ray, wave and, diffraction optics.

4.1.1 Introduction

Generally, the optical response of a homogeneous material is characterized by the polarization [180]:

$$\mathbf{P} = \varepsilon_0 \left[\chi^{(1)}\mathbf{E} + \chi^{(2)}\mathbf{E}^2 + \chi^{(3)}\mathbf{E}^3 + \ldots \right] = \mathbf{P}^{(1)} + \mathbf{P}^{(2)} + \mathbf{P}^{(3)} + \ldots, \qquad (4.1)$$

where **P** is the total polarization vector, $\chi^{(i)}$ are the linear susceptibility for i $= 1$ and the corresponding order nonlinear susceptibility for i > 1, **E** is the excitation electric field and, $\mathbf{P}^{(i)}$ the linear and nonlinear polarization for i $= 1$ and i > 1, respectively.

All materials have $\chi^{(3)}$ and its value is material dependent. In general, the nonlinear susceptibility in the same way as the linear susceptibility can be presented as a tensor due to the anisotropic nature of the material. On the other hand, due to symmetry reasons, $\chi^{(2)}$ vanishes for centrosymmetric materials [180]. However, if the material response is nonlocal, i.e. it depends on the momentum for the given excitation energy, it can give rise to second-order nonlinear effects as experimentally proven in anisotropic crystals [181, 182] and theoretically predicted for graphene [129, 130, 121].

4.1.2 Nonlinear optical response of graphene

Considering that graphene is a 2D material, its permittivity/susceptibility is not well defined (see 1.2.1) and leaves some freedom for ambiguity due to thickness uncertainty; especially when using CVD graphene. Despite all this, nonlinear susceptibility has been calculated in this thesis assuming a graphene thickness of $d_g =$ 0.33 nm for both theory and experiments.

Experiment-wise, using the standard procedures to obtain the electric field magnitude in the material and considering the above-mentioned graphene thickness, it is straightforward to obtain the nonlinear susceptibility from input and output powers. However, theory-wise, one must use the generated nonlinear electric currents in graphene taking advantage of the deep knowledge about its optical conductivity and the ability to obtain the electric field distribution through simulations. As a consequence one can write an analogous expression to equation 4.1 but for the current density:

$$\mathbf{j} = \sigma^{(1)}\mathbf{E} + \sigma^{(2)}\mathbf{E}^2 + \sigma^{(3)}\mathbf{E}^3 + \ldots = \mathbf{j}^{(1)} + \mathbf{j}^{(2)} + \mathbf{j}^{(3)} + \ldots, \tag{4.2}$$

which exemplifies the idea of the different order nonlinear currents and their relation with the electric field and nonlinear optical conductivity. For each specific nonlinear process, one must consider different expressions for the involved fields, the nonlinear conductivity and/or how they are related.

Next, it is going to be explained how to obtain the corresponding nonlinear susceptibility for 2 specific cases: nonlocal second harmonic generation (n-SHG) and THG.

4.1.3 Nonlocal second order response

The nonlinear current associated with n-SHG is given by [121]:

$$\mathbf{j}_{NL}^{22} = \sigma_{\omega}^{22,A}\mathbf{E}^{11}(\nabla_{\mathbf{R}} \cdot \mathbf{E}^{11}) + \sigma_{\omega}^{22,B}(\mathbf{E}^{11} \cdot \nabla_{\mathbf{R}})\mathbf{E}^{11} + \sigma_{\omega}^{22,C}\nabla_{\mathbf{R}}(\mathbf{E}^{11} \cdot \mathbf{E}^{11}),$$

where $\sigma_{\omega}^{22,A}$, $\sigma_{\omega}^{22,B}$, and $\sigma_{\omega}^{22,C}$ are nonlocal nonlinear conductivities whose expressions can be found in A.1. The nonlinear second order current is depending exclusively on field gradients. It is worth noting that the only possible currents are in-plane currents, thus $\nabla_{\mathbf{R}}$ becomes ∂x (also assuming homogeneity in y direction). Hence, if the field distribution is homogeneous or symmetric in x (e.g. considering a periodic structure) along the integration length (L), the overall contribution given by the nonlinear second order polarizability:

$$\alpha^{22} = \frac{i\int_L j_{NLx}^{22} dx}{2\omega}, \tag{4.3}$$

which yields the second order susceptibility:

$$\chi^{(2)} = \left|\frac{\alpha^{22}}{d_g L}\right|, \tag{4.4}$$

will vanish.

A strategy to obtain non-zero $\chi^{(2)}$ is to break the symmetry with non-normal incidence and take advantage of graphene's nonlocal response. Using graphene nanotriangle arrays was proposed theoretically in [130], where the combination of non-symmetric plasmon field at excitation and the plasmonic resonance at the second harmonic frequency foster the process. This fact reminds us that not only the incident field must be considered but also the out-coupling efficiency of the generated harmonic at each position.

4.1.4 Third order response

The nonlinear current associated with third harmonic generation is given by [121]:

$$\mathbf{j}_{NL}^{33} = \sigma_{\omega}^{33}\mathbf{E}^{11}(\mathbf{E}^{11} \cdot \mathbf{E}^{11}).$$

However, one must consider the enhancement at the third harmonic (which is unitless), hence, the polarizability reads:

$$\alpha^{33} = \frac{i\sigma_{\omega}^{33}\int_L E_x^3(\omega)E_x(3\omega)dx}{3\omega} \tag{4.5}$$

which yields the third order susceptibility:

$$\chi^{(3)} = \left| \frac{\alpha^{33}}{d_g L} \right| \quad . \tag{4.6}$$

It will only vanish if σ_ω^{33} (simply $\sigma^{(3)}$ now on because only THG is treated/ discussed/ dealt with in this work) is exactly 0 or if the integration of real and imaginary parts of the combination of the fields cancel out simultaneously.

4.1.4.1 Description of $\sigma^{(3)}$ response

Comprehending the trends of the fundamental property that drives graphene's third-order nonlinearity, $\sigma^{(3)}$, becomes essential given that it is one of the 2 most important components that contribute to the nonlinear susceptibility. We will first illustrate it for T = 0 K because there are analytical expressions provided in [128], used in [114, 115, 121] and explicitly reproduced in this thesis (eq.A.5). Whereupon, using Maldague's identity (eq.1.37 [142]), temperature dependence is introduced and further analyzed. This identity is assumed to be applicable even for the electron's temperature case. Given that the material's response is driven by the electrons, in the event of ultrafast pulsed excitation ($\delta t < 1$ ps), they stay in an intermediate thermalized state for about 1 ps after the intermediately hot electrons relax back to equilibrium with the lattice within the scattering relaxation time τ has passed. The abovementioned 1 ps is the electron-phonon interaction typical timescale or "cooling time" [183, 184, 185].

The second main contribution (the integral component) will be further studied in the next section; specifically in the second half. In the first half of the next section, only plane waves with no in-plane field variation are used which leads to trivial results of the integral component.

The first dependence to analyze is with the wavelength or excitation energy/frequency. Immediately, in Fig. 4.1 a huge frequency dependence of $|\sigma^{(3)}|$ can be observed. This is the response of a typical and easily achievable graphene doping level (E_F =200 meV) for several graphene quality (τ) at absolute zero temperature. The trend is clear: $|\sigma^{(3)}|$ monotonically decreases with frequency, with three superimposed sharp features that smear out for lower values of electron relaxation/scattering/life-time. These features correspond to logarithmic type resonances [115] when the excitation energy corresponds exactly with the interband transition energy ($2E_F$) for 3, 2 and, 1 photon in the direction of increasing frequency, respectively. A complete 2π phase change is observed between the 3 and the 1 photon peaks. For large enough excitation energy, the phase tends towards 0, either from the positive (high τ) or negative (low τ) values.

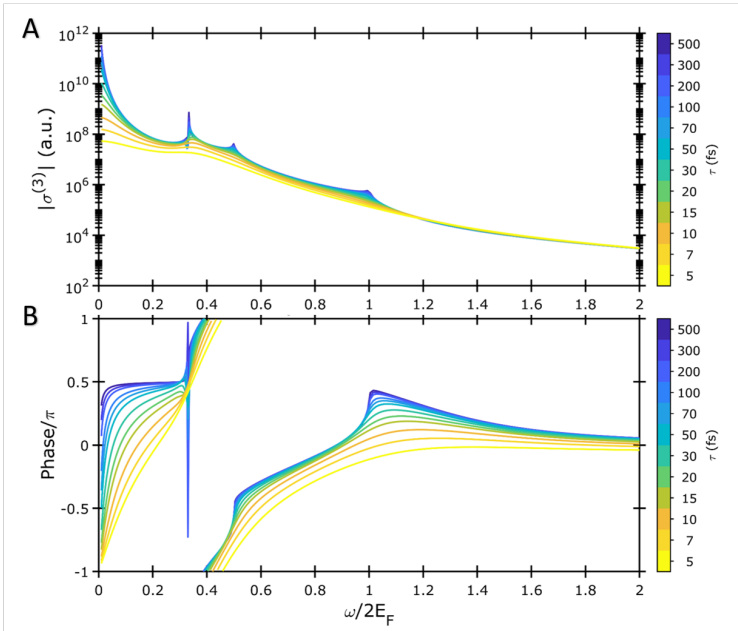

FIGURE 4.1: $|\sigma^{(3)}|$ ω dependence for $E_F = 200$ meV graphene at 0 K for various τ **A** and their corresponding phase **B**.

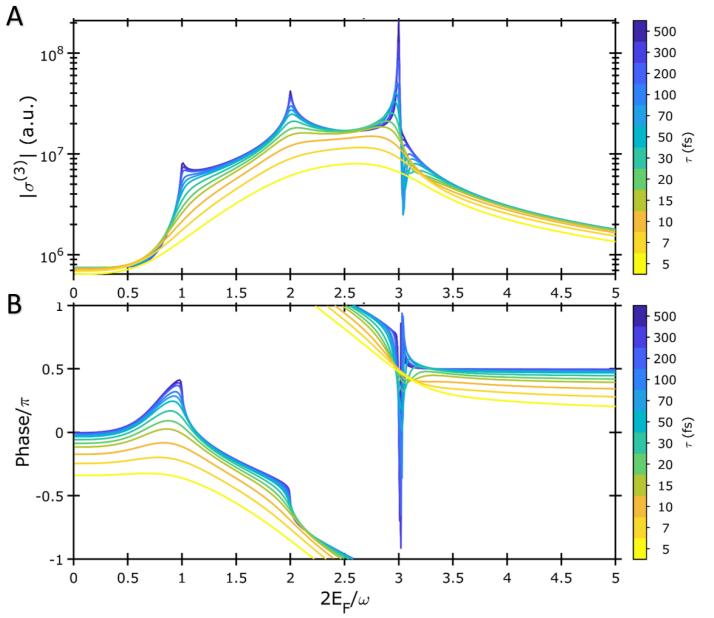

FIGURE 4.2: $|\sigma^{(3)}|$ E_F dependence for $\omega = 200$ meV excitation energy at 0 K for various graphene τ **A** and their corresponding phase **B**.

It should be noted that, according to eq.4.5, the response provided by the conductivity is going to be affected by a factor inversely proportional to the excitation frequency. Such mentioned factor in the polarizability is accentuating the response difference in the frequency dependence of the conductivity. In other words, the nonlinear polarizability $|\alpha^{(3)}|$ and susceptibility $|\chi^{(3)}|$ present a faster decrease for increasing excitation energy than the nonlinear conductivity $|\sigma^{(3)}|$.

If it is studied the E_F dependence for a given ω, one obtains Fig. 4.2. The resulting picture is almost a mirror image of Fig. 4.1 (the excitation energy dependence for a given E_F) scaled on the x-axis. The main difference is the diminishing trend observed in Fig. 4.2 for $E_F >$ 3-photon transition resonance, which translates into an increasing trend for $\omega <$ 3-photon transition resonance in Fig. 4.1. In the first case, increasing E_F corresponds to an augmented number of photons needed for an interband transition, but no extra resonances are allowed for THG. The phase also presents similar but mirrored features.

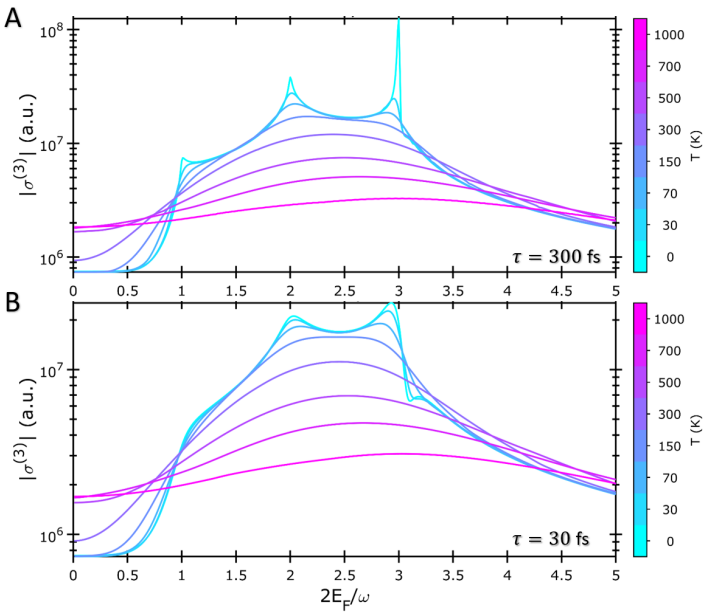

FIGURE 4.3: $\sigma^{(3)}$ E_F dependence for $\omega = 200$ meV and $\tau = 300$ fs (**A**) and $\tau = 30$ fs (**B**) for various T values.

Even though we have access to analytical expressions of $\sigma^{(3)}$ at 0 K, it is a temperature impossible to reach by definition, although it is possible to approach it in cryostats. Additionally, graphene light absorption can cause the electron temperature to rise to the 1000 K order of magnitude relatively easy. It is, therefore,

unnecessary to cool the samples down and it is possible to set the laboratory to a working temperature of 300 K (RT, comfortable for humans). In that regard, Fig. 4.3 provides a guide of what to expect from exfoliated (top) or CVD (bottom) graphene from cryogenic to photoexcited temperatures. As can be seen, the effect of temperature is to smear out all the features. The smearing can be so strong that it can induce a shift on $|\sigma^{(3)}|$ maximum position. Conversely, the value will be lower for higher temperatures except for $2E_F <$ 1-photon and $2E_F >$ 3-photon transitions doping.

4.1.4.2 Influence of light absorption in $\chi^{(3)}$

As described in 1.2, light absorption in graphene is E_F dependent. Consequently, the electron temperature T_e is also E_F dependent. In turn, the chemical potential is connected to both values via the doping charge preserving implicit relation between E_F, T_e, and μ [186]:

$$\left(\frac{E_F}{k_B T_e}\right)^2 = 2\int_0^\infty dx x\Big[\left(e^{x-\mu/k_B T_e}+1\right)^{-1} - \left(e^{x+\mu/k_B T_e}+1\right)^{-1}\Big], \tag{4.7}$$

along with the graphene heat capacity

$$F = \beta\frac{(k_B T)^3}{(\hbar v_F)^3}, \tag{4.8}$$

where F is the energy of the pulse absorbed (i.e., $F = \eta F_0$ where η is the absorbed fraction of power as obtained from the linear RCWA simulations and F_0 is the laser fluence) and

$$\beta = \frac{2}{\pi}\left\{\int_0^\infty dx x^2\Big[\left(e^{x+\mu/k_B T_e}+1\right)^{-1} + \left(e^{x-\mu/k_B T_e}+1\right)^{-1}\Big] - \frac{1}{3}\left(\frac{E_F}{k_B T_e}\right)^3\right\}, \tag{4.9}$$

to obtain the μ and T_e satisfying the above relations simultaneously. These values are then inserted into the graphene nonlinear conductivity with Maldague's thermal smearing [142] (eq.1.37).

An approximated solution for $\Delta T \gg T_0$ could also be used as in [35, 187, 188] with similar results.

4.2 THG measurements

The measurement strategy is straight-forward: illuminate the sample at ω and observe the output at 3ω. However, bringing such a concept into a real experimental setup is not as simple as it seems. Next, we will detail how.

4.2.1 Measurement setup

The measuring scheme is detailed in Fig. 4.4. The first requirement was a suitable tunable laser source that operates in the mid-IR wavelength range with enough power to drive the material's nonlinear response. The source of choice is an OPO (Optical Parametric Oscillator) pumped by a Ti-Sapphire laser, and coupled to a DFG (Difference Frequency Generator) module. The DFG provides mid-IR linearly-polarized $\sim$ 200 fs laser pulses at 80 MHz repetition rate by mixing signal and idler OPO outputs.

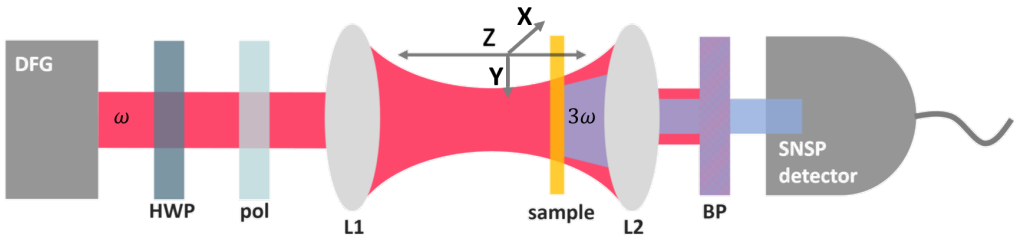

FIGURE 4.4: THG measurement scheme.

The second issue to tackle is in the detection side: high sensitivity and filtering are needed to ensure the collection of the right signal. It was decided to use a band-pass filter before a fiber-coupled SNSP (Superconducting Nanowire Single-Photon) detector [189]. The band-pass filter spectral response measured from the THG signal is shown in Fig. 4.5. The SNSP detector is built on a cavity resonant for 1550 nm but still sensitive close to the band edge of 2000 nm.

The third and last challenge is to maximize the nonlinear signal and ensure it comes from graphene. Using two converging lenses focused at the same point, L1 for the excitation and L2 for the extraction provides the highest signal possible. Additionally, the sample was mounted in a motorized XYZ-stage; and Z-scans were performed along the optical axis (Fig. 4.6). Since third-order nonlinear signals scale with the cube of the incident power, it is expected to obtain a huge contrast when in focus (high power density) compared to out of focus (low power density). In Fig. 4.6 a large peak at Z = 0.28 mm is observed, corresponding to the sample surface with graphene and graphene + gold nanoribbons. Sample details hereunder.

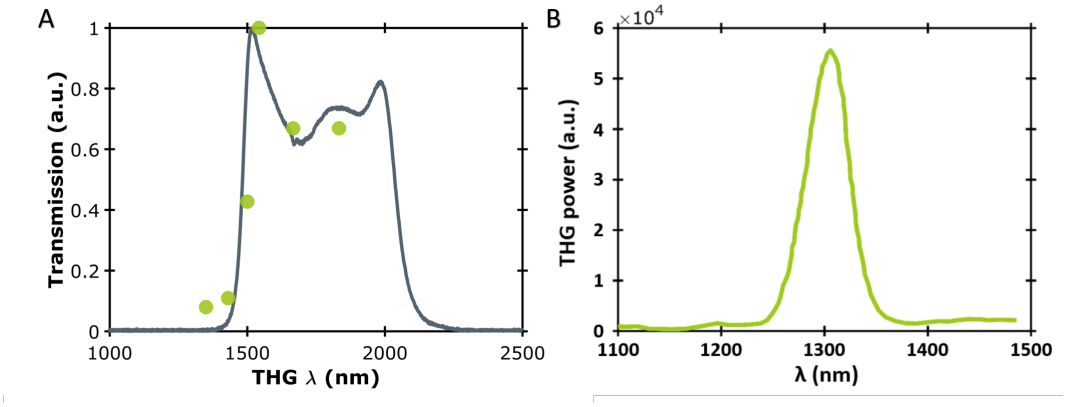

FIGURE 4.5: **A** - Band-pass filter measured using THG with the SNSP detector. The filter is centered at 1750 nm with 500 nm bandwidth. **B** - Spectrum of the THG of 3.9 μm pump.

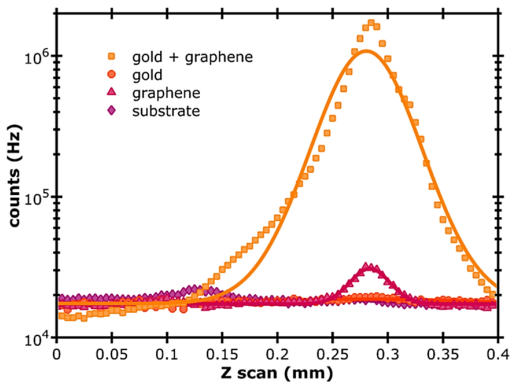

FIGURE 4.6: THG Z-scan THG counts on different exemplary positions of the sample (see Fig. 4.7).

4.2.2 THG from different structures

The samples are the same type as the ones used in Chapter 2: graphene FETs on a SiO_2-Si-SiO_2 substrate, encapsulated by a few nm Al_2O_3, and finished with 10 nm thick periodic metallic ribbon array of various width of equal nominal gap separation. From sample to sample the only difference is the encapsulant thickness ranging from 3 to 20 nm. The ribbon dimensions are intended to be maintained through all the samples; although there are some small lithographic deviations. The spatial THG response of the samples (THG signal map) with no gate voltage applied (intrinsic doping, $V_G = 0$ V) is shown in Fig. 4.7. The main features observed are:

- No transmission, no THG signal through the source and drain contacts (darkest areas).
- Clear difference in THG signal between graphene (blue) and substrate (darker blue).
- Visualization of imperfections such as resist residues due to material change of $\chi^{(3)}$ or light scattering effects.
- No extra THG signal from ribbons directly on substrate.
- Ribbon width modulation of THG signal in the hybrid structure. It will be further discussed later on.

After confirming the energy corresponds with 3ω in Fig. 4.5 and that the signal comes from graphene and the hybrid structures only; the power dependence is studied next. From the slope of the data in Fig. 4.8, the third-order nonlinear process is then proved. Enhancement of more than 2 orders of magnitude in the signal provided by the hybrid structure with respect to graphene only is also observed.

The last check / test to perform include the polarization dependence (see Fig. 4.9). First, the polarizer is placed before the sample revealing no dependence for graphene only except for the detector polarization-dependent efficiency and $\cos^6\theta$ for the hybrid structure, as expected. This dependence is explained due to the polarizing properties of the ribbon array, not surprisingly a holographic wire grid polarizer shares the same arrangement. Hence, for the THG output signal, one must apply the cube of Malus law $I_{THG}(\theta) \propto (\cos^2\theta)^3$. Second and last, if we place the polarizer after the sample while keeping the input polarizer fixed, one observes the regular Malus law. With all these checks it is concluded that there is a THG coherent (because it is preserving polarization) nonlinear process happening both at graphene and at the hybrid structures.

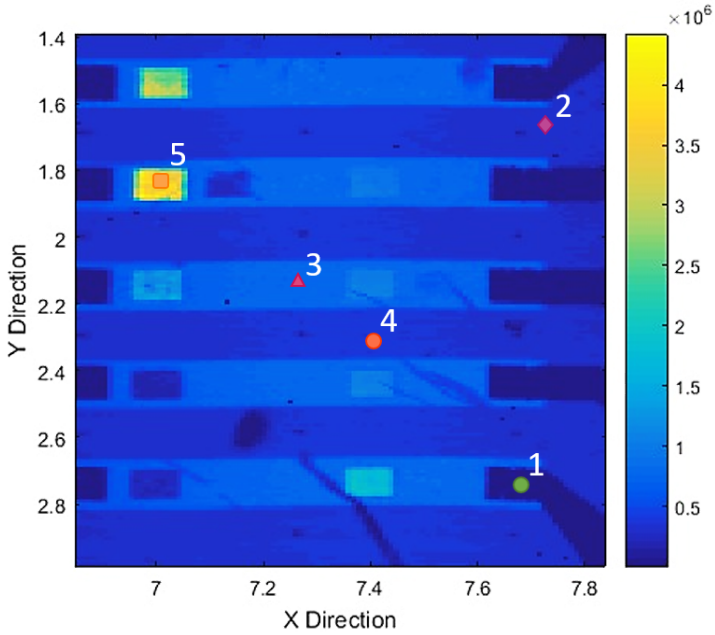

FIGURE 4.7: THG counts image of a sample where 1 is a metal contact, 2 is an area without graphene, 3 is an area containing graphene, 4 is a reference array of metal ribbons (no graphene), and 5 is a hybrid structure.

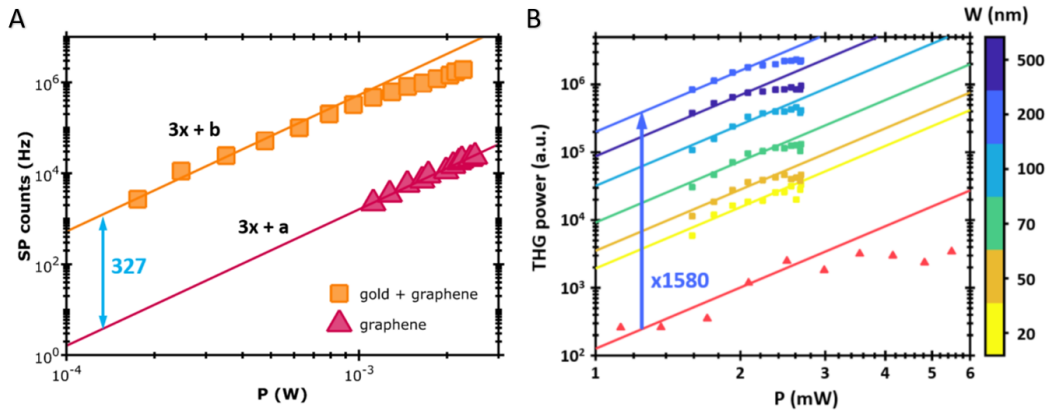

FIGURE 4.8: **A** - 3 nm Al_2O_3 spacer sample THG counts power dependence for graphene only (red triangles) and a hybrid structure (orange squares). **B** - Same as A for the monolayer h−BN spacer sample and all its structure sizes.

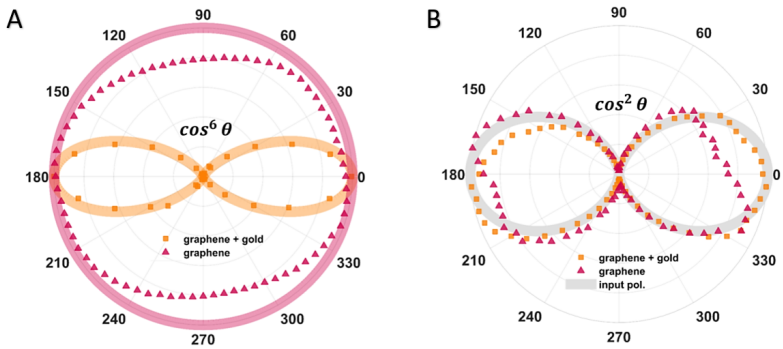

FIGURE 4.9: THG counts polarization dependence with rotating polarizer before (**A**) or after (**B**) the sample.

4.2.3 Planar graphene characterization

Next, we analyze in detail in detail the dependence of the graphene response on several parameters: E_F, Al_2O_3 thickness, and wavelength.

4.2.3.1 E_F dependence

We first analyze in Fig. 4.10 the THG gate dependence of the 5 nm Al_2O_3 encapsulated graphene device. Through this chapter a **positive** sign of $\mathbf{E_F}$ does correspond

to **hole doping** since graphene was heavily p-doped intrinsically, the electron doping was almost unreachable and it is preferred to work with positive numbers. Firstly, a noticeable noise level is detected; and secondly, the background contribution must be subtracted because it is quite large (see Fig. 4.10A). The background signal might have several origins, but the best way to know the value to subtract is by analyzing the Z-scan results. After background subtraction, one realizes there is a signal gate tunability factor of 7.

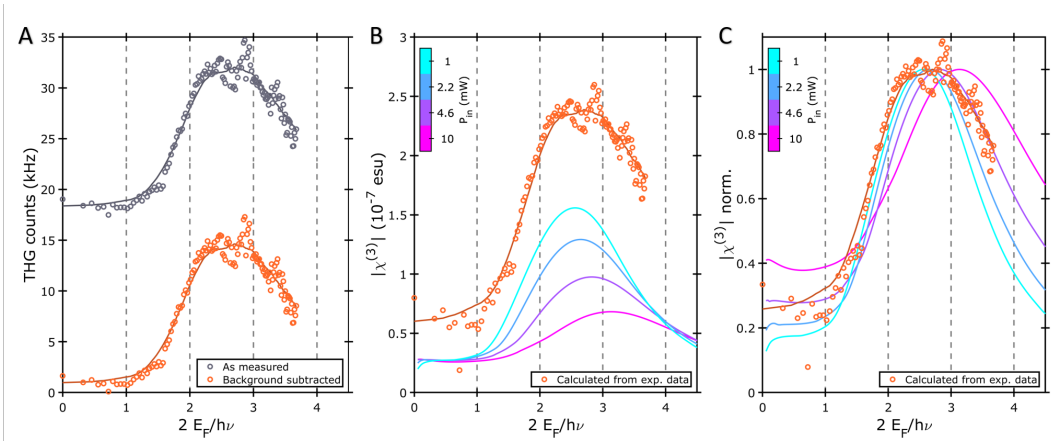

FIGURE 4.10: **A** - Gate dependent graphene THG signal counts as measured and background subtracted ($Net\ Counts_{THG}$) and corresponding $\chi^{(3)}$ calculation compared with simulations (**B**). Normalized simulated $\chi^{(3)}$ and calculated $\sqrt{Net\ Counts_{THG}}$ comparison (**C**).

In order to compare with the simulations, the THG counts must be converted into a $\chi^{(3)}$ values despite it is not very well defined for a 2D material like graphene. The expression for $\chi^{(3)}$ as a function of input $E(\omega_i = \omega)$ and output $E(\omega_o = 3\omega)$ electric field reads:

$$\left|\chi^{(3)}_{exp}\right| = \left|-\frac{i8\pi cE(\omega_o)}{d_g\omega_i E(\omega_i)^3}\right| \quad . \tag{4.10}$$

However, we do not have direct access to the electric fields at graphene experimentally. An alternative to come around is using the relation between the average power and the electric field for a Gaussian beam [180, 190]:

$$P(\omega_{i,o}) = \frac{1}{8}\left(\frac{\pi}{\ln 2}\right)^{3/2} f\tau W^2 n_{\omega_{i,o}} \varepsilon_0 c \frac{|E(\omega_{i,o})|^2}{2}. \tag{4.11}$$

Additionally, on the output side, the counts should be converted into average power accounting for transmission and coupling efficiency using:

$$P(\omega_o) = \frac{Net\ Counts_{THG}\hbar\omega_o}{T_{lens}(\omega_o)\eta_{coupling}(\omega_o)\eta_{detector}(\omega_o)T_{substrate}(\omega_o)}. \tag{4.12}$$

After conversion, when compared with the simulations, the shape apparently agrees with the corresponding input power of 2.2 mW, but it is missing a minor scaling factor to completely match (see Fig. 4.10B). The order of magnitude of the calculation is correct, though. Using a workaround that takes advantage of the fact that $\chi^{(3)} \propto \sqrt{Net\ Counts_{THG}}$, it is possiblte to plot the normalized $\chi^{(3)}$ and $\sqrt{Net\ Counts_{THG}}$ altogether. Accordingly, one observes a perfect match of theory (as described previously including the integral component for not varying field in space) and experiments. The extra features like the peak around 3-photon transition cannot be considered real in this dataset due to the high noise level. In addition, such resonance is not expected to be seen at RT either at the temperature the electrons reach when excited by the pulsed laser.

4.2.3.2 Al_2O_3 thickness dependence

In principle, the few nm encapsulation thickness does not affect the THG. Conversely, it affects the intrinsic doping level of graphene, thus modifying its electrical tuning range as can be seen in Fig. 4.11. Despite that, another obvious difference is the noise level; which is due to the measuring procedure: 3 gate sweeps average results for the 3 nm sample and no averaging for the 5 nm sample.

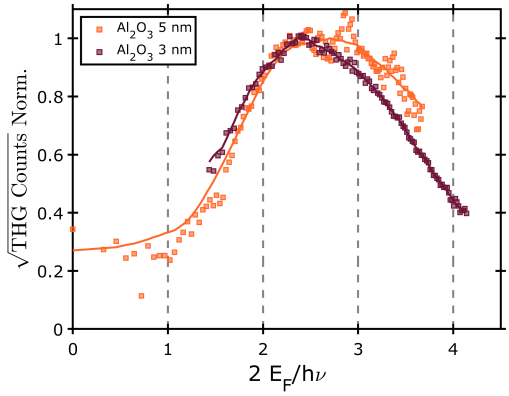

FIGURE 4.11: Encapsulation material thickness dependence of graphene's $\chi^{(3)}$ at $\lambda_i = 5.5\ \mu$m.

4.2.3.3 Wavelength dependence

When using normalized units for $\chi^{(3)}$ in the y-axis and number of photons for interband transition in the x-axis of Fig. 4.12 one observes the same trend for all wavelengths. It is expected due to the type of normalization applied. Please note the x-range diminishes as lambda is also reduced despite being the same sample. It is a natural consequence of normalizing the E_F by the excitation photon energy.

4.2.3.4 Graphene quality

When comparing the calculated values in Fig. 4.3 at RT a minor difference is observed between exfoliated and CVD grown graphene at the given excitation energy (Mid-IR). In order to clearly observe the interband transition resonances, one must use exfoliated graphene at cryogenic temperatures with larger nonlinearity values for $1 < 2E_F/\omega < 3$. Alternatively, one could increase the excitation energy to the NIR as shown in Fig. 4.13 either with exfoliated or CVD graphene. In the NIR, the nonlinear conductivity presents significantly lower values, but E_F tuning capability

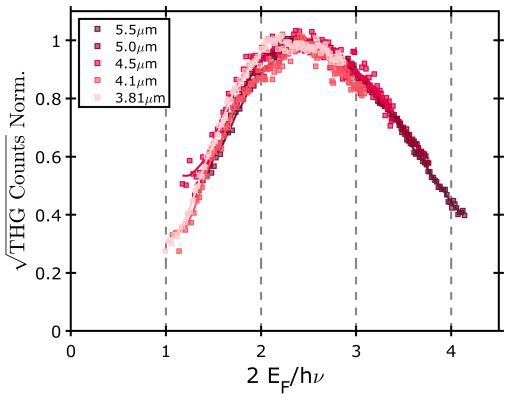

FIGURE 4.12: $\chi^{(3)}$ λ_0 dependence for 3 nm of Al_2O_3 encapsulated graphene.

(even using electrolyte polymer) is in general not able to reach the 3-NIR-photon resonance. However, the detector's sensitivity is greater and there's a larger availability of optical components. This last method was used in [115, 114], where the resonances were visible (except for the third one) and the induced electron temperature was moderate.

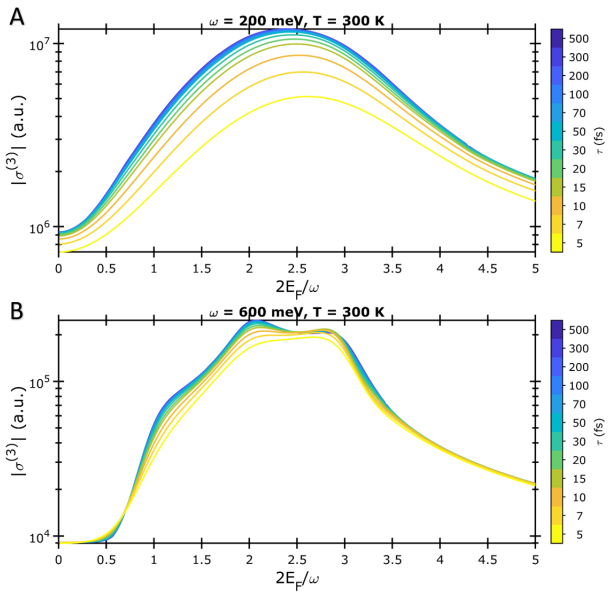

FIGURE 4.13: τ dependence at RT for $\omega = 200$ (top) and 600 meV (bottom).

4.2.4 Hybrid heterostructures characterization

Next, we study the hybrid heterostructures with graphene and their relation with the integral component from eq.4.5. The ribbon width effect in this term is going to be developed first.

4.2.4.1 Ribbon width dependence

On each sample, there were several devices whose nominal (design) metal ribbon width spanned from 20 to 5000 nm while keeping the gap width (distance between adjacent ribbons) constant at 50 nm. In practice, some of the fabricated devices present small deviations from the design geometry. Other devices were simply not lifted-off correctly (possible dose issues) and few graphene stripes result to be leaking electrically to the back-gate, so they were not tunable. In the end, the sample with more working devices had a spacer thickness of 5 nm. Its $\chi^{(3)}$ results corresponding to $E_F = 100$ meV are plotted in Fig. 4.14.

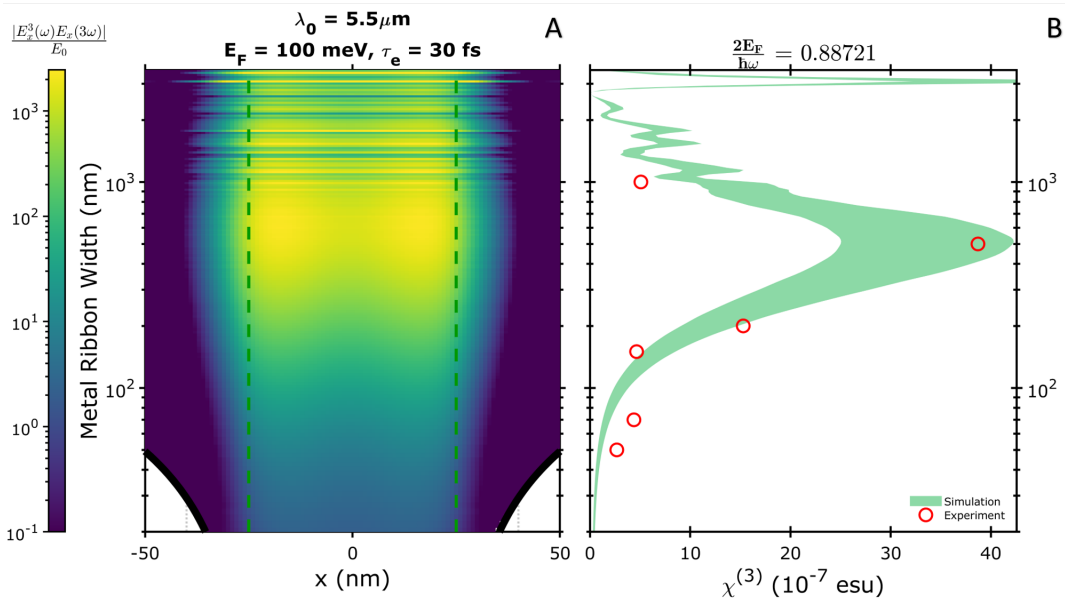

FIGURE 4.14: **A** - In-plane modulus of the electric field integral component centered around the gap region (limited by vertical dashed green lines) and $\chi^{(3)}$ dependence on the metal ribbon width **B**. The region under-metal extends beyond the horizontal limits of the plot for periods > 100 nm (**A**). The shadowed area in **B** corresponds to the range of simulated input average power from 1 to 3 mW with extra $\pm$20% on the $\chi^{(3)}$ values (**B**).

In order to explain the results, one must not forget that metals support surface plasmon polaritons below their plasma frequency. In our case, we observe field enhancement originated by a metal plasmon resonance in the periodic array, which in turn heavily increases the THG from graphene. The effective $\chi^{(3)}$ is increased by an order of magnitude compared to extended graphene. One can say we are using the metal plasmonic field enhancement to enhance in turn the graphene nonlinear response. The previous statement is correct for $2E_F \lesssim \hbar\omega$ i.e. before single-photon interband absorption is blocked and before graphene plasmons can start to be excited ($E_F \gtrsim \hbar\omega$).

4.2.4.2 E_F dependence

To better understand the dielectric / metallic properties and interband / intraband transition effect of the hybrid structure in the THG we must study their gate dependence (E_F tunability). By considering the $\chi^{(3)}$ ($\sqrt{Net - Counts_{THG}}$) enhancement factor of the hybridized structure compared to graphene only (Fig. 4.15), one can observe the effect of the integral component assuming the E_F dependence of $\sigma^{(3)}$ remains unchanged (neglecting light absorption induced heating).

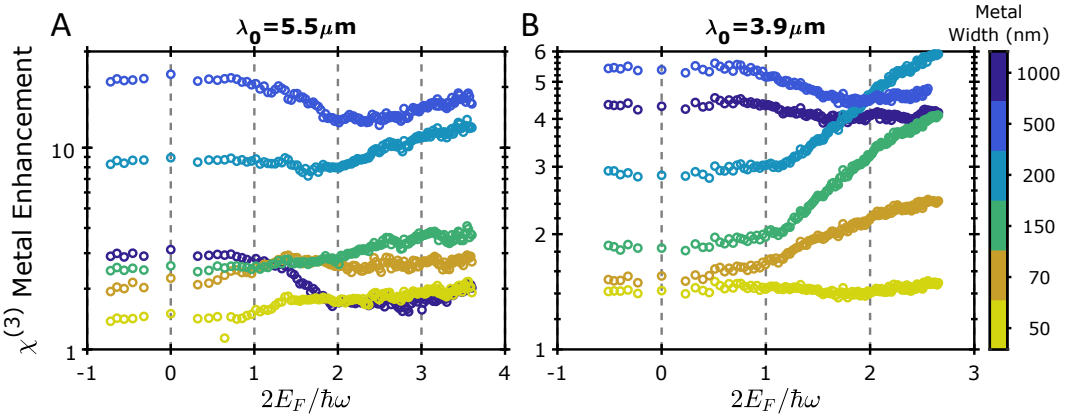

FIGURE 4.15: E_F dependent $\chi^{(3)}$ enhancement of the hybrid structure of Fig. 4.14 at $\lambda_0 = 5.5$ μm and different metal widths.

A $\chi^{(3)}$ enhancement factor up to 22 is observed for the optimum structure at $\lambda_0 = 5.5$ μm. However, this factor is not kept constant through all the doping range. From 0 to 1-photon interband transition energy, the value is constant because graphene is in the interband regime (also the nonlinear response). Later, from 1 to 2-photon interband transition energy, there is the transition through Pauli blocking into the graphene plasmon excitation regime seen as a small decrease of the enhancement (at least for the optimal structure and larger ones). For the other smaller structures, this transition doesn't occur and there is an increment of the enhancement starting already from 1-photon interband transition energy. Once the graphene plasmon regime is reached, the enhancement keeps increasing since for larger carrier concentration the electric plasmonic fields are more intense.

4.2.4.3 Wavelength dependence

We observed for extended graphene that THG response with incident wavelength keeps the overall shape with the proper scaling and it limits the number of photons transitions that can be reached with the gate range. If we perform the same study as in Fig. 4.15A but for a shorter wavelength Fig. 4.15B, one may expect something similar to happen. Meanwhile, an extra effect that modulates the integral component comes into play: by changing the excitation wavelength, the metal plasmon resonance condition is shifted towards smaller structures and possibly not matching any of the fabricated ones.

In fact, the explanation is equivalent to the previously mentioned but the enhancement observed has been reduced considerably. A more interesting case is going to be studied next (Fig. 4.16), where a possible graphene plasmonic resonance is adding some extra features to $\chi^{(3)}$ for $\lambda_0 = 5.5$ μm.

Again, the features can be explained in the same terms as before except for the "dip" around 3 photons on device 1A for 5.5 μm. Further details to come about this curve.

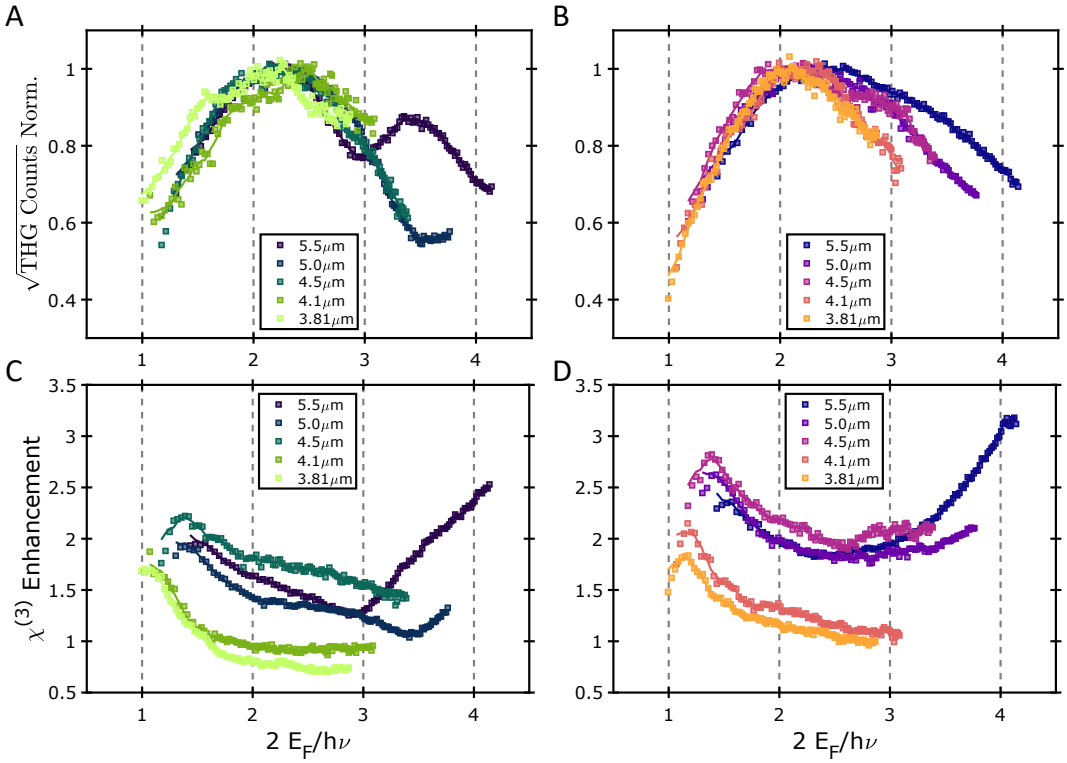

FIGURE 4.16: E_F dependent normalized $\chi^{(3)}$ (**A** and **B**) and $\chi^{(3)}$ enhancement (**C** and **D**) of two hybrid structures of 3 nm Al_2O_3 spacer and equal nominal metal widths. Device 1A (**A** and **C**) was fabricated with a lower e-Beam dose than 1B (**B** and **D**), which makes 1A metal ribbons to be narrower than in 1B, 47 nm vs. 55 nm in a 100 nm period.

4.2.4.4 Graphene plasmon resonance

Simulations of Fig. 4.17 aim to develop an understanding of the features of the 5.5 μm curve shown in Fig. 4.16A by comparing them. The reader must recall that the nonlinear current (polarizability) responsible of the THG ($\chi^{(3)}$) has two main varying contributions: the third-order nonlinear graphene conductivity and the nonlinear field integral (dashed-dotted and dashed lines in Fig. 4.17A, respectively).

The first contribution is governed by the excitation frequency ω, graphene's E_F and τ in addition to T_e (calculated from light absorption in RCWA simulations) which causes additional dips/tips and/or maximum conductivity shift in doping compared to constant T_e (see Fig. 4.18). Dips in conductivity appear as a consequence of absorption due to weak plasmonic resonances at specific doping levels which

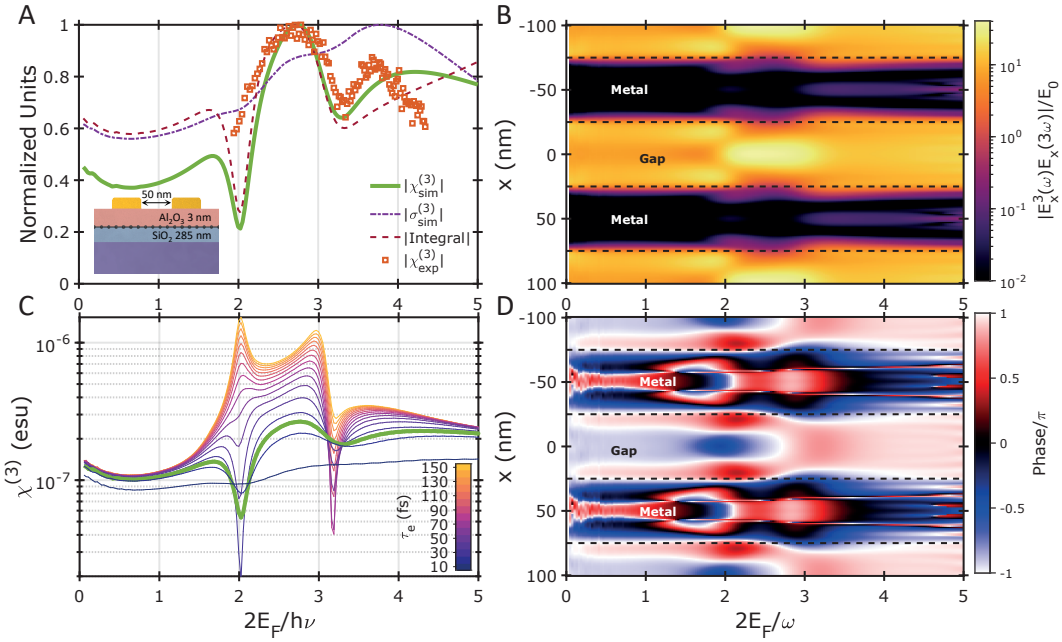

FIGURE 4.17: **A** - Gate dependent magnitudes at $\lambda_0 = 5.5\ \mu$m, normalized to their maximum: experimental (squares) and simulated (solid line) third order nonlinear susceptibility $\chi^{(3)}$, third order nonlinear conductivity $\sigma^{(3)}$ (dashed-dotted line) and, nonlinear in-plane field at graphene $\left|E_x^3(\omega)E_x(3\omega)\right|$ per period or also called field integral result (dashed line). The complex multiplication of the last two ($\sigma^{(3)}$ and the integral result) is proportional to $\chi^{(3)}$. The integral result is obtained from the complex integration of the simulated gate dependent spatial distribution of the nonlinear in-plane field at graphene, which is shown in **B** and **D** as modulus and phase, respectively for 2 periods of the structure in the inset of the panel A. **C** - Simulated $\chi^{(3)}$ τ dependence for $P_{av} = 10$ mW. The simulation electron relaxation time in panels B and D, and the green curves in A and C is 25 fs.

increase T_e, while tips may occur if the plasmonic resonance is much stronger. The maximum value shift is a consequence of the laser fluence: a greater input power causes more energy to be introduced in the system proportionally to the linear absorption coefficient for all doping levels.

The second contribution depends only on the spatial field distribution which is a consequence of graphene linear conductivity variation with E_F. This, in turn, modifies the plasmon wavelength differently for both gap and under the metal regions (see Fig. 4.17B,C). Spatial regions of opposite values cancel each other partially being their imbalance fundamentally responsible for the integral value. In other words, the net nonlinear current for a fixed nonlinear conductivity (at given

doping) is determined by the net nonlinear field in the structure's period.

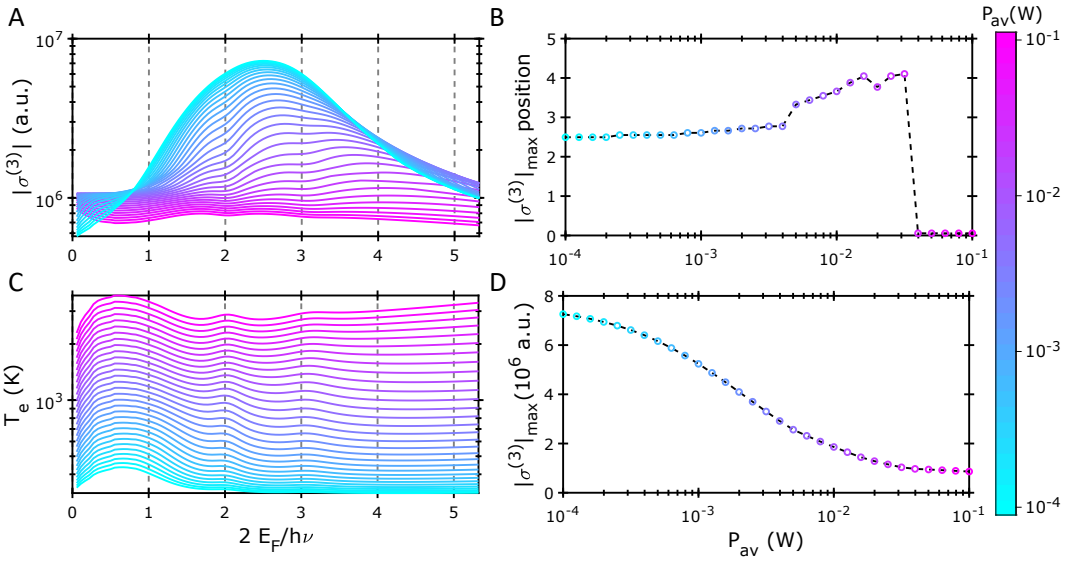

FIGURE 4.18: **A** - Simulated $\sigma^{(3)}$ incoming power P_{av} evolution of the E_F dependence of including T_e due to light absorption (**C**). **B** - Evolution with incomping power of $\sigma^{(3)}$ position of the maximum. **D** - Power evolution of $\sigma^{(3)}$ maximum value.

The nonlinear response is mainly driven by the field in the gap region (no metal above) because it is larger than under the metal (see Fig. 4.17B), especially because the 3ω component is more than 1 order of magnitude smaller under the metal (see Fig. 4.19). However, the experimental dip above three interband photons transition energy is explained by the partial cancellation of positive and negative complex field components throughout the whole period, which yields a diminished $\chi^{(3)}$. A quantitative match of $\chi^{(3)}$ is almost impossible due to sample imperfections and experimental/simulated unknowns/mismatches.

As a first example, the effective electron relaxation time used for the linear response simulations, which can vary with E_F, does not correspond with graphene's intrinsic one, and hence, neither it does for the nonlinear calculations. A second example relates to the linear simulation results, where field and absorption amplitudes do not match the experimental values even when there is good qualitative agreement. The effective electron relaxation time accounts for fabrication imperfections and inhomogeneous broadening in general in a qualitative manner. Variations of τ_e in Fig. 4.17C calculations provide means to approximately address some of the previously mentioned issues. The input average power is an additional parameter that

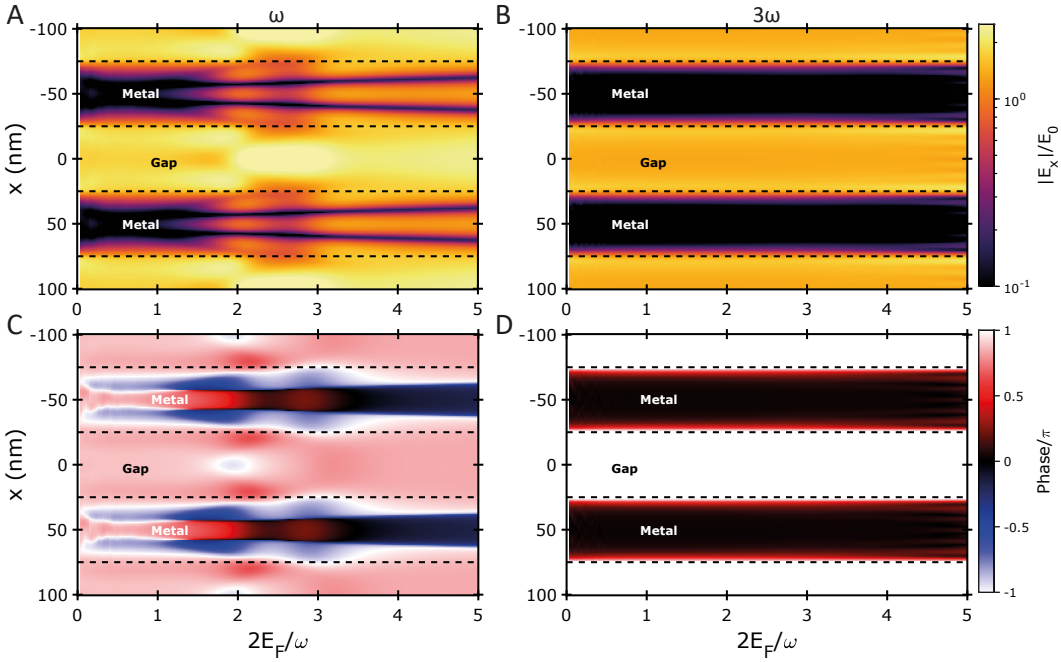

FIGURE 4.19: E_x in graphene spatial distribution of the modulus and the phase for ω (**A**,**C**) and 3ω (**B**,**D**) using $\tau_e = 25$ fs.

compensates for the inaccuracy of the linear simulations.

With the help of these two free parameters it is possible to explain the plasmonic nature of the experimental dip inf Fig. 4.17A. As shown in Fig. 4.13, varying τ_e above 20 fs introduces negligible changes in $\sigma^{(3)}$. However, high values of τ_e greatly enhance the plasmonic fields and their corresponding response. When τ_e variation is applied to THG (Fig. 4.17C), one observes that even though the near-field might be locally large, the resulting period average can vanish if the screened (acoustic, under the metal) and not screened (optical, in the gap) plasmons reach an equilibrium.

The evolution of this effect with E_F is clear by comparing Fig. 4.16 with the field enhancement in Fig. 4.19. For $2E_F/h\nu < 1$, there are no plasmons excited at graphene and the THG enhancement is localized in the gap, thanks to the metal ribbons great near-field. If $2E_F/h\nu > 1$, graphene plasmons (both types) can be excited, thus creating additional local currents which modulate the signal in comparison to graphene only.

Conclusions

Goal 1

This thesis has fulfilled the condition of efficient plasmon excitation in unpatterned graphene from far-field by adapting an old technique used in 2-DEGs. It allowed exciting the so-called acoustic plasmons (in the 2-DEG community they were called gate plasmons) in graphene as well as regular graphene plasmons.

These new modes have been characterized in detail by experimental observation of the resulting extinction resonances provided by different device geometries. Carrier concentration (E_F), metal width (w) / structure period (p), and spacer thickness (s) dependencies of the resonances were extracted. The method has been demonstrated to be fully compatible with high-quality graphene with a successful initial test sample. Detrimental quality in graphene caused by the e-beam lithography remains unstudied.

Goal 2

By using a monolayer spacer material (h$-$BN) it was possible to reach the one atom plasmonic confinement limit (out-of-plane). After comparing the experimental results with the RCWA simulations, a large contribution of the metal nonlocal permittivity was found. It had to be modeled as a thicker dielectric layer for the RCWA simulations to match in position. Additionally, it was found that the energy was located partially inside the metal. It was a consequence of the material nonlocal permittivity, which permits field penetration in the metal. Despite the ambiguity of the location of maximum field (or energy) concentration, the studied structures opened a path towards ultrastrong light-matter interactions.

Goal 3

The fulfillment of the linear optics goals stablished the basis to explore the nonlinear optical response of graphene with especial emphasis in THG. Previous to this thesis, experimental studies of THG from graphene reached doping levels inferior

to 1.5 times the excitation energy, thus not being able to resolve all the expected resonances. In this thesis, the observation of a larger E_F range of the graphene nonlinear optical response has been achieved, such that the interband excitation energy matched the energy of four photons. The value of $\chi^{(3)}$ presents a large uncertainty by its definition. However, there was good correspondence between experimental and simulated values: the normalized trends overlapped perfectly. Those trends included 1, 2, and 3-photon resonant interband transitions in the nonlinear optical conductivity of graphene that are thermally smeared in the current experimental conditions.

In order to clearly observe the aforementioned resonances in MIR, it is concluded from the simulations that cryogenic temperatures with low pump power and reasonable graphene quality are required. On the other hand, if the resonances are to be observed in the NIR at RT, CVD graphene will suffice in terms of quality; but the experimentally achievable carrier density will not be sufficiently high to observe all the features (as it was reported in [114, 115]).

Goal 4

The combination of the hybrid heterostructures with the high intrinsic nonlinear optical properties of graphene enables great success in the fourth goal. More than 2 orders of magnitude enhancement were reported for Al_2O_3 encapsulation and more than 3 orders of magnitude if the spacer is monolayer h$-$BN, an insulating 2D-material.

An interesting effect is retrieved from the results: the output not only depends on the field enhancement but on the field distribution too. It allows a new control channel for the nonlinear optical process by tuning the E_F on and off the plasmonic resonance with expected large on/off ratio of the harmonics signals for the appropriate device.

Global Conclusions

The study of the ultimate confinement has been widely cited, thus demonstrating its impact in the community.
Some examples are found in [30, 33, 54, 81, 164, 191, 192]. It is worth mentioning that unpublished projects in the group arise from the success of the preliminary results of this project. On the other hand, the nonlinear work is yet to be published but it is expected to be of great importance in the field of nonlinear optics with graphene.

Appendix A

Graphene nonlinear Conductivity

A.1 Second order nonlinear conductivity

The second order nonlinear conductivity, consequence of the nonlocal conductivity, reads[130, 121]:

$$\sigma_{\omega}^{22,A} = \frac{\mp ie^3 v_F^2}{4\pi\hbar^2} \frac{1}{(2\omega + i\tau^{-1})(\omega + i\tau^{-1})} \left(\frac{3}{\omega + i\tau^{-1}} + \frac{4}{2\omega + i\tau^{-1}} \right), \tag{A.1}$$

$$\sigma_{\omega}^{22,B} = \frac{\mp ie^3 v_F^2}{4\pi\hbar^2} \frac{1}{(2\omega + i\tau^{-1})(\omega + i\tau^{-1})} \left(\frac{-1}{\omega + i\tau^{-1}} + \frac{4}{2\omega + i\tau^{-1}} - \frac{4}{\omega} \right), \tag{A.2}$$

$$\sigma_{\omega}^{22,C} = \frac{\mp ie^3 v_F^2}{4\pi\hbar^2} \frac{1}{(2\omega + i\tau^{-1})(\omega + i\tau^{-1})} \left(\frac{1/2}{\omega + i\tau^{-1}} + \frac{2}{2\omega + i\tau^{-1}} - \frac{2}{\omega} \right), \tag{A.3}$$

A.2 Third order nonlinear conductivity

The third order nonlinear conductivity from [121]:

$$\sigma_{\omega}^{33} = \frac{3ie^4 v_F^2}{4\pi\hbar^2 E_F} \frac{1}{(3\omega + i\tau^{-1})(2\omega + i\tau^{-1})(\omega + i\tau^{-1})}, \tag{A.4}$$

gives similar results to the more complicated expression for the third harmonic generated waves given by [128]:

$$\frac{I_{3\omega}}{I_{\omega}} = \left(\frac{q^4}{\hbar^2 c^2} \frac{I_{\omega}}{\pi n_s^2 \hbar v_F^2} \right)^2 \left| \mathcal{S}_{xxx}^{(3)}(\Omega, \Omega, \Omega) \right|^2, \tag{A.5}$$

where $\mathcal{S}^{(3)}_{xxx}(\Omega,\Omega,\Omega)$ is a dimensionless function that includes the contribution of (3/0), (2/1), (1/2), and (0/3) terms. To continue using Mikhailov's [128] formalism, the next definition should be considered:

$$\Omega = \frac{\hbar\omega}{|\mu|} \quad \Gamma = \frac{\hbar\gamma}{|\mu|} \tag{A.6}$$

In the most general case, the before mentioned function takes the form:

$$\begin{aligned}\mathcal{S}^{(3)}_{\alpha\beta\gamma\delta}(\Omega_1,\Omega_2,\Omega_3) = \mathcal{S}^{(3/0)}_{\alpha\beta\gamma\delta}(\Omega_1,\Omega_2,\Omega_3) + \mathcal{S}^{(2/1)}_{\alpha\beta\gamma\delta}(\Omega_1,\Omega_2,\Omega_3) \\ +\mathcal{S}^{(1/2)}_{\alpha\beta\gamma\delta}(\Omega_1,\Omega_2,\Omega_3) + \mathcal{S}^{(0/3)}_{\alpha\beta\gamma\delta}(\Omega_1,\Omega_2,\Omega_3).\end{aligned} \tag{A.7}$$

For calculating each of these functions, additional designations need to be introduced:

$$\Delta_{\alpha\beta\gamma\delta} = \delta_{\alpha\beta}\delta_{\gamma\delta} + \delta_{\alpha\gamma}\delta_{\beta\delta} + \delta_{\alpha\delta}\delta_{\beta\delta}, \tag{A.8}$$

$$O_1 = \frac{\Omega_1 + i\Gamma}{2}, \quad O_12 = \frac{\Omega_1 + \Omega_2 + i\Gamma}{2}, \quad O_123 = \frac{\Omega_1 + \Omega_2 + \Omega_3 + i\Gamma}{2}. \tag{A.9}$$

The expression for each one of the four components in Eq. A.7 is then:

$$\mathcal{S}^{(3/0)}_{\alpha\beta\gamma\delta}(\Omega_1,\Omega_2,\Omega_3) = \frac{i\Delta_{\alpha\beta\gamma\delta}}{8O_{123}O_{12}O_1}, \tag{A.10}$$

$$\begin{aligned}\mathcal{S}^{(2/1)}_{\alpha\beta\gamma\delta}(\Omega_1,\Omega_2,\Omega_3) = -\frac{i}{4}\Bigg(\frac{\delta_{\alpha\delta}\delta_{\beta\gamma} + (\Delta_{\alpha\beta\gamma\delta}/4)O_{123}}{O_1O_{12}(1+O_{123})^2} + \frac{\delta_{\alpha\beta}\delta_{\gamma\delta} - \Delta_{\alpha\beta\gamma\delta}/4}{O_1(1+O_{12})(1+O_{123})} \\ +\frac{\delta_{\alpha\gamma}\delta_{\beta\delta} - \Delta_{\alpha\beta\gamma\delta}/4}{O_1(1+O_{12})(1+O_{123})^2} - (\delta_{\alpha\beta}\delta_{\gamma\delta} - \Delta_{\alpha\beta\gamma\delta}/4)\mathcal{J}_1(O_1,O_{12},O_{123}) \\ +(\delta_{\alpha\gamma}\delta_{\beta\delta} - \Delta_{\alpha\beta\gamma\delta}/4)\mathcal{J}_2(O_1,O_{12},O_{123})\Bigg) - \{\text{replace } (O_1,O_{12},O_{123}) \to (O_1,O_{12},O_{123})\},\end{aligned} \tag{A.11}$$

$$\mathcal{S}^{(2/1)}_{\alpha\beta\gamma\delta}(\Omega_1,\Omega_2,\Omega_3)=\frac{i}{4}\left(\frac{\Delta_{\alpha\beta\gamma\delta}/4}{O_1^2O_{12}O_{123}}\ln(1+O_1)+\frac{\Delta_{\alpha\beta\gamma\delta}/4}{O_1O_{12}O_{123}}+\frac{\delta_{\alpha\beta}\delta_{\gamma\delta}-\Delta_{\alpha\beta\gamma\delta}/4}{O_1(1+O_{12})O_{123}}\right.$$
$$\left.-\frac{\delta_{\alpha\beta}\delta_{\gamma\delta}-\Delta_{\alpha\beta\gamma\delta}/4}{O_{123}}\mathcal{J}_3(O_1,O_{12})+\frac{\delta_{\alpha\gamma}\delta_{\beta\delta}-\Delta_{\alpha\beta\gamma\delta}/4}{O_{123}}\mathcal{J}_4(O_1,P_{12})\right)$$
$$-\{\text{replace }(O_1,O_{12},O_{123})\to(O_1,O_{12},O_{123})\},\tag{A.12}$$

$$\mathcal{S}^{(0/3)}_{\alpha\beta\gamma\delta}(\Omega_1,\Omega_2,\Omega_3)=\frac{i\Delta_{\alpha\beta\gamma\delta}}{32O_{12}}\mathcal{J}_5(O_1,O_{123}).\tag{A.13}$$

Here $\mathcal{J}_i$ terms correspond to integrals defined as:

$$\mathcal{J}_1(a,b,c)=\int_1^\infty\frac{dx}{(x+a)(x+b)(x+c)}\left(\frac{1}{x^2}+\frac{1}{x(x+c)}-\frac{1}{(x+b)(x+c)}-\frac{2}{(x+c)^2}\right),\tag{A.14}$$

$$\mathcal{J}_2(a,b,c)=\int_1^\infty\frac{dx}{x(x+a)(x+b)^2(x+c)}\tag{A.15}$$

$$\mathcal{J}_3(a,b,c)=\int_1^\infty\frac{dx}{x^2(x+a)(x+b)}\tag{A.16}$$

$$\mathcal{J}_4(a,b,c)=\int_1^\infty\frac{dx}{x(x+a)(x+b)^2}\tag{A.17}$$

$$\mathcal{J}_5(a,b,c)=\int_1^\infty\frac{dx}{x^2}\left(\frac{1}{x+a}-\frac{1}{x-a}\right)\left(\frac{1}{x+b}-\frac{1}{x-b}\right).\tag{A.18}$$

List of Figures

Bibliography

[1] K S Novoselov et al. “Electric Field Effect in Atomically Thin Carbon Films”. In: *Science* 5.1 (2004), pp. 1–12. ISSN: 00092509. DOI: 10.1126/science.aab1343. arXiv: arXiv:1402.6991v1.

[2] K. S. Novoselov et al. “Two-dimensional gas of massless Dirac fermions in graphene”. In: *Nature* 438.7065 (Nov. 2005), pp. 197–200. ISSN: 0028-0836. DOI: 10.1038/nature04233.

[3] V. P. Gusynin and S. G. Sharapov. “Unconventional Integer Quantum Hall Effect in Graphene”. In: *Physical Review Letters* 95.14 (Sept. 2005), p. 146801. ISSN: 0031-9007. DOI: 10.1103/PhysRevLett.95.146801.

[4] A.K. Geim and K S Novoselov. “The rise of graphene.” In: *Nature materials* 6.3 (2007), pp. 183–191.

[5] Yuri Zuev, Willy Chang, and Philip Kim. “Thermoelectric and Magnetothermoelectric Transport Measurements of Graphene”. In: *Phys. Rev. Lett.* 102.9 (Mar. 2009), p. 96807. ISSN: 0031-9007. DOI: 10.1103/PhysRevLett.102.096807.

[6] A C. Ferrari et al. “Raman spectrum of graphene and graphene layers”. In: *Physical Review Letters* 97.18 (Oct. 2006), p. 187401. ISSN: 00319007. DOI: 10.1103/PhysRevLett.97.187401. arXiv: 0606284v1 [cond-mat].

[7] Ji Eun Lee et al. “Optical separation of mechanical strain from charge doping in graphene”. In: *Nature Communications* 3 (2012). ISSN: 20411723. DOI: 10.1038/ncomms2022.

[8] H. Itoh et al. “Scanning tunneling microscopy of monolayer graphite epitaxially grown on a TiC(111) surface”. In: *Surface Science Letters* 254.1-3 (Aug. 1991). ISSN: 01672584. DOI: 10.1016/0167-2584(91)90005-C.

[9] H.P. Boehm et al. “Surface properties of extremely thin graphite lamellae”. In: *Proceedings of the Fifth Conference on Carbon*. Elsevier, 1962, pp. 73–80. DOI: 10.1016/b978-0-08-009707-7.50013-3.

[10] H. P. Boehm et al. “Das Adsorptionsverhalten sehr dünner Kohlenstoff-Folien”. In: *ZAAC - Journal of Inorganic and General Chemistry* 316.3-4 (July 1962), pp. 119–127. ISSN: 15213749. DOI: 10.1002/zaac.19623160303.

[11] R. F. Davis. "Epitaxial growth and characterization of β-SiC thin films". In: *Journal of the Electrochemical Society* 132.3 (1985), pp. 642–648. ISSN: 19457111. DOI: 10.1149/1.2113921.

[12] Xuekun Lu et al. "Tailoring graphite with the goal of achieving single sheets". In: *Nanotechnology* 10.3 (Sept. 1999), pp. 269–272. ISSN: 09574484. DOI: 10.1088/0957-4484/10/3/308.

[13] Umar Khan et al. "High-Concentration Solvent Exfoliation of Graphene". In: *Small* 6.7 (Apr. 2010), pp. 864–871. ISSN: 16136810. DOI: 10.1002/smll.200902066.

[14] Khaled Parvez et al. "Exfoliation of graphene via wet chemical routes". In: *Synthetic Metals* 210 (Dec. 2015), pp. 123–132. ISSN: 03796779. DOI: 10.1016/j.synthmet.2015.07.014.

[15] Alfonso Reina et al. "Large Area, Few-Layer Graphene Films on Arbitrary Substrates by Chemical Vapor Deposition". In: *Nano Letters* 9.1 (Jan. 2009), pp. 30–35. ISSN: 1530-6984. DOI: 10.1021/nl801827v.

[16] Maria Losurdo et al. "Graphene CVD growth on copper and nickel: Role of hydrogen in kinetics and structure". In: *Physical Chemistry Chemical Physics* 13.46 (Dec. 2011), pp. 20836–20843. ISSN: 14639076. DOI: 10.1039/c1cp22347j.

[17] Yi Zhang, Luyao Zhang, and Chongwu Zhou. "Review of Chemical Vapor Deposition of Graphene and Related Applications". In: *Accounts of Chemical Research* 46.10 (Oct. 2013), pp. 2329–2339. ISSN: 0001-4842. DOI: 10.1021/ar300203n.

[18] Luca Banszerus et al. "Ultrahigh-mobility graphene devices from chemical vapor deposition on reusable copper". In: *Science Advances* 1.6 (2015). ISSN: 23752548. DOI: 10.1126/sciadv.1500222.

[19] T. A. Land et al. "STM investigation of single layer graphite structures produced on Pt(111) by hydrocarbon decomposition". In: *Surface Science* 264.3 (Mar. 1992), pp. 261–270. ISSN: 00396028. DOI: 10.1016/0039-6028(92)90183-7.

[20] Peter Sutter. "Epitaxial graphene: How silicon leaves the scene". In: *Nature Materials* 8.3 (2009), pp. 171–172. ISSN: 14764660. DOI: 10.1038/nmat2392.

[21] Konstantin V. Emtsev et al. "Towards wafer-size graphene layers by atmospheric pressure graphitization of silicon carbide". In: *Nature Materials* 8.3 (2009), pp. 203–207. ISSN: 14764660. DOI: 10.1038/nmat2382.

[22] Wei Yang et al. "Epitaxial growth of single-domain graphene on hexagonal boron nitride". In: *Nature Materials* 12.9 (2013), pp. 792–797. ISSN: 14764660. DOI: 10.1038/nmat3695.

[23] *2D Structures Table*. URL: https://www.materialscloud.org/discover/2dstructures/dashboard/ptable.

[24] Nicolas Mounet et al. "Two-dimensional materials from high-throughput computational exfoliation of experimentally known compounds". In: *Nature Nanotechnology* 13.3 (Mar. 2018), pp. 246–252. ISSN: 17483395. DOI: 10.1038/s41565-017-0035-5. arXiv: 1611.05234.

[25] *Computational 2D materials database - Search*. URL: https://cmrdb.fysik.dtu.dk/c2db.

[26] Sten Haastrup et al. *The Computational 2D Materials Database: High-throughput modeling and discovery of atomically thin crystals*. Sept. 2018. DOI: 10.1088/2053-1583/aacfc1. arXiv: 1806.03173.

[27] A K Geim and I V Grigorieva. "Van der Waals heterostructures". In: *Nature* 499.7459 (July 2013), pp. 419–425. ISSN: 1476-4687. DOI: 10.1038/nature12385.

[28] Andrea C Ferrari et al. "Nanoscale Science and technology roadmap for graphene, related two-dimensional crystals, and hybrid systems". In: *Nanoscale* 7 (2015), p. 4598. ISSN: 2040-3364. DOI: 10.1039/c4nr01600a.

[29] K. S. Novoselov et al. "2D materials and van der Waals heterostructures". In: *Science* 353.6298 (2016), aac9439. ISSN: 0036-8075. DOI: 10.1126/science.aac9439. arXiv: arXiv:1411.1235v1.

[30] Justin C W Song and Nathaniel M Gabor. "PersPective | FOCUS Electron quantum metamaterials in van der Waals heterostructures". In: *Nature Nanotechnology* (). DOI: 10.1038/s41565-018-0294-9.

[31] Victor Ryzhii. "Terahertz plasma waves in gated graphene heterostructures". In: *Japanese Journal of Applied Physics, Part 2: Letters* 45.33-36 (Sept. 2006), pp. L923–L925. ISSN: 00214922. DOI: 10.1143/JJAP.45.L923.

[32] Victor W Brar et al. "Hybrid Surface-Phonon-Plasmon Polariton Modes in Graphene/Monolayer h-BN Heterostructures". In: *Nano Lett.* 14.7 (2014), pp. 3876–3880. ISSN: 1530-6992. DOI: 10.1021/nl501096s.

[33] Matthew Yankowitz et al. "van der Waals heterostructures combining graphene and hexagonal boron nitride". In: *Nature Reviews Physics* (). DOI: 10.1038/s42254-018-0016-0.

[34] Achim Woessner et al. "Highly confined low-loss plasmons in graphene–boron nitride heterostructures". In: *Nature Materials* 14.4 (2015), pp. 421–425. ISSN: 1476-1122. DOI: 10.1038/nmat4169. arXiv: 1409.5674.

[35] M. Massicotte et al. "Photo-thermionic effect in vertical graphene heterostructures". In: *Nature Communications* 7 (2016), pp. 1–7. ISSN: 20411723. DOI: 10.1038/ncomms12174. arXiv: 1601.04197.

[36] A. Rodríguez Echarri, Joel D. Cox, and F. Javier García de Abajo. "Quantum effects in the acoustic plasmons of atomically thin heterostructures". In: *Optica* 6.5 (May 2019), p. 630. ISSN: 2334-2536. DOI: 10.1364/OPTICA.6.000630.

[37] L Britnell et al. "Field-Effect Tunneling Transistor Based on Vertical Graphene Heterostructures". In: *Science* 335.6071 (Feb. 2012), pp. 947–950. ISSN: 10959203. DOI: 10.1126/science.1215193.

[38] I. V. Iorsh et al. "Rashba plasmon polaritons in semiconductor heterostructures". In: (Jan. 2013), pp. 1–4. arXiv: 1301.5181.

[39] B. Zhao and Z. M. Zhang. "Enhanced Photon Tunneling by Surface Plasmon–Phonon Polaritons in Graphene/hBN Heterostructures". In: *Journal of Heat Transfer* 139.2 (2016), p. 022701. ISSN: 0022-1481. DOI: 10.1115/1.4034793.

[40] Junmo Kang et al. *Graphene transfer: Key for applications*. Sept. 2012. DOI: 10.1039/c2nr31317k.

[41] Kamal Asadi et al. "Up-Scaling Graphene Electronics by Reproducible Metal–Graphene Contacts". In: *ACS Applied Materials & Interfaces* 7.18 (May 2015), pp. 9429–9435. ISSN: 1944-8244. DOI: 10.1021/acsami.5b01869.

[42] C R Dean et al. "Boron nitride substrates for high-quality graphene electronics." In: *Nature Nanotechnology* 5.10 (Oct. 2010), pp. 722–726. ISSN: 1748-3395. DOI: 10.1038/nnano.2010.172.

[43] Jeongmin Park et al. "Dual-gated BN-sandwiched multilayer graphene field-effect transistor fabricated by stamping transfer method and self-aligned contact". In: *Current Applied Physics* 15.10 (Oct. 2015), pp. 1184–1187. ISSN: 15671739. DOI: 10.1016/j.cap.2015.07.001.

[44] Yuan Cao et al. "Unconventional superconductivity in magic-angle graphene superlattices". In: *Nature* 556.7699 (Apr. 2018), pp. 43–50. ISSN: 0028-0836. DOI: 10.1038/nature26160.

[45] Guorui Chen et al. "Signatures of tunable superconductivity in a trilayer graphene moiré superlattice". In: *Nature* 572.7768 (Aug. 2019), pp. 215–219. ISSN: 0028-0836. DOI: 10.1038/s41586-019-1393-y.

[46] Matthew Yankowitz et al. "Emergence of superlattice Dirac points in graphene on hexagonal boron nitride". In: *Nature Physics* 8.5 (May 2012), pp. 382–386. ISSN: 17452473. DOI: 10.1038/nphys2272. arXiv: 1202.2870.

[47] Shengxi Huang et al. "Probing the Interlayer Coupling of Twisted Bilayer MoS ₂ Using Photoluminescence Spectroscopy". In: *Nano Letters* 14.10 (Oct. 2014), pp. 5500–5508. ISSN: 1530-6984. DOI: 10.1021/nl5014597.

[48] Rafael Martinez-Gordillo et al. "Transport fingerprints at graphene superlattice Dirac points induced by a boron nitride substrate". In: *Physical Review B - Condensed Matter and Materials Physics* 89.16 (Apr. 2014). ISSN: 1550235X. DOI: 10.1103/PhysRevB.89.161401.

[49] Lei Wang et al. "Evidence for a fractional fractal quantum Hall effect in graphene superlattices". In: *Science* 350.6265 (Dec. 2015), pp. 1231–1234. ISSN: 10959203. DOI: 10.1126/science.aad2102. arXiv: 1505.07180.

[50] Zilu Wang, Qian Chen, and Jinlan Wang. "Electronic Structure of Twisted Bilayers of Graphene/MoS ₂ and MoS ₂ /MoS ₂". In: *The Journal of Physical Chemistry C* 119.9 (Mar. 2015), pp. 4752–4758. ISSN: 1932-7447. DOI: 10.1021/jp507751p.

[51] Po-Chun Yeh et al. "Direct Measurement of the Tunable Electronic Structure of Bilayer MoS ₂ by Interlayer Twist". In: *Nano Letters* 16.2 (Feb. 2016), pp. 953–959. ISSN: 1530-6984. DOI: 10.1021/acs.nanolett.5b03883.

[52] Stephen Carr et al. "Twistronics: Manipulating the electronic properties of two-dimensional layered structures through their twist angle". In: *Physical Review B* 95.7 (Feb. 2017). ISSN: 24699969. DOI: 10.1103/PhysRevB.95.075420. arXiv: 1611.00649.

[53] Mathias S. Scheurer. *Spectroscopy of graphene with a magic twist*. Aug. 2019. DOI: 10.1038/d41586-019-02285-1.

[54] S S Sunku et al. "Photonic crystals for nano-light in moiré graphene superlattices". In: *Science* 362.6419 (2018), pp. 1153–1156. ISSN: 10959203. DOI: 10.1126/science.aau5144.

[55] Xiaobo Lu, Xiaoqin Li, and Li Yang. "Modulated interlayer exciton properties in a two-dimensional moiré crystal". In: *Physical Review B* 100.15 (Oct. 2019). ISSN: 24699969. DOI: 10.1103/PhysRevB.100.155416.

[56] Stefan A. Maier. *Plasmonics: Fundamentals and Applications*. New York, NY: Springer US, 2007. ISBN: 978-0-387-33150-8. DOI: 10.1007/0-387-37825-1.

[57] R. R. Nair et al. "Fine Structure Constant Defines Visual Transparency of Graphene". In: *Science* 315.5811 (June 2008), pp. 490–493.

[58] A. B. Kuzmenko et al. "Universal optical conductance of graphite". In: *Physical Review Letters* 100.11 (Mar. 2008). ISSN: 00319007. DOI: 10.1103/PhysRevLett.100.117401.

[59] T. Stauber, N. M.R. Peres, and A. K. Geim. "Optical conductivity of graphene in the visible region of the spectrum". In: *Physical Review B - Condensed Matter and Materials Physics* 78.8 (Aug. 2008). ISSN: 10980121. DOI: 10.1103/PhysRevB.78.085432. arXiv: 0803.1802.

[60] Feng Wang et al. "Gate-variable optical transitions in graphene". In: *Science* 320.5873 (Apr. 2008), pp. 206–209. ISSN: 00368075. DOI: 10.1126/science.1152793.

[61] Qiaoliang Bao and Kian Ping Loh. "Graphene Photonics, Plasmonics, and Broadband Optoelectronic Devices". In: *ACS Nano* 6.5 (May 2012), pp. 3677–3694. DOI: 10.1021/nn300989g.

[62] K. S. Novoselov et al. "Two-dimensional gas of massless Dirac fermions in graphene". In: *Nature* 438.7065 (Nov. 2005), pp. 197–200. ISSN: 00280836. DOI: 10.1038/nature04233.

[63] Z. Q. Li et al. "Dirac charge dynamics in graphene by infrared spectroscopy". In: *Nature Physics* 4.7 (July 2008), pp. 532–535. ISSN: 1745-2473. DOI: 10.1038/nphys989.

[64] Lei Ren et al. "Terahertz and infrared spectroscopy of gated large-area graphene." In: *Nano letters* 12.7 (July 2012), pp. 3711–5. ISSN: 1530-6992. DOI: 10.1021/nl301496r.

[65] S. Das Sarma and A. Madhukar. "Collective modes of spatially separated, two-component, two-dimensional plasma in solids". In: *Physical Review B* 23.2 (1981), pp. 805–815. ISSN: 01631829. DOI: 10.1103/PhysRevB.23.805.

[66] Viacheslav V. Popov. "Plasmon excitation and plasmonic detection of terahertz radiation in the grating-gate field-effect-transistor structures". In: *Journal of Infrared, Millimeter, and Terahertz Waves* 32.10 (Oct. 2011), pp. 1178–1191. ISSN: 18666892. DOI: 10.1007/s10762-011-9813-6.

[67] V. V. Popov, O. V. Polishchuk, and S. A. Nikitov. "Electromagnetic renormalization of the plasmon spectrum in a laterally screened two-dimensional electron system". In: *JETP Letters* 95.2 (Mar. 2012), pp. 85–90. ISSN: 0021-3640. DOI: 10.1134/S0021364012020075.

[68] Beom Joon Kim et al. "High-Performance Flexible Graphene Field Effect Transistors with Ion Gel Gate Dielectrics". In: 10 (2010), pp. 3464–3466. DOI: 10.1021/nl101559n.

[69] K J Tielrooij et al. "Electrical control of optical emitter relaxation pathways enabled by graphene". In: *Nature Physics* 11.3 (2015), pp. 281–287. ISSN: 17452481. DOI: 10.1038/nphys3204. arXiv: 1410.1361.

[70] Michel Kettner et al. "Ionic gel as gate dielectric for the easy characterization of graphene and polymer field-effect transistors and electrochemical resistance modification of graphene". In: *Journal of Applied Physics* 118.2 (2015). ISSN: 10897550. DOI: 10.1063/1.4923054.

[71] Hai Hu et al. "Broadly tunable graphene plasmons using an ion-gel top gate with low control voltage". In: *Nanoscale* 7.46 (Dec. 2015), pp. 19493–19500. ISSN: 20403372. DOI: 10.1039/c5nr05175d.

[72] Hyunjin Jo et al. "A Hybrid Gate Dielectrics of Ion Gel with Ultra-Thin Passivation Layer for High-Performance Transistors Based on Two-Dimensional Semiconductor Channels". In: *Scientific Reports* 7.1 (Dec. 2017). ISSN: 20452322. DOI: 10.1038/s41598-017-14649-6.

[73] Jin Tae Kim et al. "Ion-Gel-Gated Graphene Optical Modulator with Hysteretic Behavior". In: *ACS Applied Materials & Interfaces* 10.2 (Jan. 2018), pp. 1836–1845. ISSN: 1944-8244. DOI: 10.1021/acsami.7b16600.

[74] Tony Low et al. "Polaritons in layered two-dimensional materials". In: *Nature Mater.* 16.2 (Nov. 2016), pp. 182–194. ISSN: 1476-1122. DOI: 10.1038/nmat4792. arXiv: 1610.04548.

[75] D. N. Basov, M. M. Fogler, and F. J. Garcia de Abajo. "Polaritons in van der Waals materials". In: *Science* 354.6309 (Oct. 2016), aag1992–aag1992. ISSN: 0036-8075. DOI: 10.1126/science.aag1992.

[76] B Wunsch et al. "Dynamical polarization of graphene at finite doping". In: *New J. Phys.* 8.12 (Dec. 2006), p. 318. ISSN: 1367-2630. DOI: 10.1088/1367-2630/8/12/318.

[77] Marinko Jablan, Hrvoje Buljan, and Marin Soljačić. "Plasmonics in graphene at infrared frequencies". In: *Phys. Rev. B* 80.24 (Dec. 2009), p. 245435. ISSN: 1098-0121. DOI: 10.1103/PhysRevB.80.245435.

[78] A N Grigorenko, M Polini, and K S Novoselov. "Graphene plasmonics". In: *Nature Photonics* 6.11 (Nov. 2012), pp. 749–758. ISSN: 1749-4885. DOI: 10.1038/nphoton.2012.262.

[79] Marinko Jablan, Marin Soljacic, and Hrvoje Buljan. "Plasmons in Graphene: Fundamental Properties and Potential Applications". In: *Proceedings of the IEEE* 101.7 (July 2013), pp. 1689–1704. ISSN: 0018-9219. DOI: 10.1109/JPROC.2013.2260115.

[80] F. Javier García de Abajo. "Graphene Plasmonics: Challenges and Opportunities". In: *ACS Photonics* 1.3 (Mar. 2014), pp. 135–152. ISSN: 2330-4022. DOI: 10.1021/ph400147y.

[81] Yuancheng Fan et al. "Graphene Plasmonics: A Platform for 2D Optics". In: *Advanced Optical Materials* 7.3 (2019), pp. 1–14. ISSN: 21951071. DOI: 10.1002/adom.201800537.

[82] Zhe Fei et al. "Infrared Nanoscopy of Dirac Plasmons at the GrapheneÀSiO 2 Interface". In: *Nano Lett* 11 (2011), pp. 4701–4705. DOI: 10.1021/nl202362d.

[83] Z Fei et al. "Gate-tuning of graphene plasmons revealed by infrared nano-imaging." In: *Nature* 487.7405 (July 2012), pp. 82–85. ISSN: 1476-4687. DOI: 10.1038/nature11253.

[84] Jianing Chen et al. "Optical nano-imaging of gate-tunable graphene plasmons". In: *Nature* 487.7405 (June 2012), pp. 77–81. ISSN: 0028-0836. DOI: 10.1038/nature11254.

[85] S Dai et al. "Graphene on hexagonal boron nitride as a tunable hyperbolic metamaterial". In: *Nature Nanotech.* 10.8 (2015), pp. 682–686. ISSN: 1748-3387. DOI: 10.1038/nnano.2015.131.

[86] Mark B. Lundeberg et al. "Thermoelectric detection and imaging of propagating graphene plasmons". In: *Nature Mater.* (Sept. 2016), doi:10.1038/nmat4755. ISSN: 1476-1122. DOI: 10.1038/nmat4755.

[87] Pablo Alonso-González et al. "Acoustic terahertz graphene plasmons revealed by photocurrent nanoscopy". In: *Nature Nanotechnology* 12.1 (Jan. 2017), pp. 31–35. ISSN: 1748-3387. DOI: 10.1038/nnano.2016.185. arXiv: 1601.05753.

[88] Mark B Lundeberg et al. "Tuning quantum nonlocal effects in graphene plasmonics". In: *Science* 357.6347 (2017), pp. 187–191. ISSN: 10959203. DOI: 10.1126/science.aan2735. arXiv: 1704.05518.

[89] A. Principi, Reza Asgari, and Marco Polini. "Acoustic plasmons and composite hole-acoustic plasmon satellite bands in graphene on a metal gate". In: *Solid State Communications* 151.21 (2011), pp. 1627–1630. ISSN: 00381098. DOI: 10.1016/j.ssc.2011.07.015. arXiv: 1104.2707.

[90] Xuefeng Gu, I. Tan Lin, and Jia Ming Liu. "Extremely confined terahertz surface plasmon-polaritons in graphene-metal structures". In: *Applied Physics Letters* 103.7 (2013). ISSN: 00036951. DOI: 10.1063/1.4818660.

[91] Victor W Brar et al. "Highly confined tunable mid-infrared plasmonics in graphene nanoresonators". In: *Nano Letters* 13.6 (2013), pp. 2541–2547. ISSN: 15306984. DOI: 10.1021/nl400601c.

[92] Weilu Gao et al. "Excitation and Active Control of Propagating Surface Plasmon Polaritons in Graphene". In: *Nano Letters* 13.8 (Aug. 2013), pp. 3698–3702. ISSN: 1530-6984. DOI: 10.1021/nl401591k.

[93] Zheyu Fang et al. "Gated tunability and hybridization of localized plasmons in nanostructured graphene". In: *ACS Nano* 7.3 (2013), pp. 2388–2395. ISSN: 19360851. DOI: 10.1021/nn3055835.

[94] Marcus Freitag et al. "Substrate-sensitive mid-infrared photoresponse in graphene." In: *ACS Nano* 8.8 (Aug. 2014), pp. 8350–8356. ISSN: 1936-086X. DOI: 10.1021/nn502822z.

[95] Tony Low and Phaedon Avouris. "Graphene plasmonics for terahertz to mid-infrared applications." In: *ACS nano* 8.2 (Feb. 2014), pp. 1086–101. ISSN: 1936-086X. DOI: 10.1021/nn406627u.

[96] Min Seok Jang et al. "Tunable large resonant absorption in a midinfrared graphene Salisbury screen". In: *Physical Review B* 90.16 (Oct. 2014), p. 165409. ISSN: 1098-0121. DOI: 10.1103/PhysRevB.90.165409.

[97] Zhongli Wang et al. "Experimental demonstration of graphene plasmons working close to the near-infrared window". In: *Opt. Lett.* 41.22 (Nov. 2016), p. 5345. ISSN: 0146-9592. DOI: 10.1364/OL.41.005345.

[98] Victor W Brar et al. "Electronic modulation of infrared radiation in graphene plasmonic resonators". In: *Nature Communications* 6 (2015). ISSN: 20411723. DOI: 10.1038/ncomms8032.

[99] Mohammad M Jadidi et al. "Tunable Terahertz Hybrid Metal-Graphene Plasmons". In: *Nano Letters* 15.10 (2015), pp. 7099–7104. ISSN: 15306992. DOI: 10.1021/acs.nanolett.5b03191.

[100] Seyoon Kim et al. "Electronically tunable extraordinary optical transmission in graphene plasmonic ribbons coupled to subwavelength metallic slit arrays". In: *Nature Communications* 7 (Aug. 2016), p. 12323. ISSN: 20411723. DOI: 10.1038/ncomms12323.

[101] Seyoon Kim et al. "Electronically Tunable Perfect Absorption in Graphene". In: *Nano Letters* 18.2 (Feb. 2018), pp. 971–979. ISSN: 1530-6984. DOI: 10.1021/acs.nanolett.7b04393.

[102] E Hendry et al. "Coherent nonlinear optical response of graphene". In: *Physical Review Letters* 105.9 (2010). ISSN: 00319007. DOI: 10.1103/PhysRevLett.105.097401.

[103] Richard Ciesielski et al. "Graphene Near-Degenerate Four-Wave Mixing for Phase Characterization of Broadband Pulses in Ultrafast Microscopy". In: *Nano Letters* 15.8 (2015), pp. 4968–4972. ISSN: 15306992. DOI: 10.1021/acs.nanolett.5b00893.

[104] Tao Jiang et al. "Ultrafast coherent nonlinear nanooptics and nanoimaging of graphene". In: *Nature Nanotechnology* 14.9 (Sept. 2019), pp. 838–843. ISSN: 1748-3387. DOI: 10.1038/s41565-019-0515-x.

[105] Sung-Young Hong et al. "Optical Third-Harmonic Generation in Graphene". In: *Physical Review X* 3.2 (June 2013), p. 021014. ISSN: 2160-3308. DOI: 10.1103/PhysRevX.3.021014.

[106] Nardeep Kumar et al. "Third harmonic generation in graphene and few-layer graphite films". In: *Physical Review B - Condensed Matter and Materials Physics* 87.12 (Mar. 2013), p. 121406. ISSN: 1098-0121. DOI: 10.1103/PhysRevB.87.121406.

[107] Evdokia Dremetsika et al. "Measuring the nonlinear refractive index of graphene using the optical Kerr effect method". In: *Optics Letters* 41.14 (July 2016), p. 3281. ISSN: 0146-9592. arXiv: 1607.00911.

[108] Naotaka Yoshikawa et al. "High-harmonic generation in graphene enhanced by elliptically polarized light excitation". In: *Science* 356.6339 (May 2017), pp. 736–738. DOI: 10.1126/science.aam8861.

[109] Matthias Baudisch et al. "Ultrafast nonlinear optical response of Dirac fermions in graphene". In: *Nature Communications* 9.1 (Dec. 2018), p. 1018. ISSN: 2041-1723. DOI: 10.1038/s41467-018-03413-7.

[110] Hassan A Hafez et al. *Extremely efficient terahertz high-harmonic generation in graphene by hot Dirac fermions*. 2018. DOI: 10.1038/s41586-018-0508-1.

[111] Dmytro Kundys et al. "Nonlinear Light Mixing by Graphene Plasmons". In: *Nano Letters* 18.1 (Jan. 2018), pp. 282–287. ISSN: 1530-6984. DOI: 10.1021/acs.nanolett.7b04114.

[112] T. J. Constant et al. "All-optical generation of surface plasmons in graphene". In: *Nature Physics* 12.2 (2015), pp. 124–127. ISSN: 1745-2473. DOI: 10.1038/nphys3545. arXiv: 1505.0127.

[113] Mohammad M. Jadidi et al. "Nonlinear Terahertz Absorption of Graphene Plasmons". In: *Nano Letters* 16.4 (Apr. 2016), pp. 2734–2738. ISSN: 1530-6984. DOI: 10.1021/acs.nanolett.6b00405.

[114] Tao Jiang et al. "Gate-tunable third-order nonlinear optical response of massless Dirac fermions in graphene". In: *Nature Photonics* 12.7 (2018), pp. 430–436. ISSN: 17494893. DOI: 10.1038/s41566-018-0175-7. arXiv: 1710.04758.

[115] Giancarlo Soavi et al. "Broadband, electrically tunable third-harmonic generation in graphene". In: *Nature Nanotechnology* 13.7 (2018), pp. 583–588. ISSN: 17483395. DOI: 10.1038/s41565-018-0145-8. arXiv: 1710.03694.

[116] S. A. Mikhailov. "Theory of the giant plasmon-enhanced second-harmonic generation in graphene and semiconductor two-dimensional electron systems". In: *Physical Review B - Condensed Matter and Materials Physics* 84.4 (July 2011). ISSN: 1098-0121. DOI: 10.1103/PhysRevB.84.045432.

[117] A. V. Gorbach. "Nonlinear graphene plasmonics: Amplitude equation for surface plasmons". In: *Physical Review A - Atomic, Molecular, and Optical Physics* 87.1 (Jan. 2013). ISSN: 1050-2947. DOI: 10.1103/PhysRevA.87.013830.

[118] Joel D. Cox and F. Javier García de Abajo. "Electrically tunable nonlinear plasmonics in graphene nanoislands". In: *Nature Communications* 5.1 (Dec. 2014), p. 5725. ISSN: 2041-1723. DOI: 10.1038/ncomms6725.

[119] Marinko Jablan and Darrick E. Chang. "Multiplasmon Absorption in Graphene". In: *Physical Review Letters* 114.23 (2015), pp. 1–6. ISSN: 10797114. DOI: 10.1103/PhysRevLett.114.236801. arXiv: 1501.05258.

[120] Habib Rostami, Mikhail I. Katsnelson, and Marco Polini. "Theory of plasmonic effects in nonlinear optics: The case of graphene". In: *Physical Review B* 95.3 (Jan. 2017). ISSN: 2469-9950. DOI: 10.1103/PhysRevB.95.035416.

[121] Joel D Cox, Renwen Yu, and F. Javier García De Abajo. "Analytical description of the nonlinear plasmonic response in nanographene". In: *Physical Review B* 96.4 (2017), pp. 1–13. ISSN: 24699969. DOI: 10.1103/PhysRevB.96.045442.

[122] Joel D. Cox, Andrea Marini, and F. Javier García de Abajo. "Plasmon-assisted high-harmonic generation in graphene". In: *Nature Communications* 8.1 (Apr. 2017), p. 14380. ISSN: 2041-1723. DOI: 10.1038/ncomms14380.

[123] Joel D. Cox, F. Javier García de Abajo, and F Javier García de Abajo. "Nonlinear Graphene Nanoplasmonics". In: *Accounts of Chemical Research* 52.9 (Sept. 2019), pp. 2536–2547. ISSN: 0001-4842. DOI: 10.1021/acs.accounts.9b00308.

[124] I. Alonso Calafell et al. "Quantum computing with graphene plasmons". In: *npj Quantum Information* 5.1 (Dec. 2019), p. 37. ISSN: 2056-6387. DOI: 10.1038/s41534-019-0150-2.

[125] J L Cheng, N Vermeulen, and J E Sipe. "Third order optical nonlinearity of graphene". In: *New Journal of Physics* 16.5 (May 2014), p. 053014. ISSN: 1367-2630. DOI: 10.1088/1367-2630/16/5/053014.

[126] J. L. Cheng, N. Vermeulen, and J. E. Sipe. "Third-order nonlinearity of graphene: Effects of phenomenological relaxation and finite temperature". In: *Physical Review B - Condensed Matter and Materials Physics* 91.23 (June 2015), p. 235320. ISSN: 1098-0121. DOI: 10.1103/PhysRevB.91.235320.

[127] N. A. Savostianova and S. A. Mikhailov. "Giant enhancement of the third harmonic in graphene integrated in a layered structure". In: *Applied Physics Letters* 107.18 (Nov. 2015), p. 181104. ISSN: 00036951. DOI: 10.1063/1.4935041. arXiv: 1510.06146.

[128] S A Mikhailov. "Quantum theory of the third-order nonlinear electrodynamic effects of graphene". In: *Physical Review B* 93.8 (2016), pp. 1–29. ISSN: 24699969. DOI: 10.1103/PhysRevB.93.085403. arXiv: 1506.00534.

[129] M Gullans et al. “Single-Photon Nonlinear Optics with Graphene Plasmons”. In: *Phys. Rev. Lett.* 111.24 (Dec. 2013), p. 247401. ISSN: 0031-9007. DOI: 10.1103/PhysRevLett.111.247401.

[130] M T Manzoni et al. “Second-order quantum nonlinear optical processes in single graphene nanostructures and arrays”. In: *New Journal of Physics* 17.8 (2015), p. 083031. ISSN: 1367-2630. DOI: 10.1088/1367-2630/17/8/083031.

[131] G. S. Painter and D. E. Ellis. “Electronic band structure and optical properties of graphite from a variational approach”. In: *Physical Review B* 1.12 (1970), pp. 4747–4752. ISSN: 01631829. DOI: 10.1103/PhysRevB.1.4747.

[132] A. H.. Castro Neto et al. “The electronic properties of graphene”. In: *Reviews of Modern Physics* 81.1 (2009), pp. 109–162. ISSN: 0034-6861. DOI: 10.1103/RevModPhys.81.109. arXiv: 0709.1163.

[133] P R Wallace and P R War Ace. “The Band Theory of Graphite”. In: *Phys. Rev.* 71 (1947). DOI: https://doi.org/10.1103/PhysRev.71.622.

[134] Yuanbo Zhang et al. “Experimental observation of the quantum Hall effect and Berry’s phase in graphene”. In: *Nature* 438.7065 (Nov. 2005), pp. 201–204. ISSN: 0028-0836. DOI: 10.1038/nature04235.

[135] Jilin Xia et al. “Measurement of the quantum capacitance of graphene”. In: *Nature Nanotechnology* 4.8 (2009), pp. 505–509. ISSN: 17483395. DOI: 10.1038/nnano.2009.177.

[136] Neil W. Ashcroft and N. David. Mermin. *Solid state physics*. New York: Holt, Rinehart and Winston, 1976, p. 826. ISBN: 9780030839931.

[137] Charles Kittel. *Introduction to Solid State Physics*. 8th. London: John Wiley & Sons, Inc., 2004, p. 704. ISBN: 9780471415268.

[138] *Introduction - Topology in Condensed Matter*. URL: https://topocondmat.org/w3%7B%5C_%7Dpump%7B%5C_%7DQHE/Laughlinargument.html.

[139] John David Jackson. *Classical electrodynamics*. Wiley, 1999, p. 808. ISBN: 9780471309321.

[140] Frank H.L. Koppens, Darrick E Chang, and F. Javier García De Abajo. “Graphene plasmonics: A platform for strong light-matter interactions”. In: *Nano Letters* 11.8 (Aug. 2011), pp. 3370–3377. ISSN: 15306984. DOI: 10.1021/nl201771h. arXiv: 1104.2068.

[141] N D Mermin. “Lindhard Dielectric Function in the Relaxation-Time Approximation”. In: *Physical Review B* 1.5 (1970), pp. 2362–2363.

[142] Pierre F. Maldague. “Many-body corrections to the polarizability of the two-dimensional electron gas”. In: *Surface Science* 73 (May 1978), pp. 296–302. ISSN: 0039-6028. DOI: 10.1016/0039-6028(78)90507-1.

[143] *Modeling methodology*. URL: https://apps.lumerical.com/other%7B%5C_%7Dapplication%7B%5C_%7Dgraphene%7B%5C_%7Dsimulation%7B%5C_%7Dtips.html.

[144] George W Hanson. "Dyadic Green's functions and guided surface waves for a surface conductivity model of graphene". In: *Journal of Applied Physics* 103.6 (2008). ISSN: 00218979. DOI: 10.1063/1.2891452. arXiv: 0701205 [cond-mat].

[145] L A Falkovsky. "Optical properties of graphene". In: *Journal of Physics: Conference Series* 129.1 (Oct. 2008), p. 012004. ISSN: 1742-6596. DOI: 10.1088/1742-6596/129/1/012004.

[146] Lifeng Li. *Use of Fourier series in the analysis of discontinuous periodic structures*. Sept. 1996. DOI: 10.1364/josaa.13.001870.

[147] Philippe Lalanne and G. Michael Morris. "Highly improved convergence of the coupled-wave method for TM polarization". In: *Journal of the Optical Society of America A* 13.4 (Apr. 1996), p. 779. ISSN: 1084-7529. DOI: 10.1364/josaa.13.000779.

[148] I. S. Culshaw, D M Whittaker, and I. S. Culshaw. *Scattering-matrix treatment of patterned multilayer photonic structures*. 1999. DOI: 10.1103/PhysRevB.60.2610.

[149] *PPML - Periodically Patterned Multi Layer - File Exchange - MATLAB Central*. URL: https://es.mathworks.com/matlabcentral/fileexchange/55401-ppml-periodically-patterned-multi-layer.

[150] J.-M. Manceau et al. "Optical critical coupling into highly confining metal-insulator-metal resonators". In: *Applied Physics Letters* 103.9 (Aug. 2013), p. 091110. ISSN: 0003-6951. DOI: 10.1063/1.4819491.

[151] David Alcaraz Iranzo et al. "Probing the ultimate plasmon confinement limits with a van der Waals heterostructure". In: *Science* 360.6386 (Apr. 2018), pp. 291–295. ISSN: 10959203. DOI: 10.1126/science.aar8438. arXiv: 1804.01061.

[152] Sukosin Thongrattanasiri, Alejandro Manjavacas, and F. Javier García De Abajo. "Quantum finite-size effects in graphene plasmons". In: *ACS Nano* 6.2 (2012), pp. 1766–1775. ISSN: 19360851. DOI: 10.1021/nn204780e.

[153] N. M.R. Peres et al. "Exact solution for square-wave grating covered with graphene: Surface plasmon-polaritons in the terahertz range". In: *Journal of Physics Condensed Matter* 25.12 (Mar. 2013), p. 125303. ISSN: 09538984. DOI: 10.1088/0953-8984/25/12/125303. arXiv: 1211.6358.

[154] Juan Luis Garcia-Pomar, Alexey Yu Nikitin, and Luis Martin-Moreno. "Scattering of graphene plasmons by defects in the graphene sheet". In: *ACS Nano* 7.6 (2013), pp. 4988–4994. ISSN: 19360851. DOI: 10.1021/nn400342v. arXiv: arXiv:1301.5152v1.

[155] Bo Zhao and Zhuomin M. Zhang. "Strong Plasmonic Coupling between Graphene Ribbon Array and Metal Gratings". In: *ACS Photonics* (2015), p. 151021110440(ISSN: 2330-4022. DOI: 10.1021/acsphotonics.5b00410.

[156] Guoxi Wang et al. "Graphene plasmonic lens for manipulating energy flow". In: *Sci. Rep.* 4 (Feb. 2014), pp. 1–7. ISSN: 2045-2322. DOI: 10.1038/srep04073.

[157] I. Torre et al. "Lippmann-Schwinger theory for two-dimensional plasmon scattering". In: *to be published* ().

[158] I. Tan Lin, Chunru Fan, and Jia Ming Liu. "Propagating and Localized Graphene Surface Plasmon Polaritons on a Grating Structure". In: *IEEE Journal on Selected Topics in Quantum Electronics* 23.1 (2017), pp. 1–4. ISSN: 1077260X. DOI: 10.1109/JSTQE.2016.2596262.

[159] Yilei Li et al. "Graphene plasmon enhanced vibrational sensing of surface-adsorbed layers." In: *Nano letters* 14.3 (Mar. 2014), pp. 1573–1577. ISSN: 1530-6992. DOI: 10.1021/nl404824w.

[160] Daniel Rodrigo et al. "Mid-infrared plasmonic biosensing with graphene". In: *Science* 349.6244 (2015), pp. 165–168. ISSN: 1098-6596. DOI: 10.1017/CBO9781107415324.004. arXiv: arXiv:1011.1669v3.

[161] In-Ho Lee et al. "Graphene acoustic plasmon resonator for ultrasensitive infrared spectroscopy". In: *Nature Nanotechnology* 14.4 (Apr. 2019), pp. 313–319. ISSN: 1748-3387. DOI: 10.1038/s41565-019-0363-8.

[162] P A D Gonçalves and N M R Peres. *An Introduction to Graphene Plasmonics*. WORLD SCIENTIFIC, June 2016. ISBN: 978-981-4749-97-8. DOI: 10.1142/9948.

[163] G. X. Ni et al. "Fundamental limits to graphene plasmonics". In: *Nature* 557.7706 (May 2018), pp. 530–533. ISSN: 0028-0836. DOI: 10.1038/s41586-018-0136-9.

[164] Jeremy J Baumberg et al. "Extreme nanophotonics from ultrathin metallic gaps". In: *Nature Materials* (). DOI: 10.1038/s41563-019-0290-y.

[165] C. Ciraci et al. "Probing the Ultimate Limits of Plasmonic Enhancement". In: *Science* 337.6098 (2012), pp. 1072–1074. ISSN: 0036-8075. DOI: 10.1126/science.1224823.

[166] Ki Kang Kim et al. "Synthesis of monolayer hexagonal boron nitride on Cu foil using chemical vapor deposition". In: *Nano Letters* 12.1 (2012), pp. 161–166. ISSN: 15306984. DOI: 10.1021/nl203249a.

[167] Nanfang Yu and Federico Capasso. "Flat optics with designer metasurfaces". In: *Nature Mater.* 13.2 (Jan. 2014), pp. 139–150. ISSN: 1476-1122. DOI: 10.1038/nmat3839.

[168] A. Moreau et al. "Impact of nonlocal response on metallodielectric multilayers and optical patch antennas". In: *Physical Review B - Condensed Matter and Materials Physics* 87.4 (Jan. 2013). ISSN: 1098-0121. DOI: 10.1103/PhysRevB.87.045401.

[169] L.R. Baker. "Electromagnetic Surface Modes". In: *Optica Acta: International Journal of Optics* 30.3 (1983), pp. 257–257. ISSN: 0030-3909. DOI: 10.1080/716099614.

[170] Cristian Ciracì, John B. Pendry, and David R. Smith. "Hydrodynamic Model for Plasmonics: A Macroscopic Approach to a Microscopic Problem". In: *ChemPhysChem* 14.6 (Apr. 2013), pp. 1109–1116. ISSN: 14394235. DOI: 10.1002/cphc.201200992.

[171] Aleksandar D. Rakić et al. "Optical properties of metallic films for vertical-cavity optoelectronic devices". In: *Applied Optics* 37.22 (Aug. 1998), p. 5271. ISSN: 0003-6935.

[172] Dominique Barchiesi and Thomas Grosges. "Fitting the optical constants of gold, silver, chromium, titanium, and aluminum in the visible bandwidth". In: *Journal of Nanophotonics* 8.1 (Jan. 2014), p. 083097. ISSN: 1934-2608. DOI: 10.1117/1.JNP.8.083097.

[173] J. S. Lehtinen et al. "Evidence of quantum phase slip effect in titanium nanowires". In: *Physical Review B - Condensed Matter and Materials Physics* 85.9 (Mar. 2012). ISSN: 1098-0121. DOI: 10.1103/PhysRevB.85.094508.

[174] Yu Luo et al. "Surface plasmons and nonlocality: A simple model". In: *Physical Review Letters* 111.9 (2013), pp. 1–5. ISSN: 00319007. DOI: 10.1103/PhysRevLett.111.093901. arXiv: 1308.1708.

[175] Eduardo J.C. Dias et al. "Probing nonlocal effects in metals with graphene plasmons". In: *Physical Review B* 97.24 (2018), p. 245405. ISSN: 24699969. DOI: 10.1103/PhysRevB.97.245405. arXiv: 1804.06478.

[176] Frederico Dias Nunes et al. "Electromagnetic energy density in dispersive and dissipative media". In: *Journal of the Optical Society of America B* 28.6 (June 2011), p. 1544. ISSN: 0740-3224. DOI: 10.1364/JOSAB.28.001544.

[177] Arthur L. Schawlow and Chrales H. Townes. *MASERS and MASER Communication System*. 1958.

[178] A. L. Schawlow and C. H. Townes. "Infrared and optical masers". In: *Physical Review* 112.6 (1958), pp. 1940–1949. ISSN: 0031899X. DOI: 10.1103/PhysRev.112.1940.

[179] P. Franken et al. "Generation of Optical Harmonics". In: *Physical Review Letters* 7.4 (Aug. 1961), pp. 118–119. ISSN: 0031-9007. DOI: 10.1103/PhysRevLett.7.118.

[180] Robert W. Boyd. *Nonlinear optics*. Academic Press, 2008, p. 613. ISBN: 9780123694706.

[181] Annunziata Savoia et al. "Nonlocal optical second harmonic generation from centrosymmetric birefringent crystals: the case of muscovite mica". In: *Journal of the Optical Society of America B* 28.4 (2011), p. 679. ISSN: 0740-3224. DOI: 10.1364/JOSAB.28.000679.

[182] A. Rubano et al. "Electronic states at polar/nonpolar interfaces grown on SrTiO 3 studied by optical second harmonic generation". In: *Physical Review B - Condensed Matter and Materials Physics* 88.24 (2013), pp. 1–10. ISSN: 10980121. DOI: 10.1103/PhysRevB.88.245434.

[183] Dong Sun et al. "Ultrafast relaxation of excited dirac fermions in epitaxial graphene using optical differential transmission spectroscopy". In: *Physical Review Letters* 101.15 (Oct. 2008). ISSN: 00319007. DOI: 10.1103/PhysRevLett.101.157402.

[184] Jared H. Strait et al. "Very Slow Cooling Dynamics of Photoexcited Carriers in Graphene Observed by Optical-Pump Terahertz-Probe Spectroscopy". In: *Nano Letters* 11.11 (Nov. 2011), pp. 4902–4906. ISSN: 1530-6984. DOI: 10.1021/nl202800h.

[185] Nathaniel M Gabor et al. "Hot carrier-assisted intrinsic photoresponse in graphene." In: *Science* 334.6056 (Nov. 2011), pp. 648–52. ISSN: 1095-9203. DOI: 10.1126/science.1211384.

[186] Renwen Yu, Alejandro Manjavacas, and F. Javier García De Abajo. "Ultrafast radiative heat transfer". In: *Nature Communications* 8.1 (Dec. 2017). ISSN: 20411723. DOI: 10.1038/s41467-016-0013-x. arXiv: 1608.05767.

[187] K. J. Tielrooij et al. "Generation of photovoltage in graphene on a femtosecond timescale through efficient carrier heating". In: *Nature Nanotechnology* 10.5 (May 2015), pp. 437–443. ISSN: 17483395. DOI: 10.1038/nnano.2015.54. arXiv: 1504.06487.

[188] Matt W. Graham et al. "Photocurrent measurements of supercollision cooling in graphene". In: *Nature Physics* 9.2 (2013), pp. 103–108. ISSN: 17452481. DOI: 10.1038/nphys2493. arXiv: 1207.1249.

[189] Chandra M Natarajan, Michael G Tanner, and Robert H Hadfield. "Superconducting nanowire single-photon detectors: physics and applications". In: *Superconductor Science and Technology* 25.6 (June 2012), p. 063001. ISSN: 0953-2048. DOI: 10.1088/0953-2048/25/6/063001.

[190] Y. R. Shen. *The principles of nonlinear optics*. Wiley-Interscience, 2003, p. 563. ISBN: 9780471430803.

[191] Johannes Flick, Nicholas Rivera, and Prineha Narang. "Strong light-matter coupling in quantum chemistry and quantum photonics". In: *Nanophotonics* 7.9 (2018), pp. 1479–1501. DOI: 10.1515/nanoph-2018-0067.

[192] Milos Toth and Igor Aharonovich. "Single Photon Sources in Atomically Thin Materials". In: *Annual Review of Physical Chemistry* 70.1 (June 2019), pp. 123–142. ISSN: 0066-426X. DOI: 10.1146/annurev-physchem-042018-052628.